DISSERTATION

EARTH, HUMANS, AND METALS: INVESTIGATING THE ROLE OF IRON AND OTHER METALS IN THE ATMOSPHERIC, OCEANIC, AND ENERGY SYSTEMS

Submitted by

Sagar D. Rathod

Department of Atmospheric Science

In partial fulfillment of the requirements

For the Degree of Doctor of Philosophy

Colorado State University

Fort Collins, Colorado

Fall, 2022

Doctoral Committee:

Advisor: Jeffrey R. Pierce
Co-Advisor: Tami C. Bond

A. Scott Denning
Emily V. Fischer
Ryan P. Scott

ABSTRACT

EARTH, HUMANS, AND METALS: INVESTIGATING THE ROLE OF IRON AND OTHER METALS IN THE ATMOSPHERIC, OCEANIC, AND ENERGY SYSTEMS

Metals such as iron and copper have been an integral component of the Earth system since its beginnings and have formed the basis for modern human civilization growth since the Bronze and Iron Ages. Human activities include metals at various levels, from burning coal in power plants and mining ores lead to emissions of particulate and gaseous metallic products into the atmosphere. While suspended in the air, metal oxides such as hematite and magnetite absorb solar radiation, thus warming the atmosphere. After falling into the oceans, metals such as iron and magnesium act as important nutrients for oceanic biota, and thus affect the marine nutrient and carbon cycles. Human activities have increased many-fold since the beginning of the Industrial Era, and as the world moves from fossil fuel to renewable energy to reduce carbon emissions, the demand for metals is also projected to increase many folds. Yet, the past, present, and future impacts of anthropogenic activities on the atmospheric and marine metal cycles, particularly iron, remain poorly understood.

In Chapter 2, I estimate the atmospheric radiative and oceanic biological impacts of anthropogenic iron emissions over the Industrial Era. I perform simulations using a mineralogy-based inventory and an Earth System Model and estimate the 1850-to-2010 global mean direct radiative forcing by anthropogenic iron to be +0.02 to +0.10 W/m^2. I estimate that the enhanced phytoplankton primary production due to anthropogenic soluble iron deposition over the last 150 years caused carbon dioxide (CO_2) sequestration of 0.2-13 ppmv. This sequestered CO_2 also led

to an 'avoided' CO_2 forcing of -0.002 to -0.16 W/m^2. While globally small, these impacts can be higher in specific regions; the anthropogenic iron oxide direct radiative forcing is +0.5 W/m^2 over areas such as East Asia and India with more coal combustion and metal smelting. Anthropogenic soluble iron sustains >10% of marine net primary productivity in the high-latitude North Pacific Ocean, a region vulnerable to thermal stratification due to climate change.

In Chapter 3, I focus on evaluating anthropogenic total iron emissions using observations and models. Performing the model-observation comparison only at sites where the modeled anthropogenic contribution is the highest, I find that the current emission inventory underestimates anthropogenic total iron emissions from North America and Europe by a factor of 3-5. Further isolating anthropogenic sectoral emissions over North America using Positive Matrix Factorization, I find that smelting and coal combustion emissions are overestimated by a factor of 3-10 in the current emission inventory, whereas heavy fuel oil emissions from ships and industrial boilers are underestimated by a factor of 2-5. By comparing modeled concentrations of iron oxides with observations from Japan, I find that the current smelting and coal combustion emissions from East Asia are only slightly overestimated in the inventory, by a factor of 1.2-1.5.

Finally, in Chapter 4, I explore the regionality and magnitude of $PM_{2.5}$ emissions from metal mining and smelting to meet projected global renewable energy demand. I estimate future $PM_{2.5}$ (particulate matter smaller than 2.5 μm diameter) emissions from mining and smelting to meet the metal demand of renewable energy technologies in two climate pathways to be 0.3-0.6 Tg/yr in the 2020-2050 period, which is projected to contribute 10-30% of total anthropogenic primary $PM_{2.5}$ combustion emissions in many countries. The concentration of mineral reserves in a few regions means the impacts are also regionally concentrated. Rapid decarbonization could lead to a

faster reduction of overall anthropogenic $PM_{2.5}$ emissions but also could create more unevenness in the distributions of emissions relative to where demand occurs.

ACKNOWLEDGEMENTS

First and foremost, I would like to thank the funding agency USA Department of Energy for the grant DE-SC0016362, Collaborative Proposal "Fire, Dust, Air, and Water: Improving Aerosol Biogeochemistry Interactions in ACME." which provided most funding for this work. Tami Bond provided funding for my last year of Ph.D. from her seed fund at the Colorado State University. A big thank you to my advisers, Tami Bond and Jeffrey Pierce, for providing guidance and feedback throughout this project. Tami, who took the risk of hiring and funding me on a topic we both had almost no idea about; and Jeff, who provided me with a supportive group and an academic place along with tons of insightful discussions: you both are awesome! I am also grateful to my Ph.D. committee members, Emily Fischer, Ryan Scott, and A. Scott Denning, for their scientific advice and insightful discussions. I also thank all my collaborators, Natalie Mahowald, Douglas Hamilton, Longlei Li, Emily Bian, Sonia Kreidenweis, Lance Nino, Zbigniew Klimont, Peter Rafaj, and many others, for their help and discussions on this project.

Next, I would like to thank all the mentors from my undergraduate program through the Ph.D. Late Dr. Nanak Varandani, who accepted me as a project assistant at the Gujarat Energy Research and Management Institute; Professors Dimpi Shah and Huma Syed, for helping me with a difficult final-year undergraduate project; and Virendra Sethi, who hired me as a research associate at the Indian Institute of Technology, Bombay, for a project whose funding was even uncertain: you all are deeply thanked. My interactions with Virendra Sethi were the ones that motivated me to do science via inquiry.

A big thanks to the academic staff at the Colorado State University in the Atmospheric Science Department, the Graduate School, and the Office of International Program. Sarah Tisdale and

many others, who made sure my transition from the University of Illinois was smooth, that I met all the university requirements on time, and that I always met the US immigration requirements: your help is why I was able to focus on research and not worry about the admin things.

A good support system is important for surviving and staying sane in grad school. I would like to thank all my friends and colleagues in atmospheric science and mechanical engineering. John, Kate, William, Michael, Sam, Anna, Ali, Nicole, En, Betty, Sarah, Julieta, Dhyey, and many others, for their wonderful help and support throughout! Particularly, I would like to thank the Atmospheric Science Diversity, Equity, and Inclusion Committee, for doing great work and providing wonderful support resources to the grad students and faculty. A big thanks to the Atmospheric Science International Students and Scholars Association, for all the fun events and hangouts over the last two years!

Slightly unconventional, but great thanks to all the indirect good things that happened to me in life. All the great movie-makers and songwriters, all the great bus drivers and food-delivery folks, and all the great people who made sure the world ran OK even during a pandemic: you all made my life and the journey smooth, and you all are deeply thanked.

And finally, I would like to sincerely thank my family and loved ones. My parents, Dina and Dilip, provided unconditional love and support. Nothing I would say here would be enough to thank them. A very big thanks to my brother Ankit and his wife Krupali, for looking after our parents and taking care of them, particularly during all the ups and downs. Ankit and Krupali ensured I had the mental freedom to go out and chase my dreams and not worry about our parents. I am deeply indebted to their support. Friends from the undergraduate school in Ahmedabad, and graduate schools in Urbana-Champaign and Fort Collins were always super supportive. Keyur, Harshils, Jay, Bhavik, and many others from L.D. College of Engineering; Varenya, Akash,

Joseph, and many others from Urbana-Champaign, and Wayne, Dhyey, and many others from Fort Collins: I could not have survived grad school without your camaraderie. And finally, I would like to thank Chaitri, my partner and my support, who also went through the Ph.D. struggle, and bore with me through the ups and down. This would not have been a fun journey without you.

DEDICATION

This work is dedicated to all those who chose academic and research jobs.

“Saala ye dukh kahe khatam nahi hota hai bey?”

Deepak Kumar, Masaan 2015

TABLE OF CONTENTS

CHAPTER 1

BACKGROUND AND MOTIVATION

1.1 Background

1.1.1 Humans, the Earth, and metals

Metals are an important part of the human system. Metals are some of the most abundant crustal and interstellar material (Skinner, 1979) and have been an integral part of human civilization's growth since the bronze and iron ages (Yahalom-Mack et al., 2014). Metals also are an integral part of the modern-day infrastructure all humans live and interact in and with: from semiconductors in phones to wires that carry electricity and from the steel bars used in building construction to the aluminum in car bodies. Along with being used in physical structures, metals such as iron and manganese also are crucial in various biological and chemical processes such as carrying blood oxygen via hemoglobin (Sundararajan & Rabe, 2021).

Metals are also important in the Earth system. Metals such as iron, cobalt, manganese, and molybdenum are essential nutrients for terrestrial and oceanic biota: plant and phytoplankton cells require these metals to perform essential functions such as carbon and nitrogen fixation (C. M. Moore et al., 2013; Twining & Baines, 2013; Wong et al., 2021). Current estimates suggest that metal co-limitation exists in over 50% of ocean areas (C. M. Moore et al., 2013; J. K. Moore et al., 2001), and sufficient nutrient supply can almost double the marine productivity (J. K. Moore et al., 2001). Metals such as iron, while in the air interact with the solar radiation and are shown to warm the atmosphere (Moteki et al., 2017; Scanza et al., 2015). It is the hematite (an iron oxide) in dust that makes it warm the atmosphere (Lafon et al., 2006). After inhalation in particulate form, metals such as iron, copper, and manganese have been shown to enhance the toxicity of air

pollutants (Yixiang Wang et al., 2020). Thus, metals also have complex interactions in the Earth and human systems.

The case for iron

While many metals are crucial in the proper functioning of the Earth and the human systems, iron particularly has an important role due to its magnitude and its impacts in various areas.

1. Human activities use iron more than any other metals: The present-day iron and steel industry output of 1900 million tons/yr dwarfs all other metal industries combined by an order of magnitude (World Mineral Statistics, 2020). This huge demand occurs because of its versatile properties and an important role in various sectors such as construction, machinery, co-production of other metals and alloys, consumer and industrial productions, and transportation.

2. Iron is an essential nutrient for phytoplankton activity: Iron is an essential component of the nitrogenase enzyme that enables phytoplankton to convert or 'fix' oceanic nitrate into ammonia and similar forms, which are then used for cell growth. Iron as a nutrient is lacking compared to other nutrients such as nitrogen and phosphorus in over 40% of ocean waters, limits phytoplankton growth, and thus influences the oceanic carbon cycle (J. H. Martin et al., 1990). It is hypothesized that a sufficient supply of iron to these iron-limited oceans can almost double the current oceanic net primary productivity (J. K. Moore et al., 2001).

3. Iron-minerals absorb solar radiation: Particulate iron emissions are suggested to exert warming of more than +0.5 W/m^2 over many industrialized areas, similar to other widely-studied climate forcers such as black and brown carbon (Matsui, Mahowald, et al., 2018; Moteki et al., 2017).

This dissertation studies the earth and energy system effects of metals, particularly iron: The first two chapters of this dissertation focus on the emissions and Earth system interactions of anthropogenic iron -- the iron that is emitted into the atmosphere from human activities. Among the Earth system interactions, this dissertation focuses on the oceanic phytoplankton enhancements and the atmospheric radiative warming, since they represent the major pathways of human influence on climate and are also poorly understood. The last chapter of this dissertation looks at potential air pollution due to metal mining and smelting to meet renewable energy demand in future scenarios. In the rest of this Introduction chapter, I will describe how iron enters the atmosphere from human activities such as combustion, what happens while it in the atmosphere, how it falls into the ocean, and what happens after its deposition. And finally, I will describe the role of metals in renewable energy devices.

1.1.2 Anthropogenic iron in the Earth system

1.1.2.1 Iron in the atmosphere

How does iron from human activities enter the atmosphere?

Emissions: Humans burn fossil fuels such as coal and oil to obtain power for homes, industries, and vehicles. Fuels contain iron in various forms due to geological processes (Dai et al., 2005). During combustion, the iron in the fuel vaporizes, condenses, undergoes physico-chemical transformations, and finally gets released from the combustion chamber in form of small particles of diameters between 0.01 to 100 μm (Flagan & Seinfeld, 2012). Of these sizes, the ones smaller than 10 μm are of greatest interest as they could travel farther and stay in the atmosphere longer than the larger particles. The smaller particles also could be more toxic to human health via the inhalation pathway (Ge et al., 2018). For a single source, emissions are estimated using three

major components: activity data, emission factors, and abatement applied after the combustion chamber and before the atmospheric release (Bond et al., 2004). For example, emission from a coal power plant is estimated by multiplying its activity (amount of coal burned or energy generated) and emission factor (mass of air pollutant emitted per unit coal burned or energy generated). This is still the raw or 'uncontrolled' emission which then undergoes some cleaning up (abatement) before it is released into the atmosphere. To then estimate the amount of iron emitted globally from all anthropogenic sources, information on the different types of fuels burned in a year is first gathered, generally from regional or international energy agencies such as the International Energy Agency. Fuel combustion in different technologies (e.g. pulverized, stoker grate, or fluidized bed coal combustors) leads to different amounts and sizes of emissions (Bond et al., 2004). Based on information from finer regional or national energy agencies, assumptions are made to estimate in which combustion technology a fuel was burned in a country in a given year (e.g. of the 100 coal power plants in a country, 50% are pulverized combustors, 30% are fluidized bed combustors, and 20% are stoker grate combustors). These technology-based activities are then multiplied by technology-specific emission factors (e.g. pulverized combustor emits less $PM_{2.5}$ (particulate matter smaller than 2.5 μm diameter) per kg coal burned than a stoker grate). And finally, assumptions are made on the regional/national distribution of abatement application per fuel and combustion technology (e.g. 50% of all coal power plants in a country have Electrostatic Precipitator, and other 50% have bag filter). A similar methodology applies to sectors such as mining and other fugitive emissions where combustion is not involved. In those cases, area-approximated values are used form observations and multiplied by the driving activity to estimate emissions (Z. Klimont et al., 2002).

The term ‘anthropogenic’ in this dissertation Is defined as the sum of all combustion- and process-related emissions from power, industrial, residential, and transportation sectors, including mining. Excluded from this definition are emissions from wildfires and dust, even if they have changed over the years due to anthropogenic activities.

Mineralogy is a key factor in emissions: The mineralogy of iron governs its atmospheric and oceanic interactions (A. Ito, 2015; Journet et al., 2008). For Earth-system-relevant interactions, I aggregated the mineral forms of iron into three major categories: Clays, Oxides, and Sulfates. Clays are kaolinite and illite, which have a large soluble fraction of iron and mainly scatter solar radiation. Oxides are hematite and magnetite, which have a small soluble fraction of iron and mainly absorb solar radiation. Sulfates are iron sulfates, which have the highest soluble fraction of iron and are assumed to absorb solar radiation. In terms of emission sources, coal contains iron as sulfides and clays and its combustion emits iron as oxides and clays. Liquid fuels such as heavy fuel oil and diesel contain iron as organo-metallic porphyrins, but oil extraction and refining process-accumulated sulfates dominate, and its combustion emits iron mainly as sulfates and oxides. Wood contains iron as sulfides and as inclusions in clays. Iron and steel smelting emits iron as oxides due to high-temperature oxidation.

Various estimates of anthropogenic combustion-iron emissions. The current global total iron emission from anthropogenic activities ranges from 0.5 to 3 Tg/yr (A. Ito, 2015; Matsui, Mahowald, et al., 2018, p. 20; Rathod et al., 2020; R. Wang, Balkanski, Boucher, et al., 2015). Differences in emissions among the studies are due in part to the inclusion of some major new sources of iron emissions such as smelting, as well as the emission estimation methodology itself (Rathod et al., 2020). In the Rathod et al., (2020) inventory, among the anthropogenic combustion sources, liquid fuels, wood, coal, and smelting contribute 1.6, 5.0, 18, and 75% of global fine

(PM_1) particle emissions, respectively, and about 1.5, 1.2, 49, and 48% of global coarse (PM_{1-10}) iron emissions, respectively. Compared to anthropogenic with values of 0.5-3 Tg Fe/yr, iron emissions from dust are in the range of 40-140 Tg Fe/yr and from wildfires about 1-3 Tg Fe/yr for the year 2010 (A. Ito, 2015; Matsui, Mahowald, et al., 2018; Myriokefalitakis et al., 2018; Rathod et al., 2020; R. Wang, Balkanski, Boucher, et al., 2015). However, the regionality of emissions, and thus impacts, is different for these sources: most anthropogenic emissions occur in industrial areas, generally near human populations, and contribute iron to the North Pacific and the North Atlantic Oceans whereas most dust emissions come from the Saharan, Chilean, and other deserts, generally far from human populations and contribute iron to the Atlantic, the Equatorial Pacific, and the Southern Oceans.

Atmospheric modeling: Because observations are sparse and do not extend far into the past, climate models are used to simulate global radiative forcing and ocean response to emissions, reconstruct past climates, and predict future impacts. These models use emission inventories as inputs, simulate the aerosol and gaseous transport, and are evaluated using present-day observations. Atmospheric transport models estimate the concentration and deposition of iron by simulating aerosol processes such as coagulation and deposition and solving fluid transport equations at each point of the domain area. In the process, external factors such as meteorology and land use that affect aerosol transport are specified in the model. To accurately represent past, present, and future Earths in the models, it is also crucial to benchmark or constrain the models. For example, in the climate context, models are constrained using historical temperature data. For aerosol and gaseous contexts, most modeling groups constrain the output using either the concentration (Hamilton et al., 2019) or an effect, such as Aerosol Optical Depth (AOD) (Huang et al., 2018). For the concentration-based benchmarking, modeled values are compared directly

against observed concentrations from single or multiple sites. Most iron cycling models are currently constrained using observations from remote iron-limited oceans (Stelios Myriokefalitakis et al., 2018). These iron concentration observations were taken using ship-based aerosol samplers in the last 20+ years and cover most iron-limited areas (Hamilton et al., 2019).

What happens after iron is suspended in the atmosphere?

Iron aerosol absorbs and scatters radiation: The suspended iron particles, depending on the size and mineralogy, absorb or scatter the incoming solar radiation. Iron-containing minerals such as hematite and magnetite (collectively "Iron Oxides") are dark and absorb solar radiation, similar to black carbon (Lafon et al., 2006). This absorption leads to atmospheric warming. In contrast, iron-containing minerals such as kaolinite and illite (collectively "Clays") generally scatter radiation and thus cool the atmosphere (M. Querry, 1987; Scanza et al., 2015). This cooling or warming is generally expressed on a common metric, W/m^2, which indicates the fraction of the incoming solar radiation that is absorbed into the atmosphere or scattered back to the space by a species. This effect is also known as the 'direct radiative effect'. The difference in this radiative effect over a period is known as 'direct radiative forcing' which indicates the change in the Earth's energy balance. Iron oxides in the form of aggregated magnetite particles from anthropogenic sources have a 10-40% of mass absorption cross-section (the ability to absorb solar radiation) as black carbon and contribute about 7% of the regional shortwave absorption of black carbon, based on aircraft measurements over the Yellow Sea and the East China Sea (Moteki et al., 2017). Modeling studies suggest present-day iron oxide global direct radiative effect to be +0.02 W/m^2 and +0.5 W/m^2 over industrial areas of East Asia (A. Ito et al., 2018; Matsui, Mahowald, et al., 2018).

1.1.2.2 Iron in the ocean

How does iron get into the ocean?

Transport modeling: For oceans, another quantity, the 'soluble iron' is of particular importance as it is this part of the total iron that stimulates phytoplankton growth. At emission, a component of the particulate total iron dissolves in water ("Soluble fraction"), and another component that does not ("Insoluble fraction") (Baker & Croot, 2010). The soluble fraction is readily taken up by phytoplankton in oceans to perform cell processes (Shaked & Lis, 2012). During its time in the atmosphere, the insoluble fraction interacts with acids and ligands and a part of it becomes soluble (A. Ito, 2015). The total soluble iron flux to the ocean is thus the initial soluble iron emitted and the additional soluble iron created via dissolution processes in the atmosphere. This interaction of the insoluble fraction of the emitted iron with acids and ligands depends on the iron mineralogy (A. Ito, 2015; Meskhidze et al., 2019). Among the minerals carried, iron oxides have a low initial solubility (<0.01%) and also react very slowly in the atmosphere whereas iron sulfates (38-80%) and clays have higher initial solubility (1-4%) and also react at a comparatively faster rate (Journet et al., 2008; Meskhidze et al., 2019; Rathod et al., 2020). While a mineralogy-based representation is well-studied for dust, only one study (Rathod et al., 2020) has modeled anthropogenic emissions via a mineralogy basis for atmospheric soluble iron concentration and deposition.

Iron falls into the oceans via dry and wet deposition: The iron emitted from dust, fires, and human activities travel large distances in the atmosphere due to its small size and eventually falls on various parts of the world. The oceans cover about 70% of the Earth's surface area and hence receive a large fraction of these suspended particles. There are two major pathways of iron

deposition from the atmosphere into the ocean: dry and wet. Dry deposition occurs when particles fall out of the atmosphere due to atmospheric turbulence and as they become heavier due to coagulation and condensation. Wet deposition occurs when particles get scavenged by falling precipitation such as rain and snow. More than 60% of global soluble iron deposition to oceans occurs via wet deposition and the rest by dry deposition (Myriokefalitakis et al., 2018; Rathod et al., 2020)

Anthropogenic contribution is high over North Pacific and North Atlantic iron-limited basins: Although anthropogenic sources contribute only about 5% of the total atmospheric soluble iron deposition (Hamilton et. al., 2019; Rathod et al., 2020), they contribute about 25% of the total soluble iron deposition to the North Pacific and North Atlantic Oceans (Table 1.1). This high anthropogenic contribution to the North Pacific Ocean is also suggested by observational studies that used isotopic markers (Kurisu et al., 2021; Pinedo-González et al., 2020). Anthropogenic contribution to the Southern Ocean is relatively smaller (<5% of total atmospheric soluble iron), although some observationally-based studies suggest it could be higher, by a factor of 2-5 (A. Ito et al., 2019; M. Liu et al., 2022). Similar to total iron, the soluble iron flux is validated using observations. However, only a small fraction of the observations reporting total iron concentration also measure soluble fraction, thus soluble iron is less constrained than total iron (Hamilton et al., 2019).

Table 1.1: Atmospheric soluble iron deposition and percent from anthropogenic sources in a few iron-limited basins. Hamilton et al., (2019) and Rathod et al., (2020).

Basin	**Atmospheric soluble iron deposition (Gg/yr)**	**Percent from anthropogenic sources (%)**
Global ocean	530	5

North Pacific	40	25
North Atlantic	90	25
Southern Ocean	40	2

What happens after iron falls into the oceans?

Phytoplankton grow by taking up iron: Following deposition, the bioavailable iron (soluble iron) is directly ready for uptake by phytoplankton, whereas the particulate insoluble part slowly solubilizes (converts to soluble iron) in presence of ligands while it is gravitationally sinking (Baker & Croot, 2010; Shaked & Lis, 2012). During the growth phase, phytoplankton consume the dissolved carbon in the ocean, thus creating a diffusion gradient from the atmosphere to the ocean and drawing down carbon dioxide. In locations where phytoplankton growth is nitrogen-limited, iron aids in the cyanobacteria secretion of nitrogenase, an enzyme responsible for nitrogen fixation, thus, indirectly enhancing carbon uptake by reducing nitrogen limitation (Schoffman et al., 2016). This 'new' growth of phytoplankton mass due to nutrient addition contributes to the marine Net Primary Productivity. Currently, atmospheric soluble iron supply from dust, wildfires, and anthropogenic sources to these iron-limited areas is suggested to account for about 15-20% of ocean net primary productivity (Okin et al., 2011). However, the role of anthropogenic contribution has not yet been separately evaluated.

Dying phytoplankton sequester carbon dioxide (CO_2): The newly-formed phytoplankton are then grazed by zooplankton and the subsequent ocean food chain. The sinking phytoplankton detritus and aggregates, fish fecal pellets, and zooplankton migration to the deep ocean lead to carbon (and other nutrients including Fe) supply from surface to end of the euphotic zone (100-150m) (Basu & Mackey, 2018). These organic materials are bacterially decomposed during this

sinking and over 90% of the carbon and other nutrients make it back to the surface layer where they are again consumed by phytoplankton or get diffused out to the atmosphere. The remaining particulate carbon sinks into the deep ocean where it is sequestered for century timescales. Some of the sinking material also scavenges dissolved colloidal iron, thus removing it from the surface pool. The iron that is remineralized during the sinking stays in the deep waters for decadal-to-century timescales before appearing in surface waters in the upwelling regions (Philip W. Boyd et al., 2017; Siegel et al., 2014; Tagliabue et al., 2017).

1.1.3 Metals in the energy system

Renewable energy devices require many metals: More than 30 metals of conventional and rare-earth nature, are required in making solar photovoltaics, wind turbines, and electric vehicles (Giurco et al., 2019a). The main metals required in all these three technologies are iron, aluminum, copper, and lithium (Giurco et al., 2019; Watari et al., 2019). Solar and wind plants require about 1.2 and 0.2 million tons of metals per GigaWatt capacity, respectively, compared to 0.053 million tons by fossil fuel plants (Watari et al., 2019). Electric vehicles, require a similar amount of conventional metals such as iron and aluminum as internal combustion, but require about 6 and 13 kg of lithium and cobalt, respectively, per vehicle (Råde & Andersson, 2001; Watari et al., 2019).

Mining and smelting cause emissions during metal extraction and production: Mining and smelting are the two major methods to obtain all the metals for renewable energy devices. Emissions from mining include those from machinery movement (during excavation) and wind-blown dust in case of open-pit mines, as well as during storage of mined earth (Z. Klimont et al., 2002; US EPA, 1995). Emissions from smelting include those from high-temperature melting of ores in blast furnaces and electric arcs. Although mining processes occur far from residential areas, smelting activities are mostly located in the vicinity of urban areas (US Department of the Interior,

2019). Metal mining and smelting processes have been shown to contribute a high (10-40%) amount of atmospheric ambient $PM_{2.5}$ and particulate heavy metal concentration in various cities (Banza Lubaba Nkulu et al., 2018; Hedberg et al., 2005; Jorquera & Barraza, 2012a; Kavouras et al., 2001a; Y. H. Kim et al., 2016; Tan et al., 2017; Vijayanand et al., 2008; Yanan Wang et al., 2016; Xue et al., 2010). Although they are important contributors to ambient air pollution, they are generally unabated, especially in low- and middle-income countries (Crippa et al., 2018; Klimont et al., 2017; Rathod et al., 2020). Currently, the global emission estimate of particulate matter smaller than 2.5 μm diameter ("$PM_{2.5}$") from smelting activities is 3 (0.3-6) Tg/yr (Rathod et al., 2020), and metal mining and smelting are the largest sources of global trace metal emissions, especially rare-earth metals such as lithium, vanadium, and lead (Nriagu, 1979; Nriagu & Pacyna, 1988; Josef M. Pacyna et al., 1984; Jozef M. Pacyna & Pacyna, 2001; Rauch & Pacyna, 2009). Along with atmospheric emissions, mining and smelting also cause other environmental impacts such as heavy metal pollution in food and water cycles (Banza Lubaba Nkulu et al., 2018).

1.2 Motivation

As discussed above, the Earth and energy system interactions of metals are complex and involve various contributing factors such as human activities and emissions. Among these factors, I focused on how human activities affect the Earth and energy systems. I identified that even if the newer modeling and observational estimates suggest an important contribution to total and soluble iron by anthropogenic sources, its atmospheric radiative and oceanic biological productivity estimates are poorly understood. Moreover, I identified that metals play an important role in the energy transition from fossil fuels to renewables but the potential impacts due to their extraction

and processing are not yet estimated. These motivations form the basis of the three chapters in this dissertation and are described below.

1. Anthropogenic emission is an important contributor of soluble iron to the North Pacific Ocean and total iron over industrialized areas, yet its role in controlling marine productivity and atmospheric warming is poorly understood.

Direct radiative forcing (DRF). Modeling studies suggest present-day iron oxide global direct radiative effect to be +0.02 W/m^2 and +0.5 W/m^2 over the industrial areas of East Asia and East Europe (A. Ito et al., 2018; Matsui, Mahowald, et al., 2018). Iron's radiative interactions strongly depend on its mineralogy, but previous studies quantifying anthropogenic iron DRF did not include mineralogical speciation, and instead assumed all emitted iron emitted from the anthropogenic activity was in the form of iron oxides. Moreover, many prior studies have omitted various important iron emission sources, such as metal smelting, which contribute to over 70% of anthropogenic fine iron emissions.

Marine net primary productivity (NPP). Basins such as the North Pacific Ocean are iron-limited for phytoplankton growth and depend mainly on atmospheric sources for iron (C. M. Moore et al., 2013; J. K. Moore et al., 2001). Some of these basins are also vulnerable to thermal stratification due to climate change (Capotondi et al., 2012), which will further increase their dependency on atmospheric sources for essential nutrients. Like DRF, previous studies estimating soluble deposition by anthropogenic iron lacked a comprehensive mineralogical representation of iron aerosol. Anthropogenic sources contribute 20-50% of total atmospheric soluble iron deposition over the iron-limited North Pacific Ocean (Rathod et al., 2020) but their contribution to marine net productivity is not yet estimated separately from all (dust, fires, and anthropogenic

emission) atmospheric sources. *I address these questions by performing sensitivity simulations using a mineralogy-based emission inventory and an Earth system model.*

2. Models are not able to explain observed concentrations in various remote oceans; anthropogenic sources are pointed to as a possible reason.

Iron-cycling models currently under- and overestimate total and soluble iron concentrations over the Southern and Atlantic Oceans, respectively, by over two orders of magnitude (A. Ito et al., 2018; Rathod et al., 2020). Although the Southern Ocean model underestimation was attributed to underestimated wildfire and anthropogenic emissions, it did not improve even when the highest estimates of those emissions were used (Rathod et al., 2020). However, modeled concentration and deposition values are affected by various aspects and a "correct" modeled concentration can also be obtained through compensating errors, for example, high emissions are offset by rapid deposition. This raises a question: Is the model-observation mismatch in many ocean basins due to an underestimation in the emission inventory or is it the model's fault (transport parameterizations)? Surface aerosol concentrations in most iron cycling models are currently constrained using observations from remote iron-limited oceans (Stelios Myriokefalitakis et al., 2018) where transport and deposition dominate (e.g. Tsigaridis et al., 2014). Moreover, modeled iron concentration in remote oceans—the location of the most important biogeochemical effects—is compared with observations by moving ships taken over only a few days (Baker & Croot, 2010; Stelios Myriokefalitakis et al., 2018). These periods might be inadequate to capture the model variability that spans many orders of magnitude (Smith et al., 2017). This is in contrast with some modeled species like black carbon (Lee et al., 2013) or dust (Mahowald et al., 2002) which are evaluated against long-term data on land. *I address these questions by evaluating the model using*

global long-term near-source observations and isolating anthropogenic contributions in those observations using source apportionment methods.

3. Future metal demand in the energy system could increase many folds and can lead to more emissions from mining and smelting. Projections of future global warming due to ongoing human activities suggest a temperature increase of 2-6 ℃ compared to pre-industrial levels (Masson-Delmotte et al., 2021). To limit this temperature increase, many countries have committed to reducing their greenhouse gas emissions by shifting their energy sources to renewable energy such as solar and wind ("The Paris Agreement", UNFCCC, 2016). As economies move from fossil to renewable sources of energy to mitigate climate change, it will increase the demand for solar panels, wind turbines, and EVs, which in turn will increase the metal demand. The metal demand to make the major renewable energy technologies might reach around 5-20 times the present-day production levels in 2050 (e.g. Giurco et al., 2019), which will be met by mining and smelting which are emission-intensive processes. There has been no estimation of future impacts on air quality from the processes to supply these materials in high renewable energy demand climate mitigation scenarios. *I address these questions using observed and modeled data of metal demand in renewable energy devices, an emission inventory model that has a representation of current and future activities and abatement.*

1.3 Scope of the dissertation

This dissertation consists of three studies involving emission inventory evaluation, estimating the Earth system impacts of anthropogenic iron emissions, and estimating the future metal demand due to renewable energy deployment and the subsequent production-related emissions from

mining and smelting processes. The first two chapters essentially represent the application and evaluation of a comprehensive mineralogy-based inventory I developed for my Master's research (Rathod et al., 2020). The following paragraphs provide an overview of the chapters in this dissertation.

Chapter 2 is a research article accepted in*Geophysical Research Letters.* In this chapter, I estimate the 1850-to-2010 direct radiative forcing and net primary productivity impacts of anthropogenic emissions from combustion activities using a mineralogy-based emission inventory and an Earth system model. While many factors in emissions and modeling, such as particle size distribution and deposition flux rates, affect the DRF and NPP estimates, I mainly focus on mineralogy and emission magnitude, as they have been shown to have the greatest effect on the global total and soluble iron supply (Scanza, et al., 2020; Ito, 2015; Matsui et al., 2018).

Chapter 3 is a research article in preparation for the *Journal of Geophysical Research: Atmospheres*. In this chapter, I discuss the challenges and methods to evaluate an emission inventory using observations and models. I use long-term near-source observations to evaluate anthropogenic iron emissions from various regions. In the process, I also evaluate individual anthropogenic emission sources from the USA and East Asia using various speciated observations and statistical source apportionment tools.

Chapter 4 is a research article published in *Environmental Research Letters* (Rathod et al., 2022). In this chapter, I estimate the primary $PM_{2.5}$ emissions from mining and smelting of metals obtained specifically for making three technologies required to expand renewable energy: solar PV, wind turbines, and EVs. I also analyze the effect of metal production regionality on unequal distributions of emissions relative to demand and compare the effects of decarbonization rate and emission abatement on both emission totals and distributions.

Finally, Chapter 5 provides a summary of the above chapters along with future research directions that could fill some of the remaining knowledge gaps.

CHAPTER 2

ATMOSPHERIC RADIATIVE AND OCEANIC BIOLOGICAL PRODUCTIVITY RESPONSES TO INCREASING ANTHROPOGENIC-COMBUSTION IRON EMISSION IN THE 1850-2010 PERIOD[1]

2.1 Introduction

Iron-containing aerosols are toxic to human health (Wang et al., 2020), affect the atmospheric chemistry of acids (Harris et al., 2012; Kotronarou & Sigg, 1993), absorb and scatter solar radiation (Lafon et al., 2006), and enhance biological growth in nutrient-limited waters after deposition (J. H. Martin et al., 1990). Of these, its atmospheric radiative and oceanic biological interactions affect the Earth's energy budget and nutrient cycles. Iron emissions have various sources including dust, wildfires, and anthropogenic combustion (Mahowald et al., 2018). The anthropogenic fraction increases with population and economic growth but is not usually examined separately. Even though anthropogenic combustion iron has similar emission magnitude and radiation-absorbing properties as black carbon in Asia, and contributes to more than 25% of the total atmospheric soluble iron deposition in the nutrient-limited North Pacific and North Atlantic Oceans (Ito et al., 2019; Moteki et al., 2017; Rathod et al., 2020; Yoshida et al., 2018), its role in modulating the atmospheric radiative budget and the oceanic nutrient cycle is yet poorly understood. Some iron interactions are cumulative in nature, so quantifying their relationship with anthropogenic activities will lead to a better understanding of the human influence on the Earth system. This study aims at understanding these complex iron interactions using emission inventories and an Earth system model.

[1]This work is published in Geophysical Research Letters as Rathod et al., (2022). Atmospheric radiative and oceanic biological productivity responses to increasing anthropogenic-combustion iron emission in the 1850-2010 period.

Direct radiative forcing (DRF) is the first climate effect in the lifecycle of anthropogenic iron that occurs when suspended aerosols scatter or absorb radiation, thus changing the Earth's atmospheric energy budget. Present-day emissions of anthropogenic iron are estimated to exert a direct radiative effect of 0.02-0.05 W/m^2 globally and 0.2-1 W/m^2 over many industrialized regions, comparable to the forcing by carbonaceous species (Ito et al., 2018; Matsui et al., 2018). Iron's radiative interactions strongly depend on its mineralogy: iron oxide, like black carbon, is an efficient absorber (Single Scattering Albedo of ~0.6 for 1μm particle at 550 nm) of incoming shortwave solar radiation in contrast to the iron bound in clays that mainly scatters (Li et al., 2021; Moteki et al., 2017; Scanza et al., 2015). But the previous studies quantifying anthropogenic iron DRF did not include mineralogical speciation, and instead assumed all iron emitted from the anthropogenic activity was in the form of iron oxides (Ito et al., 2018; Matsui, Mahowald, et al., 2018). Moreover, many past studies have omitted major iron emission sources, such as metal smelting, which is responsible for over 70% of anthropogenic iron emissions (Ito, 2015; Luo et al., 2008; Rathod et al., 2020).

Marine net primary productivity (NPP) change is the second climate effect in the lifecycle of anthropogenic iron that occurs when the deposited soluble iron is taken up by phytoplankton for growth and to perform biological tasks such as nitrogen fixation (J. H. Martin et al., 1990; Tagliabue et al., 2017). Phytoplankton biomass accumulation and subsequent cycling lead to atmospheric CO_2 drawdown and sequestration into deep oceans, and this biological CO_2 pump is suggested to offset about 25% of annual anthropogenic CO_2 emissions (Le Quéré et al., 2018; Siegel et al., 2014). Soluble iron deposition is one of the strongest controls on marine NPP (Moore et al., 2001) which in turn depends on the mineralogical composition of iron (Journet et al., 2008; Meskhidze et al., 2019). Like DRF, previous studies estimating soluble deposition by

anthropogenic iron lacked a comprehensive mineralogical representation of iron aerosol. Anthropogenic sources contribute 20-50% of total atmospheric soluble iron deposition over the iron-limited North Pacific Ocean (Rathod et al., 2020), a region where iron is crucial for phytoplankton growth (S. Myriokefalitakis et al., 2020).

In this study, we estimate the mineralogically-speciated radiative and ocean biogeochemical effects of anthropogenic combustion-iron emission, in contrast with all previous studies that estimated the combined effect of dust, fire, and anthropogenic iron. We estimate the DRF and NPP effects over the 1850-to-2000 period using a mineralogy-based anthropogenic-combustion iron emission inventory and an Earth system model. Increased NPP leads to CO_2 sequestration which indirectly leads to an 'avoided' CO_2 forcing. We estimate this avoided forcing to compare the NPP effects against DRF using a common metric: W/m^2. While many factors in emissions and modeling, such as particle size distribution and deposition flux rates, affect the DRF and NPP estimates, we focus on mineralogy and emission magnitude as they have been shown to have the greatest effect on the global total and soluble iron supply (Scanza, et al., 2020; Ito, 2015; Matsui et al., 2018).

2.2 Methodology

We define anthropogenic emission as the sum of all combustion-related emissions from the power, industrial, residential, and transportation sectors. Excluded from this definition are emissions from wildfires and dust, even if they have changed over the years due to anthropogenic activities. This study aims to understand whether anthropogenic effects become important at central or upper bounds. Hence, we also perform various sensitivity analyses on anthropogenic iron emissions to understand the uncertainties in its DRF and NPP impacts; summarized in Tables A.1 and A.2 and explained below.

2.2.1 Direct Radiative Forcing

We estimate the anthropogenic iron DRF by carrying emissions in an atmospheric transport model and using a radiative transfer model. This method has three major elements: estimates of mineral emissions, atmospheric modeling to get concentration fields, and estimating DRF using concentration fields and mineral-specific optical properties.

Emissions: Iron is embedded in different minerals during combustion (e.g. Schroth et al., 2009) and these minerals also have other species such as oxygen, aluminum, and silica. We estimate the iron mineral emissions (sum of iron plus other species in a mineral) by dividing the iron-as-mineral emissions by the iron fraction in that mineral. Rathod et al., (2020) segregated anthropogenic combustion-iron minerals from coal, wood, oil, and smelting emissions into iron oxides (hematite, magnetite, goethite), clays (illite, and kaolinite), and iron-sulfates. The 'clays' here are assumed to be 80% illite and 20% kaolinite based on Rathod et al., (2020). We assume iron oxides to be strictly stoichiometric (%Fe in hematite Fe_2O_3 = 0.7 and %Fe in magnetite Fe_3O_4 = 0.723). We use the iron-in-illite and iron-in-kaolinite fractions from Journet et al., (2008) and Mermut & Cano, (2001) but also acknowledge the uncertainty in these fractions (Table A.3) could affect mineral emissions by three orders of magnitude. Most iron from the smelting sector is emitted as iron oxides, clays and iron oxides from coal and wood combustion, and as iron sulfates from wood and oil combustion (Rathod et al., 2020). Preindustrial anthropogenic iron emissions, which were mainly from residential wood combustion, are about a factor of 100 smaller compared to the present-day emissions (Hamilton et al., 2020); hence, we do not simulate their transport and radiative interactions assuming they would have been negligible.

Atmospheric modeling: Mineral emissions are transported in the Community Atmosphere Model v6 (CAM6) (e.g. Li et al., 2021) to estimate the direct radiative forcing. Anthropogenic combustion-iron emissions are transported in CAM6 using the Modal Aerosol Module-4 (MAM4,

Liu et al., 2016), with the same segregation of anthropogenic mineral emission mass into the Aitken, Accumulation, and Coarse modes as described in Rathod et al., (2020). The model is run for 18 months starting June 2009, and only the last 12 months are used for analysis. Offline MERRA2 (Rienecker et al., 2011) meteorology was used so the aerosols do not feedback on the meteorology. Emissions such as BC, SO_4, and OM are from the CMIP6 dataset (Hoesly et al., 2018), and dust and sea-salt are simulated prognostically online (Li et al., 2021; Liu et al., 2016).

Optical Properties and DRF: Interaction of radiation with particles in CAM6 is performed in an embedded online radiative transfer model RRTMG (Iacono et al., 2008) that uses a k-distribution model and takes 12 shortwave and 16 longwave wavelength-specific optical properties per species as input. We use the optical properties for hematite, illite, and kaolinite directly from Scanza et al., (2015). We assume iron sulfates to have similar optical properties as hematite since no information was available and because their emissions are small. Two very different optical properties for magnetite are available from observations, highly-absorbing (Moteki et al., 2017) and moderately-absorbing (Querry, 1987; Querry, 1985), with imaginary refractive indices at 0.63 and 0.077 at 550nm, respectively. We use Moteki et al., (2017) values in these simulations to estimate the upper bound in DRF. DRF is then calculated as the difference in the all-sky top-of-atmosphere incoming and outgoing shortwave and longwave radiation caused by iron minerals between 1850 CE and 2010 CE (Equation A.1).

Sensitivity: We transport the combined clays and oxides with central emissions in the base simulation to estimate the net central anthropogenic DRF effect. To estimate the potential warming extent of anthropogenic iron on DRF, we run two other simulations with only central and high oxide emissions since oxides are a factor of 5-8 more efficient in warming than clays are in cooling per unit emission (Figure A.3 and A.4, discussed in Results). For clays, we estimate the upper

bound in their cooling effect by scaling to high emissions using the ∆DRF/∆Emission ratio from the two oxide-only simulations. Central and high values for clays and oxides are selected based on the available bounds in Rathod et al., (2020).

2.2.2 Net Primary Productivity

We estimate the ocean NPP by assuming that anthropogenic soluble iron deposition to any iron-limited region leads to phytoplankton growth (Equation A.2; Boyd et al., 2012; Okin et al., 2011). We use this method in place of a mechanistic ocean model to obtain the first-pass estimate of NPP sustained by anthropogenic iron. Three variables affect the NPP estimation in this method: soluble iron deposition, phytoplankton Carbon/SolubleFe ratio, and iron limitation area definition.

Atmospheric soluble iron deposition: To obtain the present-day soluble iron deposition fields, we transport a mineralogy-based emission inventory (Rathod et al., 2020) in CAM6 for the years 2007-2012 with a 1-year spinup. At emission, depending on the mineral, some fraction of total iron is soluble and the rest is insoluble; the soluble fraction is less than 0.01% for iron oxides, between 1-4% for clays, and 38-80% for iron sulfates (Journet et al., 2008; Meskhidze et al., 2019; Rathod et al., 2020). We run the model with the central observed soluble fractions for all minerals (Rathod et al., 2020). Iron sulfate is the largest contributor to anthropogenic soluble iron emissions (Rathod et al., 2020) and has an uncertainty of a factor of a 2 in its soluble fraction (38-80%; Fu et al., 2012; Oakes et al., 2012; Schroth et al., 2009). Hence, to estimate the possible upper bound of anthropogenic soluble iron deposition due to the upper bound in iron sulfate's soluble fraction, we multiply the modeled soluble iron deposition values with an offline factor of 2. We estimate that anthropogenic total and soluble iron emissions in 1850 were about 1% of 2010 values (Hamilton et al., 2020). For the 1850-to-2010 soluble iron deposition, we assume that anthropogenic iron emissions increased at a compounded annual growth rate of 2% which is roughly the average of global anthropogenic BC and SO_2 emission growth in that period

(Lamarque et al., 2010, Figure A.1); we then assume that deposition is linearly proportional to emissions to obtain the deposition fields for this period.

Phytoplankton carbon-to-soluble iron ratio (C/SFe): The C/SFe ratio represents the growth in phytoplankton carbon (a measure of NPP) by the addition of one unit of soluble iron (Boyd et al., 2012; Okin et al., 2011). We use 3.0×10^4 gCarbon/gSolubleFe as the central value of the phytoplankton C/SFe ratio which is around the mean in observations and modeling studies (Moore et al., 2001; Twining & Baines, 2013).

Iron limitation area definition: Ocean waters with high nitrate concentrations indicate iron limitation; if there were iron in sufficient quantities, phytoplankton would take up the iron and fix nitrate for cell processes (Moore et al., 2013; Schoffman et al., 2016). We use ocean surface nitrate concentration as a proxy to define areas that are iron-limited and hence sensitive to atmospheric soluble iron deposition, which also enables sensitivity simulations on the effect of the iron-limitation area on the estimated NPP. We define iron-limited regions as basins with more than 4 μM (micromolar) surface nitrate concentration, a value that is supported by observational and modeling studies (Krishnamurthy et al., 2009; Moore et al., 2013; Moore et al., 2001). We use present-day (2018) ocean surface nitrate concentrations from Garcia et al., (2019) to define iron-limited regions for the whole 1850-to-2010 period, with the justification that changing emissions, have little effect on these boundaries.

Avoided 1850-to-2010 CO_2 Forcing: NPP is estimated by multiplying soluble iron deposition with C/SFe ratios only in iron-limited regions (Equation A.2). To estimate the cumulative effect of the 1850-to-2010 anthropogenic soluble iron deposition on the atmospheric carbon dioxide concentration and the subsequent radiative forcing, we first convert the estimated NPP in each year to Export Production (EP) which is the fraction of NPP flux that reaches deep oceans and

sequesters carbon for century timescales. We assume that 5% of the NPP converts to EP based on the mean of several estimates (Siegel et al., 2014). We then convert the EP (in units of Pg C/yr) to atmospheric CO_2 removed (in units of ppmv) using a factor of 2.124 ppmv atmospheric CO_2 per Pg C emitted or removed per year (Le Quéré et al., 2018; Sarmiento et al., 2010). We repeat the above steps for the 1850-2010 period to estimate the cumulative atmospheric CO_2 drawdown and the present-day concentrations without this source. After estimating the avoided atmospheric CO_2 concentration due to anthropogenic soluble iron deposition, we estimate the avoided CO_2 radiative forcing assuming a simple relationship between CO_2 concentration and its DRF (Equation A.3; Ramaswamy et al., 2001).

Sensitivity: To understand the possible extent and the relative role of anthropogenic soluble iron among other oceanic parameters in estimating the NPP, we perform sensitivity calculations using upper bounds (Table A.2). We use the high anthropogenic soluble iron deposition values from Rathod et al., (2020). For C/SFe, we use $1.5x10^5$ g/g as the high value, as suggested by Okin et al., (2011). For iron limitation area extent, we use 2μM and 8μM as low and high values in the sensitivity simulations based on Okin et al., (2011).

2.3 Results and Discussion

2.3.1 Direct Radiative forcing

Emissions: We estimate that the total mineral (iron plus the mass of oxygen and other bound species) emissions from anthropogenic combustion activities in 2010 were 11 Tg/yr and 23 Tg/yr in PM_1 and PM_{1-10} fractions, respectively. Clays (illite and kaolinite) contribute more than 85% of the total mass in both the sizes fractions (Table A.4). The central value of global anthropogenic iron oxide emissions is about 1.2 Tg/yr, and the high estimate of iron oxides is about 5.0 Tg/yr, both in PM_1 and PM_{1-10} fractions. Mineral-specific emission values are shown in Table A.4; gridded maps in Figure A.2. The uncertainties in the mineralogical composition of kaolinite and

illite at 0.007-3 %Fe and 0.88-9 %Fe by mass, respectively, affect the clay emission estimates by 3-4 orders of magnitude. Hence, we focus only on central iron-in-mineral fractions for all minerals.

Mineral-specific forcing: Figure 2.1a shows the 1850-to-2010 anthropogenic oxide-only top-of-atmosphere all-sky DRF. The global mean oxide-only warming is about +0.03 W/m^2, with values reaching more than +0.5 W/m^2 over industrialized regions of East Asia. Figure 2.2 shows the global mean DRF by clays and oxides. Clays have a weak net cooling effect, with their global mean DRF value being -0.01 W/m^2, even with an emissions and column burden a factor of between 5 and 8 higher than iron oxides (Figure A.3 and A.4); thus, indicating a smaller role of clays compared to iron oxides in the atmospheric interactions of anthropogenic iron. The global mean 1850-to-2000 DRF by anthropogenic-combustion-iron minerals (sum of cooling clays and warming oxides) is about +0.02 W/m^2 (Figure A.3).

Regionality of forcing impacts: Most warming effect occurs over East Asia (>0.5 W/m^2) and many parts of India and Eastern Europe (>0.2 W/m^2), with oxide DRF values being positive almost everywhere. These positive values are because of the low SSA of magnetite and hematite particles in the 0.1-10 μm diameter size range in the shortwave and because of aerosol-over-cloud effects. The net anthropogenic DRF values over most regions are below 0.1 W/m^2 due to the offsetting cooling and warming effects of clays and oxides (Figure A.3). In the high oxide case (Figure A.3), regional DRF values exceed 0.5 W/m^2 over East Asia, India, Middle East, and Eastern Europe, become more than 0.2 W/m^2 over some parts of North America, Chile, and South America, but remain less than 0.1 W/m^2 everywhere else.

This work's net anthropogenic DRF estimate of +0.02 W/m^2 is consistent with previous studies that estimated the global mean values at +0.01 to +0.05 W/m^2 (Ito et al., 2018; Matsui et al., 2018). Previous studies had overall lower total iron emissions compared to this work but

assumed all iron as oxides, making the iron oxide mass similar. The optical properties chosen are also similar to previous studies. East Asia has the largest emissions of iron oxide and thus the DRF of iron. Iron oxide observations from Japan receiving the East Asian aerosol outflow suggest the central values used in this work for East Asia are well constrained between 500-600 Gg FeO_x/yr (Ohata et al., 2018; Yoshida et al., 2018). However, modeled high values likely better represent the Southern Ocean iron oxide observations than the central values (Lamb et al., 2021; Liu et al., 2022), suggesting the possibility of a wide regional uncertainty, particularly in the Southern Hemisphere. Since anthropogenic effects are very small in regions outside of Asia, Eastern Europe, the Middle East, and North Africa, we suggest that the central DRF values simulated here best represent global anthropogenic iron DRF impacts.

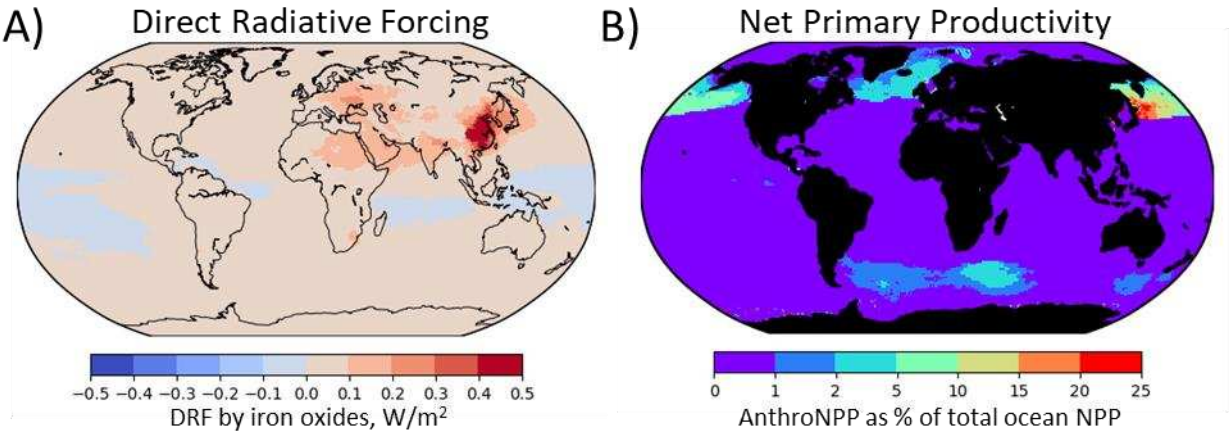

Figure 2.1. (a) Top-of-atmosphere all-sky 1850-to-2010 Direct Radiative Forcing (DRF) in W/m^2 by anthropogenic iron oxides, and (b) 2010 Anthropogenic Fe Net Primary Productivity (NPP) as a percent of total ocean NPP.

2.3.2 Net Primary Productivity

Figure 2.1b shows the anthropogenic soluble-iron-based NPP as the percent of total ocean NPP in the year 2010 using the central deposition, iron limitation, and C/SFe values. Anthropogenic soluble iron deposition sustains 2-15% of the ocean NPP (Behrenfeld & Falkowski,

1997) in the North Pacific Ocean and 0.3 Pg C/yr global total. NPP values and maps are shown in Table A.5 and Figure A.7 for all sensitivity cases of deposition, C/SFe ratio, and Fe limitation area definition.

Regionality of NPP impacts: We find that anthropogenic soluble iron deposition sustains 2-15% of total oceanic NPP in the high-latitude North Pacific Ocean in the central case (Figure 2.1b). It sustains less than 5% of total oceanic NPP in the North Atlantic and Southern Oceans. NPP effect by anthropogenic iron in the Equatorial Pacific Ocean is almost zero. The Southern Ocean impacts directly occur in the plumes from the Brazilian, South African, and Australian industrial and shipping emissions and do not extend beyond 70ºS (Figure A.7). The Equatorial and the North Pacific basins are one of the most productive regions (Figure A.5) but their productivity depends more on atmospheric iron input compared to upwelling and mixing sources due to stratification most times of the year (Moore et al., 2001). Since anthropogenic sources contribute more than 25% of total atmospheric soluble iron input (Rathod et al., 2020), they might act as an important control on phytoplankton growth in these basins where stratification might increase in the future due to climate change (Capotondi et al., 2012; Wang et al., 2015). The North Atlantic Ocean may be more light-limited than iron-limited (Moore et al., 2002), hence these estimates might overestimate the NPP impacts in that basin. The iron limitation definition (ocean waters with more than 2, 4, or 8 μM nitrate) affects mainly the Equatorial and North Pacific and the Atlantic Oceans in terms of the sensitive area but not the Southern Ocean which has more than 20μM surface nitrate concentrations throughout the year (Figure A.6, Garcia et al., 2019). Since the Southern Ocean is iron-limited for phytoplankton growth irrespective of the iron definition limitation, any additional soluble iron input to this basin causes NPP enhancements in this work (Figure A.7), up to 30% in some sensitivity cases.

Impact on atmospheric CO_2: Converting NPP to EP shows the anthropogenic iron-related sequestration removed 0.007 ppmv atmospheric CO_2 in 2010 in the central case (Table A.5). Integrating the NPP over the 1850-to-2010 period, the present-day atmospheric CO_2 concentrations would be 0.33 ppmv higher without the anthropogenic soluble iron deposition. This sequestered 0.33 ppmv leads to an estimated avoided CO_2 forcing of 0.005 W/m^2 (Figure 2.2).

Uncertainty in NPP and CO_2 forcing: The estimated global total anthropogenic soluble iron related NPP in 2010 ranges from 0.2 to 11 Pg C/yr (Table A.5). Under various assumptions of deposition and phytoplankton sensitivity, the anthropogenic iron NPP ranges from 2-50% over the North Pacific and North Atlantic Oceans, and between 0-30% over the Southern Ocean (Figure A.7). Similarly, the present-day atmospheric CO_2 concentrations would be 0.2-13 ppmv higher without this source, converting to an avoided 1850-to-2010 CO_2 forcing of 0.002 to 0.16 W/m^2 (Figure 2.2). The NPP attributable to anthropogenic iron varied by a factor of 4 for the uncertainty in anthropogenic soluble iron emission, a factor of 3 for the uncertainty in the iron limitation region, and a factor of 5 for the uncertainty in C/SFe ratios (Figure 2.2).

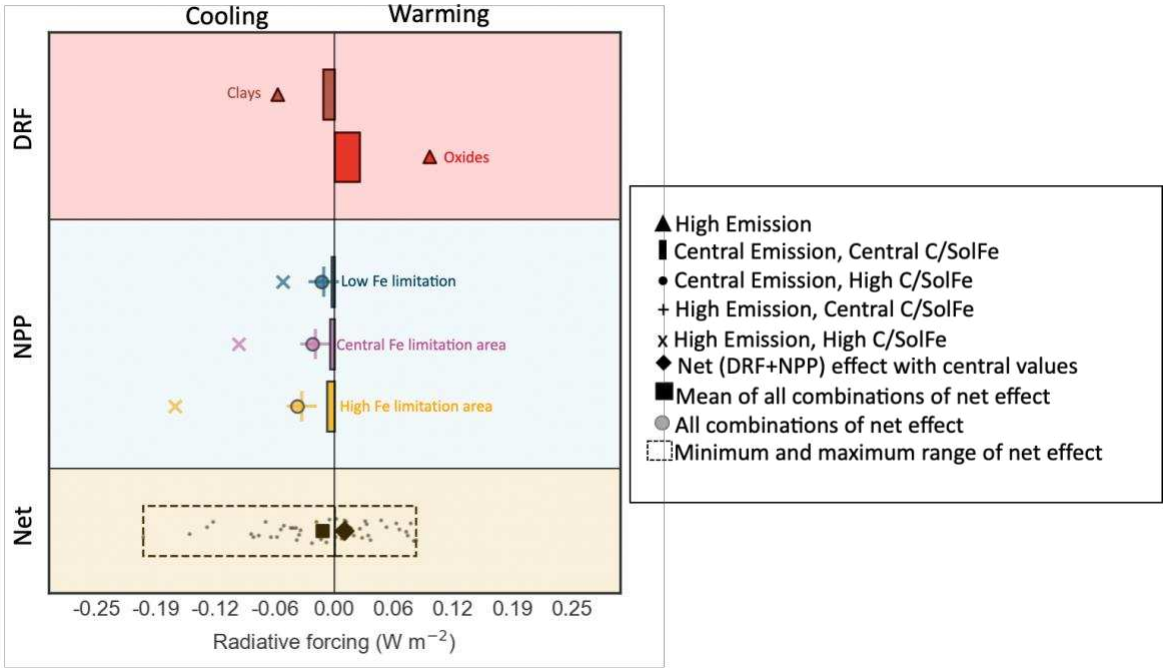

Figure 2.2. The contrasting warming and cooling effects of anthropogenic iron on climate over the Industrial Era. In terms of the direct radiative interactions, clays cool and oxides warm. The biological NPP effect is cooling in nature due to the cumulative 1850-2010 carbon sequestration. Low, Central, and High Fe limitation areas correspond to ocean water with >2, >4, and >8 μM surface nitrate concentrations, respectively. The uncertainty box shows the minimum and maximum values of the net anthropogenic effect (CO_2 cooling plus clays cooling plus oxide warming).

2.4 Implications and Caveats

This work isolates two major effects of anthropogenic iron aerosol on the Earth system and explores their potential importance with sensitivity studies. The global mean anthropogenic iron DRF over 1850-2010 is around 5% of the magnitude of net anthropogenic aerosol direct radiative forcing although in the opposite sign, and 0.7% of all anthropogenic forcing including gases in the 1850-2010 period (Masson-Delmotte et al., 2021). However, its value of +0.5 W/m^2 over East Asia and Eastern Europe is 10 and 200% of the anthropogenic emissions of black and brown carbon, respectively (Ito et al., 2018; Matsui et al., 2018). In the high bound, the anthropogenic

mineral-Fe DRF exceeds +0.5 W/m^2 over many areas and reaches around 10% of the magnitude of net anthropogenic aerosol direct radiative forcing (Figure 2.2 and A.3). Similarly for NPP, the central 0.3 Pg C/yr productivity due to present-day anthropogenic soluble iron deposition is around 0.5% of the total ocean NPP of 40-60 Pg C/yr (Behrenfeld & Falkowski, 1997; Buitenhuis et al., 2013; DeVries & Weber, 2017) and 1850-2010 avoided CO_2 forcing values of 0.002-0.16 W/m^2 due to anthropogenic soluble iron deposition are less than 7% of total anthropogenic CO_2 forcing in this period (Masson-Delmotte et al., 2021). However, anthropogenic emissions sustain more than 10% of present-day total oceanic NPP in the North Pacific basin, thus potentially an important component in a stratifying ocean (Ito et al., 2016; Wang et al., 2015). In its high bound, the estimated global anthropogenic Fe NPP reaches about 11 Pg C/yr, about 20% of the total ocean NPP, and regionally it sustains more than 50% of NPP over the North Pacific Ocean. Both DRF and NPP, depend almost linearly on emissions. Even if near zero, the sign and the magnitude of the net (DRF+NPP) effect become uncertain (Figure 2.2) when the uncertainties in emissions, phytoplankton sensitivity, iron-limitation cut-offs, and mineralogy are considered.

Implications for minerals and anthropogenic emission sectors: We find that iron oxides (magnetite and hematite) exert a net warming effect on the Earth system since they have high radiation absorption properties (Moteki et al., 2017) and very low contribution to soluble iron deposition (Journet et al., 2008; Rathod et al., 2020). Clays and sulfates, on the other hand, exert a cooling effect due to their radiation scattering properties (Scanza et al., 2015) and a high soluble iron fraction (Journet et al., 2008). Since smelting and oil combustion are the largest emitters of iron oxides and sulfates (Rathod et al., 2020), they also act as the largest controls of anthropogenic DRF and NPP.

Caveats: Various assumptions made in this work could affect the DRF and NPP estimates for anthropogenic iron and are summarized here. Optical properties of hematite and magnetite affect their warming potential and observations suggest their absorption potentials might be lower than those used here (Li et al., 2021; Querry, 1987). Aerosols are treated as internally mixed in CAM6; however, the choice of internal mixing can increase forcing estimates by a factor of 1.5 or more compared with external mixing (Matsui et al., 2018). Although iron limitation is well established to exist in widespread portions of the ocean, the NPP oceanic response to atmospheric deposition of iron is uncertain (Mahowald et al., 2018; Moore et al., 2013; Tagliabue et al., 2017), since the biotic response may be limited by other factors such as sedimentary sources of iron or shift in microbe community due to nutrient supply (Boyd et al., 2017; Hamilton, Moore, et al., 2020). However, since the impact of the above assumptions is less than an order of magnitude for both DRF and NPP, smaller than the current uncertainty, the major findings from this analysis are not expected to change even if these are refined. That is, anthropogenic impacts of Fe on atmospheric radiation and oceanic biogeochemistry are smaller on a global-average basis, but their local impacts are non-trivial over East Asia and the North Pacific Ocean, respectively.

2.5 Conclusion

We estimate the radiative and ocean biogeochemical effects of anthropogenic combustion-iron emission relying on mineralogical characteristics, from the power, industrial, residential, and transportation sectors, contrasting with previous studies that estimated the combined effect of dust, fire, and anthropogenic iron emission without considering iron speciation. Anthropogenic combustion-iron emissions cause about +0.02 W/m^2 global mean 1850-2010 top-of-atmosphere all-sky DRF, with strongly absorbing iron oxides causing +0.03 W/m^2 and weakly scattering clays causing -0.01 W/m^2. The deposited anthropogenic soluble iron sustains 0.2-11 Pg C/yr of present-

day oceanic net primary production. Present-day atmospheric CO_2 concentrations would have been 0.2-13 ppmv higher without anthropogenic soluble iron deposition in the last 150 years, indicating an avoided CO_2 forcing of -0.002 to -0.16 W/m^2. The uncertainty in the estimated NPP depends on the uncertainty in anthropogenic iron as much as on other biogeochemical parameters. Smelting and oil combustion are the largest emitters of iron oxides and sulfates (Rathod et al., 2020), and hence are also the largest controls of anthropogenic DRF and NPP, respectively. The net anthropogenic effect in the base case is estimated to be slightly warming, due to the atmospheric impacts being greater than oceanic ones. However, the magnitude and sign of the net effect are uncertain due to high uncertainties in both the effects, occurring mainly due to uncertainty in emission magnitude. Even with the known uncertainty in emissions, both, the DRF and NPP effects, are much smaller than the total anthropogenic. These impacts become important only at regional levels. Anthropogenic iron oxide is estimated to exert a DRF of +0.5 W/m^2 over East Asia and Eastern Europe with a high bound of +1 W/m^2. The anthropogenic soluble iron deposition is estimated to sustain about 10% of the total ocean NPP in the high-latitude North Pacific Ocean, with a high bound of 40%. Anthropogenic soluble iron supply to the North Pacific Ocean hence could become crucial as this basin is predicted to undergo increased stratification in the future due to climate change.

2.6 Data Availability

Anthropogenic soluble iron deposition fields, anthropogenic mineral emissions, and radiation and concentration fields are available at: http://dx.doi.org/10.25675/10217/234658

CHAPTER 3

CONSTRAINING PRESENT-DAY ANTHROPOGENIC TOTAL IRON EMISSIONS USING OBSERVATIONS AND MODELS[2]

3.1 Introduction

Iron-containing aerosol particles are toxic to human health (Wang et al., 2020), affect the atmospheric chemistry of acids (Harris et al., 2012; Kotronarou & Sigg, 1993), absorb and scatter solar radiation (Lafon et al., 2006), and enhance biological growth in nutrient-limited waters after deposition (J. H. Martin et al., 1990). Iron emissions have various sources including dust, wildfires, and anthropogenic combustion (Mahowald et al., 2018). Of these, the anthropogenic component is suggested to exert about +0.5 W/m^2 direct radiative forcing over regions with high coal combustion and smelting, and sustain over 10% phytoplankton primary productivity over iron-limited North Pacific Oceans (Ito et al., 2019; Moteki et al., 2017; Rathod et al., 2020; Yoshida et al., 2018). Yet, the current emission estimates of iron-containing aerosols remain unconstrained. This study aims at constraining the present-day anthropogenic total iron emissions using observations and an atmospheric transport model.

Climate models are used to simulate global radiative forcing and ocean response to emissions of aerosols and gases. Since observations of parameters that represent climate, such as temperature, are scarce and do not extend much into the past, models are also used to reconstruct past climates and predict future impacts. These models use emission inventories of gases and aerosols as inputs, simulate the transport, and are evaluated using present-day observations. To assess whether models using these inventories are producing approximately correct results, modeled concentrations are

[2]This work is in preparation for Journal of Geophysical Research: Atmospheres, as Rathod et al., (2022), Constraining present-day anthropogenic total iron emissions using observations and models.

compared against the observed concentrations (e.g. Mahowald et al., 2009). However, beyond the emission inventories themselves, the modeled concentrations of gas and aerosol species are affected by emissions, transport, and deposition (Menut et al., 2007; Smith et al., 2017). Many models have been tuned to match observed concentrations by simply altering the emissions (Hamilton, Moore, et al., 2020; Matsui, Mahowald, et al., 2018), but "correct" modeled concentrations can also be obtained through compensating errors in the different model processes, for example, high emissions are offset by rapid deposition. When models and observations disagree, emission rates, deposition, and/or transport processes might each be at fault.

Models that represent the life-cycle of iron currently under- and overestimate atmospheric total and soluble iron concentrations over the Southern and Atlantic Oceans, respectively, by over two orders of magnitude (A. Ito et al., 2018; S. D. Rathod et al., 2020a). For example, although the Southern Ocean model underestimation was attributed to underestimated wildfire and anthropogenic emissions, it did not improve even when the highest estimates of those emissions were used (S. D. Rathod et al., 2020a). Observations of iron oxides (hematite and magnetite), which are dominated by anthropogenic sources, suggest that the anthropogenic contribution is underestimated by a factor of 5 over the Southern Ocean in the current inventories, in contrast to the North Pacific Ocean where the current estimates are in line with the observations using isotope markers (Liu et al., 2022; Kurisu et al., 2021; Paulina et al., 2021). Thus, large uncertainties remain around the anthropogenic total iron estimates.

Given the potential contribution of anthropogenic activities to contribute iron into the Earth system and the uncertainty in its emission estimates, this paper addresses the question, "How can a global anthropogenic emission inventory be constrained?"

The term “constraining”, as used in atmospheric aerosol studies, varies among studies. It can either mean determining a factor by which to adjust the inventory to match observations or providing bounds to the inventory. Most previous studies focusing on ‘constraining’ emissions used one emission inventory, supplied it to one atmospheric transport model, and compared simulated concentrations against available observations (Cakmur et al., 2006; R. V. Martin et al., 2003; Zhu et al., 2013). A correction factor, generally a mean or a median of the model-observation comparison, is then determined to nudge or adjust the inventory. The scaled inventory is sometimes fed to the atmospheric transport model to confirm whether the model-observation bias improved. Other studies used the same inventory in different models and compared the multi-model mean with observations to obtain the correction factor for the inventory (Adebiyi et al., 2020; Samset et al., 2014). This approach has been used most often when atmospheric processes after emission dominate the simulated concentration. In this work, we follow the first approach, using a single iron inventory in an atmospheric transport model. We compare the simulated total iron concentrations against observations to obtain a correction factor by region. Unlike many other studies on constraining inventories, we also consider uncertainties by region in the correction factor attributable to inter-annual variability and number of sites. We define the correction factor as the inverse of the median of the model-to-observation ratio in a region. We then define “constraining” as multiplying the central emission inventory by the correction factor and providing uncertainties in the correction factor.

Several factors affect our ability to constrain emissions using model-measurement comparisons. First, the locations of the observations used for constraining simulated concentrations determine whether these simulated concentrations are more affected by emissions or transport. Surface aerosol concentrations in most iron-cycling models are currently constrained

using observations from remote iron-limited oceans (Stelios Myriokefalitakis et al., 2018), where errors in transport and deposition are more likely to influence the concentrations than errors in the emissions (e.g. Tsigaridis et al., 2014). Second, representativeness (how well an observation set represents the temporal and spatial aspects of a region) determines whether it is justified to compare observations that are sparse in space and time. For example, some modeled species like black carbon (Lee et al., 2013) or dust (Mahowald et al., 2002) are often evaluated against long-term data on land. In contrast, modeled iron concentrations have been more likely to be compared with observations by moving ships taken over only a few days (Baker & Croot, 2010; Stelios Myriokefalitakis et al., 2018). These sampling periods might be inadequate to capture the temporal variability of iron concentrations at any location, which may span many orders of magnitude (Smith et al., 2017).

The total and soluble components of anthropogenic combustion-iron contribute to direct radiative forcing and oceanic biogeochemistry, respectively. Anthropogenic total iron emissions are dominated by coal combustion and smelting and contribute to over 0.5 W/m^2 forcing over East Asia. Over other regions, its radiative effects are smaller. Anthropogenic soluble iron emissions are dominated by heavy fuel oil combustion in boilers and ships and wood combustion in the residential and industrial sectors, contribute to over 10% of phytoplankton primary productivity over the iron-limited North Pacific and North Atlantic Oceans. Over other iron-limited basins, however, the impact of anthropogenic soluble is smaller.

In this paper, we constrain the anthropogenic emissions component of the iron cycle, in contrast with most previous studies that did not separate specific sources. Constraining individual sources is important so that sources do not offset each other in a "perfect" model-observation comparison. We first highlight the regions where the simulated anthropogenic contribution to

soluble iron overlaps with the iron-limited ocean basins. We then show the contribution of simulated anthropogenic sub-sources to total and soluble iron concentration. We then compare the simulated anthropogenic total iron concentration against long-term near-source observations, and also apply Positive Matrix Factorization on a subset of the observations to isolate the anthropogenic component. We also compare the simulated anthropogenic iron oxide concentrations to recent observations from East Asia. In the process, we also show the contribution of various model-observation comparison uncertainties such as the spatio-temporal coverage of observations to the adjustment to the central emission values in each of region.

3.2 Methods

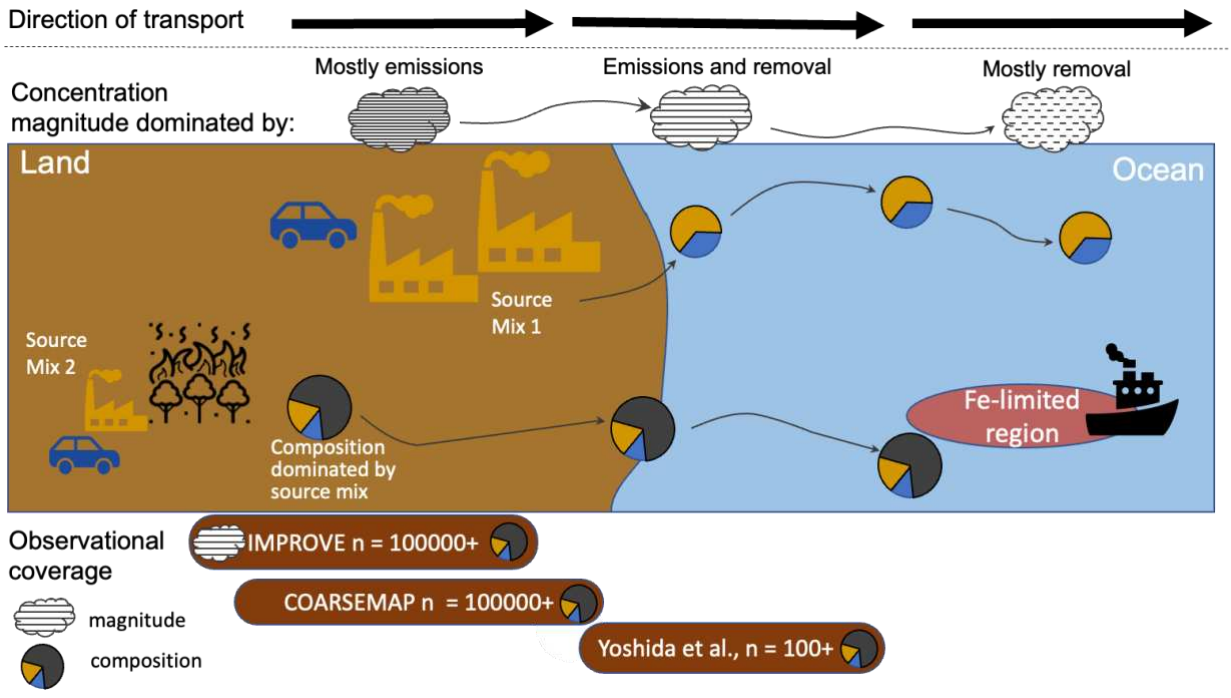

Figure 3.1. A schematic of the sources, observations, and spatial range covered in this work to evaluate anthropogenic iron emissions. Prior work focused on constraining emissions by only looking at iron concentrations in remote regions, where observations are generally scarce and model errors may be more influenced by deposition and transport than by emissions. This work focuses on the source regions with a multi-species approach using long-term observations. n is the number of daily-averaged observations in each site in that observation group.

3.2.1 Overview

Figure 3.1 shows the sources, observations, and spatial range covered in this work. It shows the two broad areas where emission (land, near-source) and transport/deposition (oceans, remote regions) are more likely to dominate any uncertainties in the modeled concentration. Prior work on model-observation comparison focused on remote oceans, where transport or deposition errors are more likely to dominate errors in modeled concentrations, but a lower number of observations are available. We focus on near-source regions to address the proximity and representativeness issue of observations to constrain emissions. In this paper, we constrain total anthropogenic iron emissions and its important sub-source, metal smelting. In the coming subsections, we describe the emission inventories (Sec. 3.2.2), the atmospheric transport model (Sec. 3.2.3), and the observations (Sec. 3.2.4). In Sec. 3.2.5, we compare modeled and observed total iron concentrations at land-based sites where modeled anthropogenic sources dominate. We constrain the anthropogenic total iron emissions using two methods: first in which we use a model filter to identify the locations where anthropogenic contributions are predicted to dominate and second in which we use Positive Matrix Factorization to quantify the anthropogenic contribution in the observations. We compare the simulated iron oxide concentrations against iron oxide observations from Japan to constrain emissions from the smelting industry in East Asia in Sec. 3.2.5.2. And finally, in Sec. 3.2.6, we show the effects of various model-observation comparison uncertainties, such as interannual variability, on the correction factor. The emissions, observations, and analysis methods are summarized in Table 3.1.

Table 3.1. Description of the analyses used to constrain emissions in this paper.

Quantity constrained	Observations	No. locations	Time period	Regions	Distance from source	Analysis

Anthropogenic total iron emissions	COARSEMAP	685 ($PM_{2.5}$) and 185 (PM_{10})	2000-2015	Most in N. America, Europe, Asia, Africa, S. America, Australia	Near	Point-to-point comparisons
Anthropogenic total iron emissions	US-IMPROVE	171 ($PM_{2.5}$)	2010	USA	Near	Positive Matrix Factorization; Point-to-point comparison
Smelting-related iron oxide emissions	Yoshida et al., (2020)	5	2017	Japan	Downwind 1000 km	Point-to-point comparison

3.2.2 Emission inventory

Total anthropogenic iron emissions: Total anthropogenic iron emissions are used directly from Rathod et al., (2020). The global emissions of fine (PM_1) and coarse (PM_{1-10}) mass of anthropogenic iron in Rathod et al., (2020) were 1.1 and 1.0 Tg/yr, respectively. These fine iron emissions were about an order of magnitude higher than most previous studies, while the coarse emissions were within the range of most previous studies (e.g., Ito et al., 2015; Wang et al., 2015; Matsui et al., 2018). These emissions were tested in an atmospheric transport model and yielded improvements in model skill for simulating ambient total iron concentrations compared to previous studies (Rathod et al., 2020).

Fuel-specific emissions: We use the fuel-specific emission output from Rathod et al. (2020) who segregated them into major emission sources based on source characteristics, and also separated them based on solubility. The emission sub-sources are grouped: 'Coal': combustion of coal and other coal-related hard fuels. 'Smelt': Smelting-related emissions from iron and steel, copper, aluminum, zinc, and lead production, along with sintering emissions wherever applicable.

'Oil': combustion of heavy fuel oil (HFO), gasoline, diesel, and natural gas emissions; dominated by HFO in boilers and ships. 'Wood': combustion of wood and solid waste.

Iron oxide emissions: We estimate global anthropogenic iron oxide (iron plus oxygen) emissions by dividing the iron emissions within iron oxides from Rathod et al., (2020) by the iron fraction in that mineral. We assume that all iron-containing iron oxides have a fixed fraction of iron. We assume iron oxides to be strictly stoichiometric (hematite Fe/Fe_2O_3 = 0.7, Magnetite Fe/Fe_3O_4 = 0.723).

Natural sources of total iron: The two other sources of iron, dust and wildfires, emit a large amount of total and soluble iron. These two sources affect the locations where anthropogenic contribution to iron dominates and thus affect the model evaluation, as further described in Sec. 3.2.5. We model dust and wildfire-related total iron emissions following Hamilton et al., (2019). Dust iron is estimated by multiplying the emitted mass of dust (which is tracked online in the model) by an iron fraction which depends on the location (global mean ~3%). Wildfire-iron is estimated by multiplying the wildfire-related black carbon emissions (used from GFED) by observed black carbon-to-iron ratios from various regions.

3.2.3 Atmospheric transport modeling

Model setup: Aerosol emissions are transported in the Community Earth System Model's Community Atmosphere Model v6 (e.g. Hurrell et al., 2013) The model resolution is 0.94º x 1.25 º (latitude x longitude) and has 56 hybrid-sigma pressure levels from 1000 hPa (ground) to up to 2 hPa. Emissions of all other species, such as aerosol precursor vapors and primary carbonaceous carbon, are taken from the Coupled Model Intercomparison Project-5 (CMIP5) emission dataset (Lamarque et al., 2010), and dust and sea-salt emissions are calculated online. The model is nudged using Modern-Era Retrospective analysis for Research and Applications (MERRA2, Rienecker et al., 2011) offline meteorology so that the different representations of anthropogenic iron-

containing aerosol can be compared without feedback on the meteorology. Unless otherwise specified, each model simulation was run for 18 months starting in 2009 with the first 6 months used as spin-up.

Aerosol size treatment: CAM6 uses the Modal Aerosol Module-4 (MAM4, Liu et al., 2016) to track the evolution of aerosol size and composition during its life cycle. Anthropogenic iron emissions are segregated by mass into PM_1 (fine) and $PM_{1\text{-}10}$ (coarse). At the time of emission, 10% and 90% of the anthropogenic PM_1 iron mass is allocated to the Aitken mode and the accumulation modes, respectively. As these particles grow or shrink during transport due to coagulation and condensation/evaporation of vapors, they are reallocated to suitable size bins. All anthropogenic $PM_{1\text{-}10}$ iron mass is emitted into the MAM4 coarse mode (Rathod et al., 2020).

Solubility treatment: We run the CAM6 model with the Rathod et al. (2020) total and soluble iron emissions with an updated atmospheric solubility treatment (MIMI) module (Hamilton et al., 2019). MIMI's integration into CAM6 is described in Hamilton et al., (2019) and Rathod et al., (2020). In summary, MIMI simulates the atmospheric reactions of iron with atmospheric acids and ligands to estimate the conversion of insoluble to soluble iron during transport. Most soluble iron deposition occurs via wet deposition in MIMI. For the fuel-specific solubility simulation described below, we used the Rathod et al., (2020) central fuel solubility (Table 3 in Rathod et al., 2020).

Simulations: We perform three simulations to estimate the anthropogenic total and soluble iron concentrations, estimate the contribution by anthropogenic sub-sources, and estimate the anthropogenic iron oxide concentration. First, we run the CAM6 model with Rathod et al., (2020) emissions and the MIMI module to identify overlapping regions where the anthropogenic supply of soluble iron is important and oceanic waters are iron-limited. Ocean waters with more than 4 uM surface NO_3^- concentrations are defined as Fe-limited (Okin et al., 2011b). The soluble iron

deposition and iron-limited maps are then overlaid. We also use the total iron concentrations of dust, wildfires, and anthropogenic from this simulation to perform the model-observation comparison described in Sec. 3.2.5. Second, we performed a simulation in which anthropogenic source-specific emissions are transported in CAM6 to identify the sources that contribute most to surface-level concentrations of total and soluble iron along with the regions they contribute the most to. Third, since the previous two simulations included only total iron and not mineralogy, we run the CAM6 model with anthropogenic iron oxide emissions to evaluate coal combustion and smelting emissions (Sec. 3.2.5.2).

3.2.4 Observations

This section summarizes the available observations used here to constrain anthropogenic iron emissions in various details. Their spatio-temporal coverage and applications are summarized in Table 1.

COARSEMAP: COARSEMAP is a global, voluntary-contribution dataset compiled by various researchers (http://www.geo.cornell.edu/eas/PeoplePlaces/Faculty/mahowald/COARSEMAP/). COARSEMAP dataset for particulate iron is mainly land-based, and long-term (>1 year at daily-to-monthly resolution). Aerosol samples were analyzed using various methods such as ICP-MS (Inductively coupled plasma mass spectrometry) and XRF (X-ray fluorescence), and hence there might be inter-sample differences Many observations in COARSEMAP are from a country- or state-level agency such as the US-EPA, and the rest are from individual research groups. COARSEMAP's coverage is global but most observations are in the USA for $PM_{2.5}$-Fe and Europe for PM_{10}-Fe (Table B.1 and B.2).

US-IMPROVE: We use the observations of various metals, organic, and inorganic species from the US-IMPROVE (Interagency Monitoring of Protected Visual Environments) network

(http://vista.cira.colostate.edu/Improve/improve-data/), along with the reported uncertainties, to use in PMF to separate source contributions. Although the network was started in 1988, we used data only from the period 2011-2019, avoiding changes in analytical protocols that were implemented starting in 2011 (Solomon et al., 2014). The IMPROVE network collects 24 h samples every third day from midnight-to-midnight local time. The IMPROVE monitor is equipped with a Teflon® filter that is analyzed for PM2.5 gravimetric fine mass and elemental analysis which is performed by X-ray fluorescence (XRF) (Hand et al., 2012).

Yoshida et al., (2020) iron oxide: Atmospheric iron oxide observations are fairly new, and represent emissions from high-temperature combustion activities, mainly smelting and coal combustion (Moteki et al., 2017; Ohata et al., 2018; Yoshida et al., 2018). Yoshida et al., (2020) compiled the observations of particulate iron oxides, obtained using a modified single-particle soot photometer (SP2) described in Moteki et al., (2017). In summary, Moteki et al., (2017) used a modified SP2 which detects light-absorbing refractory aerosols based on intra-cavity laser-induced incandescence. The iron oxide observations represent East Asian continental outflow plumes (site Hedo, and Fukue), fresh urban pollution (Tokyo and Chiba), and pristine Arctic air (Ny-Ålesund).

3.2.5 Model evaluation and uncertainties

3.2.5.1 Anthropogenic total iron

3.2.5.1.1 Global: using a model site selection filter

Modeled surface total iron concentrations (from anthropogenic sources, dust, and wildfires) are compared point-to-point against the COARSEMAP $PM_{2.5}$-Fe and PM_{10}-Fe observations. To ensure that the evaluation is mostly influenced by the anthropogenic component while preserving spatial representativeness, the comparison is performed only at sites where the modeled anthropogenic contribution to total iron is the largest among anthropogenic combustion, wildfires, and dust. For example, if at a given site the anthropogenic, wildfire, and dust iron represented 34%,

33%, and 33% of the total iron, respectively, this site would be included in the evaluation because the anthropogenic fraction was the largest. We refer to this screening as the 'dominant source filter' throughout this analysis. Most COARSEMAP observations are of $PM_{2.5}$ whereas the MAM4 scheme in the CAM6 model does not have a $PM_{2.5}$ cut-off between modes. So, to estimate $PM_{2.5}$-Fe from the modeled values, we use all of Aitken and Accumulation mass and 15% of coarse mode mass (based on the average volume median diameter and geometric standard deviation of the coarse mode in MAM4). For observations of PM_{10}, we use all the MAM4 modes in the comparison.

3.2.5.1.2 USA: using Positive Matrix Factorization

We use PMF on the speciated USA IMPROVE observations to quantify the source contribution by anthropogenic sources. PMF is a statistical model that finds groups of associated species in an observation sample. PMF is a receptor-only model based on mass conservation which requires no previous information about types of sources or their characteristics (e.g. Kim et al., 2003). It assumes the groups of associated species to be constant across time scales. PMF is highly tailored to atmospheric chemistry, specifically toward source apportionment applications (Paatero, 1997; Paatero & Tapper, 1994). It solves the source contribution matrix (Paatero, 1997) and deduces various factors (or groups) that the user must assign to a source/group based on the composition information. PMF has been applied to various real-world cases, for example, Chueinta et al., (2000), Kim et al., (2003), and Ramadan et al., (2000).

The species used for the analysis in the IMPROVE observations are shown in Table S3. Choices related to the selection of species and processing of data are described in Text S1. After species selection and data filtering, we had about 176,000 observations from 148 sites in the USA. The ME-2 (EPA PMF) engine can only calculate 100,000 samples at a time (Paatero, *personal*

communication, 2021), so we split the data in half using the Python pandas "sample" method with random seed 125. Because of the observed heterogeneity of sources and their contributions, PMF is generally operated individually on data from each site and not on the lumped data from multiple sites (e.g. Vecchi et al., 2008). But performing the PMF assessment on 148 sites individually is a resource-heavy task. In this paper, we attempt to obtain a broad quantification of the anthropogenic contribution to total iron concentration over the whole USA, and hence we run PMF on the lumped data from the 148 sites, while acknowledging that the inter-site differences might be considerable (discussed further in Sec. 3.2.2.2). In doing so, we lump multiple "non dust" or "anthropogenic" factors into one factor to deal with their variability between sites but do not lump the "dust" factor because it varies less. between sites. Based on Ulbrich et al., (2009), we use the second derivate maximum of the ratio of Q/Qexp, where Q is the same objective function that PMF tries to minimize, while Q_{exp} is the expected Q if all PMF factors were perfect at explaining the data. Using this analysis, we found that either 9 or 10 factors are the optimal number. We chose 10 factors for this analysis because all 10 made physical sense and were intuitive. Once the 10-factor solution was deemed optimal, we ran 20 PMF runs initialized with random seed 125 and let the software choose the optimal run based on the lowest Q. The results presented herein are the factors produced in that optimal run.

Finally, we compare the modeled anthropogenic iron against the PMF-derived anthropogenic component in the IMPROVE observations.

3.2.5.2 Smelting-related iron oxide emissions

Metal smelting is the largest anthropogenic source of iron and emits most iron as iron oxide due to high-temperature oxidation processes. We perform a point-to-point comparison of modeled and observed aerosol iron oxide using a mineralogy-based inventory and an atmospheric transport model. Iron oxide (hematite and magnetite, Sec. 2.2) is modeled in CAM6 (Sec. 2.3) and compared

against corresponding monthly-averaged observations from Yoshida et al., (2020). These observations are located in Japan (4 sites) and Norway (1 site), all receiving mainly anthropogenic iron oxide flux (Yoshida et al., 2018; Ohata et al., 2019). All the iron oxide observations are in the PM_1 fraction, so are compared only against the sum of modeled Aitken and Accumulation modes.

3.2.6 Uncertainties

The model-observation comparison to obtain a single correction factor by region for the inventory includes many uncertainties, such as interannual variability. In this section, we describe four uncertainties that affect the correction factor: site selection factor, number of sites, interannual variability, and inter-model variability. We then describe the procedure to combine these uncertainties.

3.2.6.1 Site selection filter

We evaluate the anthropogenic total iron concentrations using a model filter in which the model is compared against observations only at sites where the modeled anthropogenic iron emissions contribution is the greatest source among anthropogenic combustion, wildfires, and dust in a specific size range ($PM_{2.5}$ or PM_{10}). A comparison that is less confounded by external factors such as dust and wildfires could be obtained with a stricter cut-off, such as 90 % modeled anthropogenic contribution. However, only a small number of sites would qualify such a high cut-off. To estimate the model bias due to the filter selection, we perform a model evaluation for $PM_{2.5}$-Fe on the COARSEMAP observations in the USA using the 90% anthropogenic contribution to total atmospheric iron cut-off and compare it against the filter used in Sec. 2.5.1.1. We then estimate the uncertainty due to the site selection filter as the ratio of the median model-to-observation ratio of the sites selected with 90% cut-off and the dominant-source filter

3.2.6.2 Number of sites

Except for North America and Europe, most regions in the COARSEMAP data set have fewer than 20 observation sites for both $PM_{2.5}$ and PM_{10} iron. To estimate the uncertainty due to a lower number of sites in many regions, we perform a sensitivity analysis on the North American COARSEMAP $PM_{2.5}$-Fe observations where data from more sites are available, with 527 sites passing the dominant-source filter. We simulate a lower number of sites by randomly selecting a number of sites *n* from the entire data set, determining its median model-to-observation ratio, and dividing it by the median model-to-observation ratio for the whole data set. We repeat this sampling and determination 500 times for each value of *n*, estimating the uncertainty in the median model-to-observation ratio as the 5^{th} and 95^{th} percentiles. We conduct this experiment for values of *n* that are approximately geometrically spaced: 1, 2, 3, 4, and then increasing by a factor of about 1.6 until n=527

3.2.6.3 Interannual variability

Many sites in regions such as South America and Africa have data spanning only 1-2 years compared to North America where the iron observations are from more than10 years for most sites. The model was run only for the year 2010, and hence comparing it against observations other than from 2010 or a long-term average will contain a bias due to interannual variability (IAV) bias. To estimate the IAV bias, we use the yearly averaged data from IMPROVE from 2006-14 (4 years each around 2010) and compare each of the yearly averaged data and 2006-14 observed mean with the modeled 2010 concentrations. We then divide the median model-observation ratio from each of these years by the median model-to-observation ratio from the mean. We then present the uncertainty due to IAV as the 5^{th} and the 95^{th} percentiles of the obtained ratios of all years.

3.2.6.4 Inter-model variability

We used only CESM-CAM6 atmospheric transport model to evaluate the emission inventory. However, selecting any other model (such as GEOS-Chem) would lead to a different model-observation bias because of different aerosol representation and model resolutions. To estimate the uncertainty due to different model outputs, we refer to literature where different atmospheric transport models were fed the same aerosol emission inventory and meteorological conditions. Chen et al., (2019) found the inter-model standard deviation to be about 20% of the mean for near-source regions. Thus, about 20% of the model difference from observations can be attributed to model selection alone.

3.2.6.5 Combined uncertainty

We assume that the uncertainties discussed above are independent of each other, and combine them in a quadrature (e.g. Streets et al., 2003). For the site selection filter parameter, we use the ratio of the median model-to-observation comparisons in the two filters as is. For the number of sites and interannual variability parameters, we use the 5^{th} and 95^{th} percentiles as the 95% confidence intervals. For the model selection parameter, we use 1.2 as the 95^{th} percentile uncertainty. We then calculate the low and high bounds of the confidence intervals individually based on the low and high estimates of the uncertainties in the individual parameters.

3.3. Results

In this section, we first determine the simulated regions where a high anthropogenic contribution to atmospheric soluble iron overlaps with iron-limited oceanic phytoplankton growth areas (Sec. 3.3.1). We then show simulated anthropogenic source-specific contributions to total and soluble iron (Sec. 3.3.1.2). In Sec. 3.3.2, we evaluate the modeled values against observations for various anthropogenic emission sources in multiple regions. In Sec. 3.3.3, we show the

influence of various model-observation comparison parameters on the uncertainty in constraining the inventory.

3.3.1 Regions where the anthropogenic contribution is important

3.3.1.1 Regionality

Figure 3.2 shows the annual average contribution of the anthropogenic soluble iron to total atmospheric soluble iron (dust, wildfires, and anthropogenic) deposition, with dots and hatches representing the central and upper bounds in the area of iron limitation for oceanic phytoplankton growth (see Sec. 2.3 for the definition of iron limitation). Of the Fe-limited regions, anthropogenic sources supply 15-50% of atmospheric soluble iron to the North Pacific, Equatorial Pacific, and North Atlantic waters. The anthropogenic contribution to atmospheric soluble iron in Fe-limited areas such as the Southern Ocean is less than 15%. Hence, for the model evaluation for anthropogenic contribution to total and soluble iron, we focus mainly on the overlapping areas where the basin is iron-limited and where the anthropogenic contribution to soluble iron is high.

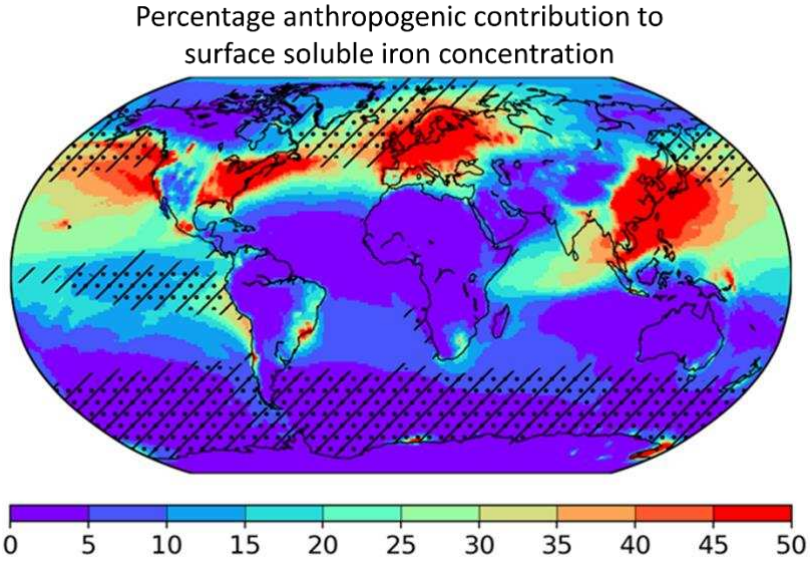

Figure 3.2. The background shows the percentage anthropogenic contribution to atmospheric soluble iron deposition, and the dots and hatches show central and upper bounds, respectively, of the annual-average iron-limitation area.

3.3.1.2 Dominant anthropogenic sources

Figure 3.3 shows the simulated anthropogenic source-specific contribution to surface concentrations of total and soluble iron. Smelting-related emissions dominate the anthropogenic total iron concentration in most areas, with contributions in many areas exceeding 60%. Coal combustion is another dominant source that supplies anthropogenic total iron to industrial areas of North America, East Asia, and Europe. For soluble iron, however, heavy fuel oil and other liquid-fuel combustion in industrial/shipping sectors and wood combustion in industrial and residential sectors contribute the highest anthropogenic soluble-iron fractions, especially over iron-limited ocean waters. Hence, constraining the oil and wood combustion iron emissions is crucial in constraining the anthropogenic soluble-iron flux whereas smelting and coal combustion have higher fractions of the total anthropogenic iron flux.

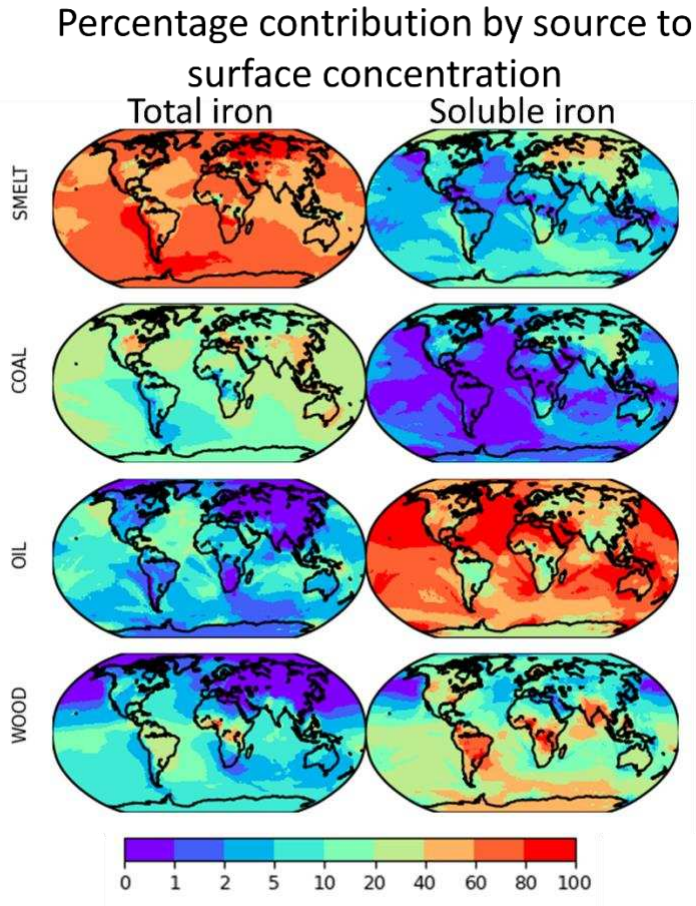

Figure 3.3. The simulated percentage contributions to total (left panel) and soluble (right panel) anthropogenic iron surface concentration by its sub-sources.

3.3.2 Comparison with observations

3.3.2.1 Anthropogenic total iron emissions

3.3.2.1.1 Global: using a model filter

Figures 3.4a and 3.4b show boxplots of the model-observation comparison for the annual average total iron concentrations for various regions in $PM_{2.5}$ and PM_{10} fractions, respectively. Over 90% of the modeled values are within an order of magnitude of the observations for both PM sizes, with over 50% sites within a factor of 5 (Figure 3.4a and 3.4b boxplots, 25-75% quartiles). Maps with modeled concentrations and observation locations are shown in Figures B.1 and B.2 for $PM_{2.5}$ and PM_{10}, respectively. $PM_{2.5}$-Fe is observed mostly in North America and has relatively fewer observations everywhere else (87% of observation sites are in North America). The coarse mass (PM_{10} minus $PM_{2.5}$) represents 50% of emissions and 30% of concentration over remote oceans in the model (Rathod et al., 2020), but the number sites measuring it (both individually or as a sum with fine iron) are even less across the world compared to $PM_{2.5}$, with most sites in Europe and globally only 20% of the number of $PM_{2.5}$-measuring sites. For Europe with comparable observing sites for both the PM sizes, the $PM_{2.5}$-Fe is overestimated in the inventory by a factor of 1.2, while the PM_{10}-Fe is underestimated by a factor of 2.

Two continental emissions regions contribute to the majority of soluble iron deposition in the North Atlantic and North Pacific Oceans: North America and East Asia, respectively. Additionally, shipping emissions within these oceanic regions also contribute to deposition in these regions. Emissions from western South America also contribute about 15% of total atmospheric soluble iron to the iron-limited Equatorial Pacific Ocean (with higher soluble iron fractions close to the continent). Of the three source regions discussed here, however, South America and Asia have

much fewer observations (2 and 29, respectively) that passed the dominant source filter compared to North America with 527 sites. We find that the model underestimates concentrations over North America by a factor of 2 and represents concentrations with a factor of 1.1 over for Asia for $PM_{2.5}$-Fe and a factor of 5 and 2 respectively for PM_{10}-Fe although much fewer observations are available for the PM_{10}-Fe size. The correction factors for each of the regions are summarized in Table 2 for $PM_{2.5}$-Fe. We apply the following correction factors with uncertainty as the 5th and 95th percentiles of the inverse of the model-observation ratio: 2 (1.1-3.3) for North America, 0.67 (0.5-0.87) for South America and Africa, 0.9 (0.5-1.5) for Europe, 1 (0.56-1.6) for Asia, and 2.5 (2-5) for Australia/New Zealand.

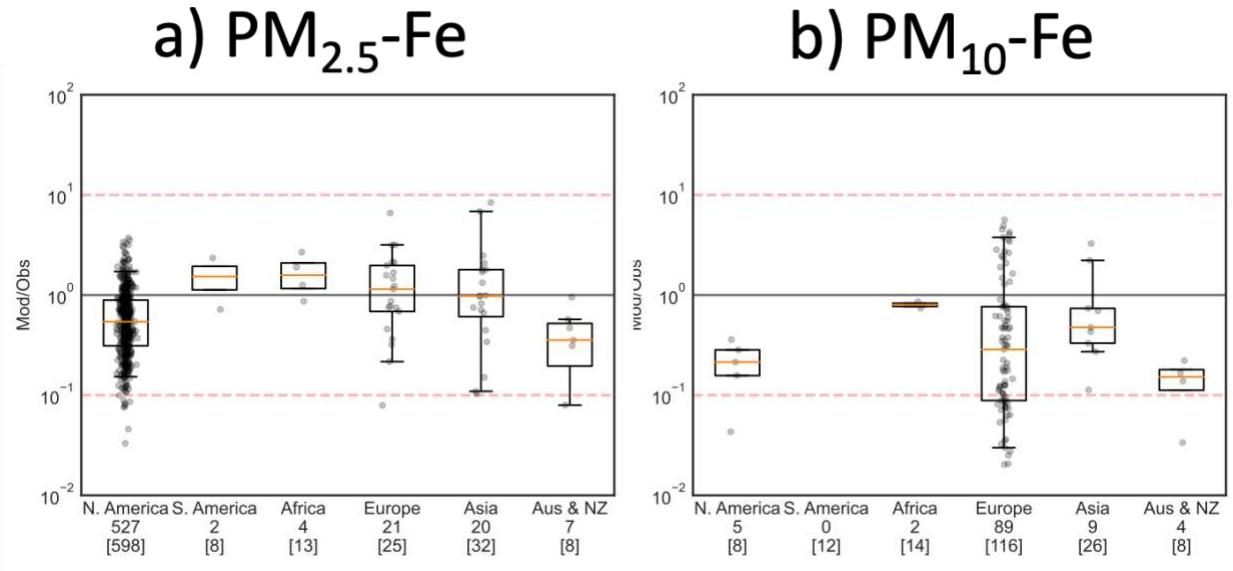

Figure 3.4. Boxplots of model-observation comparison of $PM_{2.5}$-Fe (a) and PM_{10}-Fe (b) total iron concentration in various regions. Comparison is performed only at sites where the anthropogenic contribution to iron in these size ranges is the highest of all atmospheric sources (dust, wildfires, and anthropogenic combustion). Each dot represents the ratio of modeled 2010 mean concentration to observed temporal-mean concentration for each site. Values below the region name show the number of observation sites that passed the filter and were used in the evaluation. Values in brackets show the total numbers of sites in each region. Whisker length is 5th-95th percentiles.

3.3.2.1.2 USA: using Positive Matrix Factorization

The PMF output is in the form of factor profiles, where each factor represents a source- or species-group based on the association of species in occurrence in the observation samples. We identify and name these factors based on existing knowledge of specific species contributions from different sources and the contribution to key, representative species (Figures B.3 and B.4). For example, a factor with a dominant contribution of Al, Si, and Ti is identified as Dust. SO_4 is associated with coal combustion and thus the factor contributing most SO_4 is identified as Coal combustion. Similarly, we named a factor "biomass burning" based on its richness in K, Na, and Cl for sea salt, and we named a factor "oil combustion" due to contributions from V, Ni, and SO_4. Many aspects affect the PMF results and how species are grouped into factors: for example, most SO_4 is not directly emitted (as primary) but is rather produced in the atmosphere via the oxidation of SO_2 and hence its association with other species would depend on the age of the airmass (Yuan et al., 2006). Moreover, co-location of emission sources also leads to a factor that has fingerprints from two or more sources. Using all-USA observations together in our analysis also led to the "mixing" of various factors for iron.

While we identified a separate 'coal combustion' factor using its SO_4 contribution, we also found that this factor did not contribute to iron emissions which contrasts model findings in Figure 3 (potentially because SO_4 depends on the airmass age in addition to the source; hence it may not be well correlated with other emissions from coal combustion). Even though PMF can separate many factors that have a distinct source profile along with representative marker species, it also fails to reproduce the observed source profiles of many sources such as heavy fuel oil and wood combustion (Tables B.4 and B.5). This mismatch could be due to the generalization of source profiles across the USA and co-emissions with other iron sources in various regions. For example,

over coastal areas, heavy fuel oil is associated with sea-salt, but over inland areas, it is associated with SO_4 emissions and other industrial PM emissions.

Even though running PMF on a lumped set of observations from all over the USA led to the mixing of sources in different factors and thus no clear-cut factor separation for anthropogenic sub-sources, it does represent dust consistently over all the sites and reproduces a dust source profile consistent with observations (Table B.6). Since our confidence in individual factors for anthropogenic sub-sources is much lower than in dust for iron, we compare the modeled anthropogenic iron concentrations against the non-dust iron concentrations in PMF. However, this non-dust-Fe consists of anthropogenic combustion sources as well as wildfires. Figure 3.5a shows the model (anthropogenic and anthropogenic+wildfire) and observation (non-dust-Fe in PMF) comparison for iron over the US-IMPROVE observations. The modeled concentrations in both the cases (anthropogenic and anthropogenic+wildfires) are higher than the non-dust-Fe concentrations in PMF in ~85% of the sites over the USA and 97% of the sites are within an order of magnitude. The simulated wildfire contribution is about 30% of the anthropogenic component over the USA. The median model-to-observation ratio is 1.7 and 2.3 for the anthropogenic and anthropogenic+wildfire cases, respectively (Figure 3.5b). The simulated dust Fe is underestimated compared to the PMF dust Fe by an order of magnitude (Figure B.5).

The model underestimates the overall $PM_{2.5}$-iron (sum of anthropogenic combustion, wildfires, and dust) over North America when compared to the COARSEMAP dataset (Figure 4a). However, the model overestimates the anthropogenic combustion and wildfire components compared to PMF in the IMPROVE dataset. This mismatch between the two comparisons (COARSEMAP and PMF) over North America is because the model has lower dust than estimated by the PMF (Figure S5) as also reported in other studies (Kok et al., 2021) and because the site

selection filter used in Figure 3.4a does not entirely eliminate the influence of Fe from dust and wildfires (discussed further in Sec. 3.3.3.1).

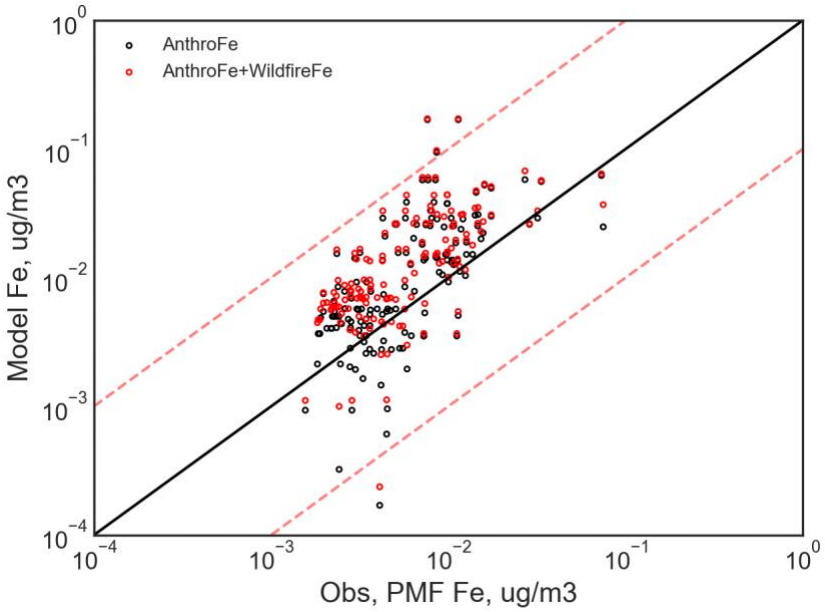

Figure 3.5. Scatterplot of the model anthropogenic (black) or model anthropogenic+wildfire (red) and observed (non-dust Fe in PMF) iron concentrations. Each dot represents an USA-IMPROVE site used for PMF analysis. The non-dust-Fe component is identified as the total minus the dust-Fe component, and is used here instead of individual components because of the higher confidence in PMF dust-Fe than other factors.

3.3.2.2 Smelting emissions

Rathod et al., (2020) estimated the global anthropogenic emissions of iron oxides to be 1.4 Tg/yr (0.1-6 Tg/yr 95% CI) in the PM_1 fraction with smelting contributing about 80% of these emissions. Note this is the PM_1 fraction instead of $PM_{2.5}$ discussed earlier, due to the size cut-off in the SP2 instrument used in the observations in Yoshida et al., (2020). The fine iron oxide emissions from East Asia (China, Chinese Taipei, Hong Kong, S Korea, and N Korea) in this inventory are about 0.6 Tg/yr (central estimate, which is near the upper estimate of 0.5 Tg/yr estimated by Yoshida et al., (2018) using the observed relationship between iron oxide and BC in the outflow from that region.

Figure 3.6a shows the modeled annual average contribution of fine anthropogenic iron oxides to the total atmospheric iron oxides (anthropogenic + dust). The anthropogenic contribution dominates the surface iron oxide concentration over the industrial regions of East Asia including Japan, Europe, Eastern USA, and Eastern Brazil, also supported by particle morphology observations from Japan and Switzerland (Yoshida et al., 2020). Figure 3.6b shows the model-observation comparison of fine iron oxide, in ng/m3, at the ground-based sites compiled by Yoshida et al., (2020). The modeled values in Figure 6b show only anthropogenic iron oxides; Figure B.6 includes dust iron oxides but the difference is negligible due to low dust contribution in the regions where the observations are. The model overestimates iron oxide concentration by a factor of 3 at Fukue, a factor of 1.5 at all other Japanese sites, and underestimates by an order of magnitude in Ny-Alesund, which is the only location outside of Japan and is in the Arctic North Atlantic. This comparison, however, is within the range of model-observations ratios seen for total iron in COARSEMAP sites which are nearer to the sources than compared here. Both, the model underestimation, and the overestimation could be due to uncertain deposition and other transport factors, and these factors could be more uncertain at Ny-Alesund due to its large distance from anthropogenic emission sources compared to the Japanese sites which are closer to emission sources. Thus, the best estimates of anthropogenic iron oxide (Fe_3O_4) emissions from East Asia could be around 0.4 Tg/yr (0.6 Tg/yr previous estimate divided by 1.5, the factor of overestimation), indicating the anthropogenic iron emissions from smelting and coal combustion to be around 0.28 Tg/yr (0.4 Tg/yr Fe_3O_4 multiplied by 0.72, the fraction of Fe in Fe_3O_4).

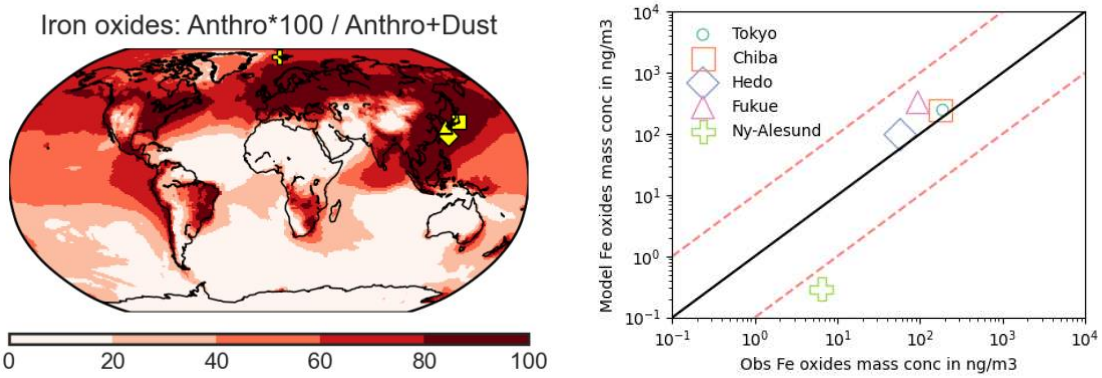

Figure 3.6. a) Percentage contribution of fine anthropogenic iron oxides to total fine (anthropogenic + dust) iron oxides. Yellow triangles show the observation locations and b) Model-observation comparison of fine iron oxides at monthly averages in five ground-based sites. Observations are from Yoshida et al., (2020).

3.3.3 Uncertainties

3.3.3.1 Site selection filter

In the evaluation for anthropogenic total iron, we use the 'dominant-source filter' to select sites for comparison. This filter does not exclude sites with substantial iron concentrations from dust and wildfires; if those sources are overestimated in the model, then the apparent model-observation ratio for total iron would be greater than that for anthropogenic iron. Figure 3.7a compares the distribution of model-observation ratios for the North America COARSEMAP data for $PM_{2.5}$-Fe using two filters: the dominant-source filter and another, stricter filter where the modeled anthropogenic contribution is more than 90% of atmospheric iron. The median model-observation ratio for the 90% cut-off filter ("Anthro>90%") is a factor of 1.3 higher than the dominant-source filter ("Anthro = max of all"), indicating that the overestimation of dust and wildfire emissions is confounding the comparison. However, there is a tradeoff between isolating modeled anthropogenic contribution and greater coverage with more sites. The 90% cutoff filter excludes 60% of the sites in the USA (220 sites for the 90% filter vs 527) and 70% of the sites outside the USA (16 sites vs 54). We infer that, over North America, the overall model-observation ratio should be increased by a factor of 1.3 to reflect a group of sites that are less influenced by

dust and wildfire emissions. We apply the same factor of 1.3 to other regions assuming the model-observation comparison is also affected by under- or overestimated dust and wildfires there, acknowledging that this correction lacks observational support but cannot be ignored.

3.3.3.2 Number of sites

Figure 3.7b summarizes uncertainty caused by a limited number of regional observation sites, using the COARSEMAP dataset over North America. Each dot represents the ratio between the median model-to-observation ratio from a random selection of *n* sites, simulating a smaller collection of sites, and the median model-to-observation ratio of all sites. The data and boxplot for each value of *n* show the results of 500 such simulations. When the number of sites is below 3, the inferred model-to-observation ratios vary by as much as a factor of 3; however, the uncertainty diminishes rapidly with an increasing number of sites, falling to about 30% for about 20 sites. We apply the following uncertainty factors (as 5^{th} and 95^{th} percentiles) based on the number of sites in each region: 1 for North America (n=527), 0.3-2.5 for South America (n=2), 0.5-2 for Africa (n=4), 0.75-1.4 for Europe (n=21), 0.75-1.4 for Asia (n=20), and 0.5-2 for Australia/New Zealand (n=7).

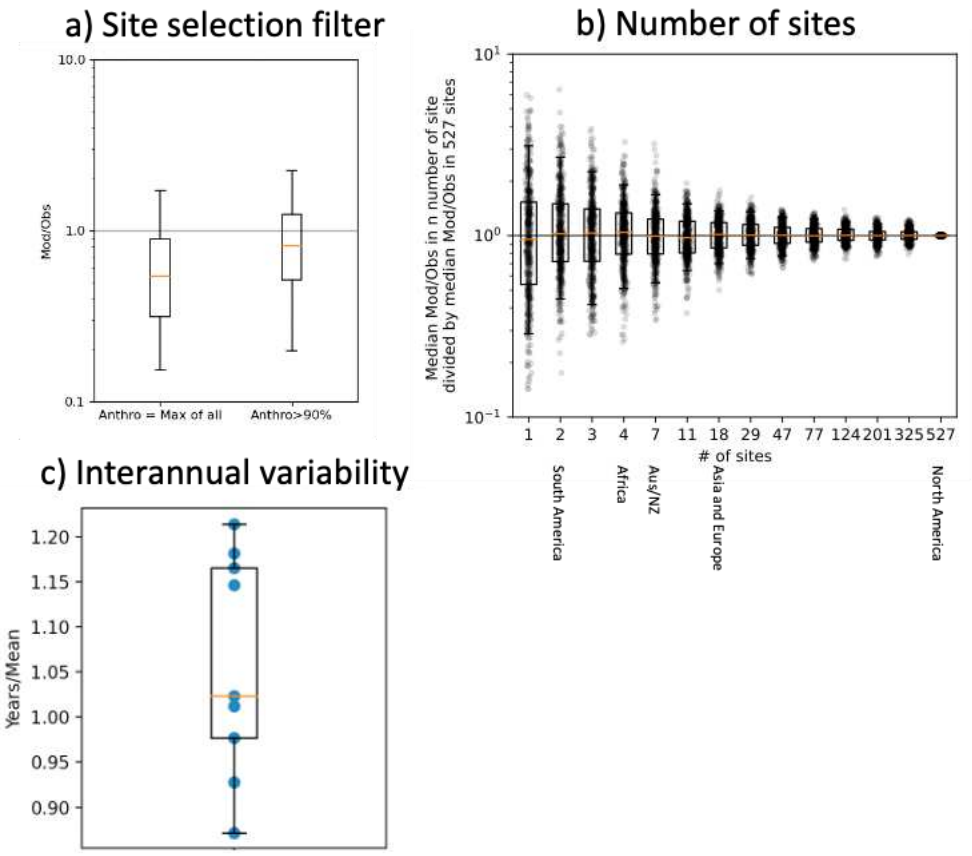

Figure 3.7. (a) Distribution of the model-observation ratios in the North American COARSEMAP sites for $PM_{2.5}$ total iron concentrations with the two filters described in Sec. 2.5.3.1. "Anthro = max of all" shows the results from sites where the modeled $PM_{2.5}$ anthropogenic emissions were a larger contributor to total iron than both dust and wildfires. "Anthro>90%" shows the filter in which only the sites where the modeled anthropogenic contribution was >90% of the total $PM_{2.5}$ atmospheric iron were selected. (b) Distributions of total iron concentrations shown as the ratio of the median model-to-observation ratio from a random selection of *n* sites and the median model-to-observation ratio of all sites Distribution is shown from 500 simulations. (c) Distribution of the interannual variability in the model-to-observation ratio for North America IMPROVE $PM_{2.5}$-Fe observations. Each dot shows the ratio of a year's median model-to-observation ratio and the 2006-2014 mean's median model-to-observation ratio. Whisker length in all the plots are 5^{th}-95^{th} percentiles.

3.3.3.3 Interannual variability

Observed concentrations may not reflect the average if the measurement duration is short. Figure 3.7c summarizes the ratio of the median model-to-observation ratio for each year and the median model-to-observation ratio of the mean (2006-14) for sites in North America. This distribution shows the uncertainty due to comparing any random year with the model compared to

a long-term average. While most sites in all regions have data longer than a year, many sites have coverage of less than a year. We apply the uncertainty of 0.85-1.2 as the 5th and 95th percentiles to all regions to account for the model-observation bias due to the temporal coverage of observations.

3.3.3.4 Combined uncertainty

Table 3.2 summarizes the central adjustments to the inventory and their uncertainties in each region for $PM_{2.5}$-Fe. The Correction Factor is the factor by which scaling the inventory would give a better model-observation comparison in that region. Uncertainties of 5% and 95% confidence are shown as the multipliers to the Correction Factor. The Correction Factor Range, also a 5%-95% confidence interval, encapsulates the combined effect of all uncertainties. The model-observation spread is the dominant uncertainty in North America, Europe, and Asia, whereas the number-of-sites parameter is the dominant uncertainty in South America, Africa, and Australia/New Zealand. The site selection uncertainty is the second largest uncertainty in all the regions. In all regions except North America and Australia/New Zealand, the Correction Factor range varies from less than one to above one, indicating that the *a priori* estimate has usually been within the range of uncertainty.

The model-observation spread is not really an uncertainty due to external parameters but it is a variability that occurs because of fine-resolution spatial discrepancies in the inventory. Regions with a low number of sites do not capture this variability and thus the uncertainty attributed to the model-observation spread appears to be low in those regions. However, the 'number of sites' uncertainty offsets this uncertainty due to model-observation spread in those regions, but most likely underestimates the error. This underestimation in the error in the 'number of sites' uncertainty is because of the assumed extrapolation of US data to other regions that might have more spatial heterogeneity in emission sources and contributions. For example, while 10 sites can

capture the USA's spatial variability to about 20% uncertainty (25-75 percentiles) compared to 520 sites, 10 sites might not be able to capture the same amount of variability for all of Asia (that includes Middle East, Russia, India, and China) or Africa.

The IAV and model-specific (using only one model in place of a model ensemble) uncertainties come from data sources other than COARSEMAP. While coarse (PM_{10} minus $PM_{2.5}$) Fe contributes about 50% and 30% of the anthropogenic total and soluble iron emissions, respectively, its contribution to the remote ocean is rather low because of its limited long-range transport (Rathod et al., 2020). Moreover, most sites do not measure iron in coarse particles. Hence, observational data sets do not allow similar estimations of uncertainty for the PM_{10}-Fe component. It is probably higher than the uncertainty in $PM_{2.5}$-Fe, because the comparison would be more greatly affected by the uncertain contribution of dust and wildfires Hamilton et al., 2019; Myriokefalitakis et al., 2018).

Table 3.2. Summary of regional model evaluation for $PM_{2.5}$-Fe. Uncertainties are absolute multipliers and are shown as 5-95 percentiles. Correction Factor is the factor by which scaling the inventory in that region should lead to a better model-observation comparison. The cumulative uncertainty in the Correction Factor is shown as 95% CI. Parameters representing the highest uncertainty in a region are in bold.

			Uncertainty (as multipliers to the Correction Factor)					
Region	**n**	**Correction Factor**	**Mod/Obs spread**	**IAV[a]**	**# of sites**	**Atm. Model[b]**	**Site selection filter[a]**	**Correct Factor Range (95% CI)**
North America	527	2	**0.55-1.67**	0.85-1.2	1	0.8-1.2	1.3	1-3.5
South America	2	0.67	0.77-1.3	"	**0.3-2.5**	"	"	0.5-1.7
Africa	4	0.67	0.77-1.3	"	**0.5-2**	"	"	0.4-1.4
Europe	21	0.9	**0.56-1.64**	"	0.75-1.4	"	"	0.5-1.7
Asia	20	1	**0.56-1.67**	"	0.75-1.4	"	"	0.6-1.9
Aus/NZ	7	2.5	0.8-2	"	**0.5-2**	"	"	1.5-6

[a]Applied to all regions, [b]Applied to all regions, from Chen et al., (2019)

3.4 Implications

The constraining exercise described above suggests bounds for the anthropogenic total iron emissions in several regions. Total iron is important for direct radiative forcing, and soluble iron for oceanic biogeochemistry. Since the radiative and biogeochemistry impacts of anthropogenic iron are dominant over East Asia, and North Pacific and North Atlantic, respectively (Rathod et al., 2022), we discuss the implications of the constraining procedure for emissions from source regions of East Asia and North America. We compare the constrained emission estimates, in which a Correction Factor with uncertainty is applied to the central estimate of emission rate in each region, with *a priori* emission estimates.

Over Asia (including Middle-East, Russia, India, China, East Asia, and South East Asia), the median Correction Factor is 1, and the uncertainty is 0.6-1.9 (95% CI). The current anthropogenic total iron emissions from Asia are about 0.8 (0.15-4) Tg/yr, or about 75% of the global total (Rathod et al., 2020). Thus, the uncertainty estimated in this study is smaller than the uncertainty of the *a priori* estimate. However, the iron oxide observations suggest the central bound could be lower by a factor of 1.5 for East Asian smelting and coal combustion emissions which dominate the radiative effects. This is in line with the model-observation comparison at the two sites in China where the model overestimates by a factor of 2. Thus, the direct radiative effect could be lower than 0.5 W/m^2 averaged over East Asia as estimated by Rathod et al., (2022). While the East Asian soluble iron flux is suggested to sustain about 10% of North Pacific Ocean phytoplankton productivity, we were not able to constrain its dominant sources (heavy fuel oil and wood combustion) due to a lack of speciated data.

Over North America (USA), the median Correction Factor is 2, with a range of 1-3.5 (95% CI). The *a priori* estimates of anthropogenic total iron emissions are 0.1 (0.02-0.5, 95% CI) Tg/yr,

compared to the 0.2 (0.1-0.35, 95% CI) Tg/yr estimated based on the Correction Factor from the total iron observations. The *a posteriori* central estimate could be about 0.06 Tg/yr based on the PMF comparison. The direct radiative effects of anthropogenic combustion-iron over the USA are small (<0.1 W/m^2), and thus the uncertainty of a factor of 2 in its total iron emissions does not matter compared to those from other anthropogenic species such as black carbon and sulfur dioxide. The North American contribution to soluble iron, however, to the North Atlantic Ocean is non-trivial and sustains 5-10% of phytoplankton productivity (Rathod et al., 2022). The soluble iron emissions sources such as heavy fuel oil and wood combustion were not constrained because of the relatively smaller (<1%) contribution to total iron by these two sources and because of the PMF limitations in resolving site-specific source contributions in a large dataset as IMPROVE.

3.5. Summary

Anthropogenic iron forms an integral part of the input to the models that estimate the present-day atmospheric and oceanic cycling of iron, yet its emission estimates remain unconstrained. In this work, we used an atmospheric transport model, an anthropogenic iron emission inventory, and long-term near-source observations from various regions along with Positive Matrix Factorization to evaluate the modeled concentrations. The major findings of this work are:

- North Pacific and North Atlantic Oceans are the two iron-limited basins that overlap with atmospheric soluble iron deposition.
- Among the anthropogenic sources, coal and smelting contribute the most to modeled total iron, and oil and wood combustion contribute the most to soluble iron concentrations, respectively.

- The model underestimates total iron concentration (dominated by anthropogenic contribution) compared to the COARSEMAP observations of $PM_{2.5}$-Fe over North America and Australia/NZ and overestimates in South America, Africa, Europe, and Asia.
- Anthropogenic PM2.5-Fe iron emissions are constrained to a factor of 3 in all regions except in Aus/NZ where it is a factor of 6. These constraints are narrower than the factor of 5 globally in the *a priori* inventory.
- The dominant cause of uncertainty in anthropogenic PM2.5-Fe varies by region: model-observation spread is the dominant uncertainty in North America, Europe, and Asia, whereas the number-of-sites parameter is the dominant uncertainty in South America, Africa, and Australia/New Zealand.
- Even when data from 148 sites from the contiguous USA were lumped, PMF was able to reproduce robust dust source profiles. However, its resolution of the non-dust sources was not robust and there was a high amount of inter-factor mixing of sources.
- When lumping all non-dust-Fe (Total-Fe minus dust-Fe) values from PMF over the USA, the simulated anthropogenic total iron concentrations are overestimated by about factor of 2. The model underestimates dust-Fe concentrations by about an order of magnitude almost everywhere over the USA, consistent with prior work.
- As low as 10 sites can aid in constraining the simulated values to a factor of 2, assuming the regional variability in iron concentrations is similar to the US.
- Smelting contributes about 80% of the global fine anthropogenic iron oxide emissions, which cause over 0.5 W/m^2 atmospheric radiative forcing over regions with high emissions (Rathod et al., 2022). Comparison of simulated iron oxide emissions (a proxy of high-

temperature smelting) from East Asia with observations from Japan suggests the East Asian smelting emissions are overestimated in the model by a factor of 1.5.

- The total-iron component affects direct radiative forcing and the soluble component affects biogeochemistry. However, because the soluble-iron component is emitted from sources that do not emit considerable total iron, they could not be isolated and identified even in speciated observations.

CHAPTER 4

FUTURE $PM_{2.5}$ EMISSIONS FROM METAL PRODUCTION TO MEET RENEWABLE ENERGY DEMAND[3]

4.1 Introduction

Anthropogenic emissions of greenhouse gases (GHGs) from fossil fuel combustion are the largest drivers of anthropogenic climate change (Masson-Delmotte et al., 2021). Projections of future global warming due to ongoing human activities suggest a temperature increase of 2-6 ºC compared to pre-industrial levels (Masson-Delmotte et al., 2021). To limit this temperature increase, many countries have committed to reducing their greenhouse gas emissions by shifting their energy sources to renewable energy such as solar and wind ("The Paris Agreement, UNFCCC, 2016").

More than 20 metals, including conventional and rare-earth, are required in the production of solar photovoltaic panels (PVs), wind turbines, and electric vehicles (EVs) (Giurco et al., 2019b; Watari et al., 2019b). The extraction and processing of these metals are emission-intensive activities causing health and ecosystem damage due to local and transboundary air pollution (Csavina et al., 2011; Ghose & Majee, 2001; Kavouras et al., 2001b). On a capacity basis (kg metal required per GW installed), the major renewable energy technologies require more than two orders of magnitude more metals than fossil fuel technologies (Valero et al., 2018; Watari et al., 2019b). The metal demand to make the major renewable energy technologies might reach around 5-20 times the present-day production levels in 2050 (e.g. Giurco et al., 2019).

[3]This work is published as Rathod, S. D., Bond, T. C., Klimont, Z., Pierce, J. R., Mahowald, N., Roy, C., ... & Rafaj, P. (2022). Future $PM_{2.5}$ emissions from metal production to meet renewable energy demand. *Environmental Research Letters*, *17*(4), 044043.

Mining and smelting are two major processes needed to extract and refine metals. Both these processes are emission-intensive for air contaminants such as particulate matter and SO_2 (Dudka & Adriano, 1997). Mining emissions occur during digging and extraction in open-pit mines, loading and unloading of trucks, storage and handling, and some initial ore refinement at source (cutting or crushing, wetting, etc) (Ghose & Majee, 2001; Huertas et al., 2012). Smelting emissions occur during high-temperature melting of metals to reduce impurities (generally in a blast furnace) and some secondary melting with high-grade oxygen to reach desired quality (generally in a basic oxygen furnace or in the presence of some electrolytes) (US EPA, 2016). In terms of primary impacts, mining and smelting contribute to more than 10% of ambient $PM_{2.5}$ concentrations in industrial cities such as Santiago in Chile and Panzhihua in China (Jorquera & Barraza, 2012b; Xu et al., 2021). Metal smelting is also a cause of heavy-metal pollution, such as mercury and nickel, in many places (Tian et al., 2012; Wu et al., 2012). There has been no estimation of future impacts on air quality from the processes to supply these materials in high renewable energy demand climate mitigation scenarios.

Only a few countries have economically feasible reserves and resources of many of these metals, and hence these countries control the metal supply (e.g. Giurco et al., 2019). For example, the Bolivia-Argentina-Chile triangle has over 50% of known reserves of the lithium needed for batteries (Seefeldt, 2020). Along with supplying the metals, these regions also bear the environmental impacts of mining and smelting (Kaunda, 2020). The dependence on solar and wind for rapid decarbonization and the material intensity of these technologies and the subsequent environmental impacts create a complex problem: global decarbonization might create local pollution impacts (Lèbre et al., 2020; Mwaanga et al., 2019). Because of growing concerns around critical metal supply, countries might focus inwards for meeting the metal demand, either by

increasing local extraction or acquiring raw ores from elsewhere (Vekasi, 2021). The changing regionality of metal extraction and processing could lead to changes in where impacts might occur relative to demand (e.g. increased exploration in the Round Top Mountain, USA, Pingitore, 2019).

This work aims at estimating the primary $PM_{2.5}$ emissions from mining and smelting of metals obtained specifically for making three technologies required to expand renewable energy: solar PV, wind turbines, and EVs. Many studies have estimated how trade redistributes emissions among countries for conventional goods and services (Lin et al., 2014; Wu et al., 2021; Zhang et al., 2017). This work augments this body of literature, focusing on the capital equipment required to deploy renewable energy. We analyze the effect of metal production regionality on distributions of emissions relative to demand and compare the effects of decarbonization rate and emission abatement on both emission totals and distributions. We also compare the projections with a highly idealized case in which each country produces metal to meet its own demands for renewable capacity. This extreme self-producing case is used mainly to contrast with emission distributions caused by natural trade.

4.2 Methods

We estimate the atmospheric emissions of primary $PM_{2.5}$ (particulate matter with diameter smaller than 2.5μm) by multiplying activity and emission factors that consider the extent of mitigation technology applied at a specific location/region (Bond et al., 2004; Klimont et al., 2017). Activity is the driver that causes emissions, such as energy or amount of metal mined, e.g. kWh energy generated, and emission factor is the emission intensity of the production process, e.g. g $PM_{2.5}$ / kWh. We use Equations C.1, C.2, and C.3 (within Text C.1) to derive metal demand projections, map the metal demand to relevant GAINS (Greenhouse gas - Air pollution

INteractions and Synergies, Klimont et al., 2017) process sectors, and estimate emissions from each GAINS sector in different years, respectively. This paper illustrates the distribution of environmental impact using $PM_{2.5}$. A complete analysis of air pollution impacts would include SO_2, NO_x, volatile organic compounds, and organic precursors, among others. However, NOx and VOCs are less relevant for the sectors covered in this study in terms of $PM_{2.5}$ formation, therefore we focus on implications for primary $PM_{2.5}$. In particular, SO_2 would increase the atmospheric concentration of particulate matter, but an atmospheric model is required to estimate the yield of $PM_{2.5}$ from SO_2. A simplified modeling experiment comparing magnitudes of SO_2 emission among regions under different scenarios is not reported here but gave similar findings on the regional distribution of emission and the effect of abatement. The analysis is performed at the global scale for the years 2020 to 2050, with a 5-year resolution. We analyze eight policies of decarbonization rates, abatement, and production regionality for their effect on emissions and distributions, as shown in Table 4.1 and described below. The penetration of renewable energy is projected to reduce the dependency on, and hence emissions, from fossil fuel combustion sources. We compare the metal production-related $PM_{2.5}$ emissions to anthropogenic combustion $PM_{2.5}$ emissions to evaluate its relative regional contribution. We use the anthropogenic combustion emissions from the GAINS model in the corresponding energy and abatement cases as described below.

Table 4.1. Scenarios explored in this study. Two cases of each policy are explored, for a total of eight scenarios

	Cases							
Scenarios	**1**	**2**	**3**	**4**	**5**	**6**	**7**	**8**
Energy Policy	→	→	→	→	↘	↘	↘	↘
Air Pollution Policy	→	→	↘	↘	→	→	↘	↘
Production Regionality	֍	●	֍	●	֍	●	֍	●

Energy Policy		*Air Pollution Policy*		*Production Regionality*	
Current Energy Policy	→	Current Abatement Legislation	→	Global Market	֍

Rapid Decarbonization ↘ Stringent Mitigation ↘ Local Production ●

Activity: Renewable additions (GW/yr) and fleet projections (vehicles/yr) are based on two scenarios from World Energy Outlook 2020 (International Energy Agency IEA, 2020). The "Current Energy Policies" scenario relies on projections in the IEA Stated Policies Scenario, which predicts energy mix based on current or committed policies. Anthropogenic GHG emissions in scenarios used in this study correspond approximately to a set of scenarios used in the climate modeling community within the IPCC sixth Assessment Report, these so-called Shared Socioeconomic Pathways (SSPs) span across different macroeconomic, populations, and climate policy assumptions (Riahi et al., 2017). The Current Energy Policy scenario is similar to the SSP2-4.5 (Fricko et al., 2017). The Rapid Decarbonization scenario corresponds to IEA's Sustainable Development Scenario. It assumes a much faster decarbonization rate than the Stated Policies Scenario and has anthropogenic GHG emissions similar to the SSP1-2.6 (van Vuuren et al., 2017). The comparison of outcomes between the two scenarios demonstrates how metal demand, total anthropogenic emissions, total air pollution, and regional distributions of metal production may respond to rapid decarbonization. Metal composition and intensities from Watari et al., (2019) are used for all three technologies (Table C.1) for the 2020-2050 period. We assume all solar PV to be crystalline silica PV and all wind turbines to be onshore based on their projected higher penetration in SSP scenarios (https://tntcat.iiasa.ac.at/SspDb), and all EVs to be passenger EVs based on their projected number of sales compared to other forms of EVs, the relatively smaller difference in material requirement between vehicle types, and the uncertainty in future material composition and intensities (Table C.2, and Wolfram et al., 2021). For the mining sector, the activity in units of kg of ore is estimated as the sum of the steel, aluminum, and all non-ferrous metals multiplied by three (based on 2019 global steel-to-iron-ore and aluminum-to-bauxite

production ratios) since the metal-to-ore data were scarce for most metals, and because many important critical metals are simply obtained as by-products during conventional metal production. IEA activity data are downscaled from the original 26 macro-regions to 180 emission/source GAINS regions using a downscaling routine described in Text C.2 (Rafaj et al., 2018).

Emission Factors: Region-specific uncontrolled $PM_{2.5}$ emission factors for both combustion and non-combustion activities are used from the GAINS model for metal mining and smelting sectors. Emission factors for the mining sector represent the emissions during digging and extraction. Fugitive emissions from mines and trucking-related operations are not considered due to a lack of data. Smelting emission factors represent the particulate emissions during high-temperature melting of ores in blast furnaces for iron and aluminum. For the non-ferrous metals sector, we use the emission factor for copper as it is the largest non-ferrous metal considered in this work. Two GAINS abatement pathways, "Current Abatement Legislation" in which abatement policies are based on current and stated policies, and "Stringent Mitigation" in which the best control technologies are employed to the maximum extent without structurally changing the energy mix, are analyzed (Rafaj et al., 2018). Most results presented here will be with Current Abatement Legislation, while Stringent Mitigation is used to assess the effect of stricter abatement policies on emissions. Under the Stringent Mitigation case, different regions adopt the best possible abatement measures starting from 2020 and peaking by 2040. Factors such as the present stock of technologies and the technical feasibility of control application govern the abatement rate and penetration in different regions in the Stringent Mitigation case (Rafaj et al., 2018).

Regionality of Activity: To evaluate the effect of the location of production on emissions, we explore two cases, Global Market and Local Production. Under the Global Market scenario, the amount of renewables-related metal activity occurring in a region is proportional to the total metal

activity in the IEA projections (IEA, 2020). IEA predicts the magnitude and regionality of metal production based on policies, infrastructure change, and economic projections. However, in the "Global Market" regionality, only a few countries produce most minerals. This concentrates environmental impacts in the producing countries and creates a concentrated supply chain that is vulnerable to trade disruptions (Nassar et al., 2020). We simulate an idealized "Local Production" case in which countries mine and smelt their own metals for renewable energy devices. This scenario assumes that all countries have sufficient mineral resources and technologies to mine and smelt metal ores and metals. While this is an idealized scenario, countries may move in this direction to ensure mineral (American Mineral Security Act, 2020; European Commission, 2020), and thus it could greatly affect where and how production happens. We use a distribution index, similar to the Gini index (Gastwirth, 1972; Lorenz, 1905), to quantitatively compare regional distributions of emissions to metal demand in different decarbonization, abatement, and production scenarios. The distribution index can be derived by plotting in Cartesian coordinates where the x-axis is the cumulative normalized metal demand from the lowest to the highest and the y-axis is the cumulative normalized emissions corresponding to the demand region. Then, the distribution index is calculated as the ratio of the area between the perfect equality line and the curve divided by the total area under the perfect equality line. A distribution index value closer to zero indicates emissions occur in the demand region, and a value of one indicates most emissions are concentrated in fewer regions than demand.

4.3 Results and Discussion

4.3.1 Metal demand

Under the Current Energy Policies scenario, the finished total metal demand is 195 million tons (Mt) /yr in 2020, peaking at 270 Mt/yr in the years 2040-2045 and ending at 250 Mt/yr in

2050. Under the Rapid Decarbonization scenario, the total finished metal demand peaks at 480 Mt/yr in the year 2040 and then declines to 325 Mt/yr in 2050 (Figure C.1, Table C.3). Among the renewable technologies, demand is dominated (around 70%) by solar in all years in both the scenarios (Figure C.1) due to its high metal intensity and the overall role in capacity addition. EVs pose around 20% of renewables-related metal demand in Current Energy Policies and 30% in Rapid Decarbonization. Total metal demand for wind turbines is the least, at around 1-4% in both scenarios. Iron and steel account for more than 90% of the total metal demand due to their higher intensity in all three technologies (Table C.3). The metal demand by renewables represents about 8-17% of all-use demand for steel, 10-28% for non-ferrous metals, and 4-12% for aluminum (Table C.3).

Low- and middle-income countries represent most of the metal demand due to their projected renewable energy addition (IEA, 2020). India and China account for 20-45% of the metal demand (Figure C.2- C.4) via solar PVs, wind turbines, and EVs. High-income regions represent a major demand in the first half of the 2020-2050 period but then have slower growth, except for EVs for which growth is higher in the second half of the period (Figure C.2- C.4). The relative metal demand is much higher in Asian, African, and Latin American countries in the Rapid Decarbonization than in Current Energy Policies for all the three technologies, and Rapid Decarbonization, in general, has more regional diversity in demand than Current Energy Policies.

4.3.2 Emissions

Figure 4.1a and 4.1b show the regional $PM_{2.5}$ emissions from mining and smelting to meet the metal demand of global renewables in the two pathways with the Current Abatement Legislation measures. Emission values in the Rapid Decarbonization values are almost twice those of Current Energy Policies in many years for the Current Abatement Legislation case, similar to metal

demand. India and China dominate emissions in both scenarios. USA, Russia, Eastern Europe, and rest-of-Asia account for about 30% of emissions. Rest-of-Asia, Africa, and South America have a similar contribution to emission in the two scenarios, at about 15%. Stronger abatement in future years is projected to cause about 90% emission reduction in both the pathways (Figure C.5). Emissions peak at the same time as capacity addition in both the scenarios with Current Abatement Legislation. With Stringent Mitigation, emissions are projected to peak much earlier than with Current Abatement Legislation (Figure C.5), and with a much lower magnitude (Klimont et al., 2017; Rafaj et al., 2018). Emissions remain at a constant minimum level after 2035 due to the offsetting effect of capacity addition and emission control (Figure C.5).

Technology-wise, Solar photovoltaics and EVs cause most of the emissions in Current Energy Policies and Rapid Decarbonization with both Current Abatement Legislation and Stringent Mitigation (Figure C.6), similar to their fractions in the metal demand. Process-wise, smelting represents about 95% of total primary $PM_{2.5}$ emissions and mining the rest (Figure C.7). Steel, non-ferrous metals (NFMEs), and aluminum smelting represents about 80%, 10%, and 5% of the total with similar contributions in Current Abatement Legislation and Stringent Mitigation cases. The relative contribution of mining is projected to increase even with Stringent Mitigation as controls are applied to point sources more than area sources (Figure C.7).

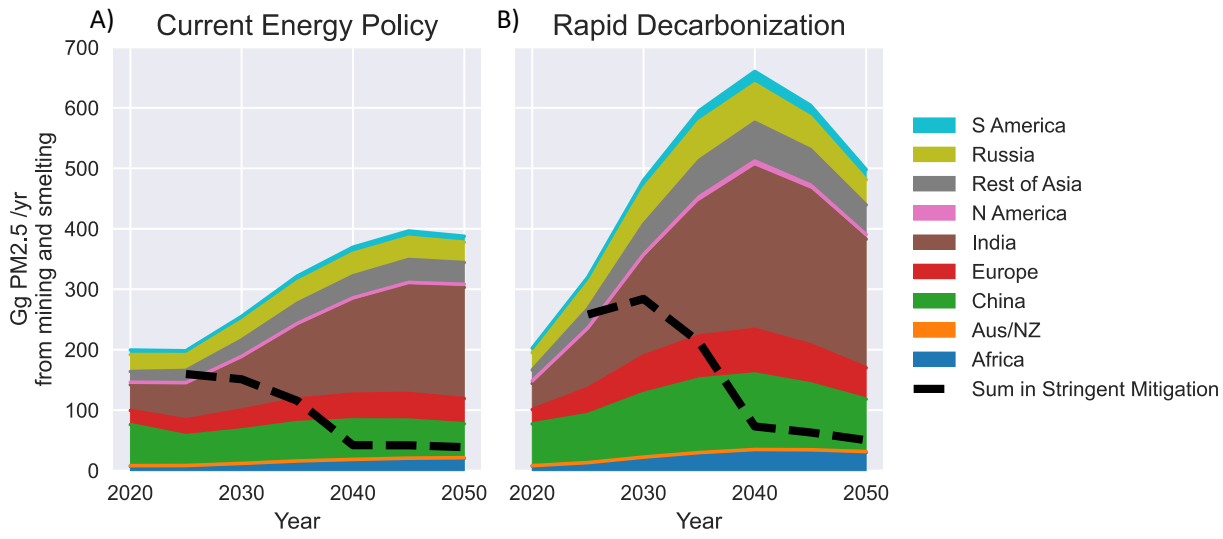

Figure 4.1. $PM_{2.5}$ emissions from metal mining and smelting toward making renewable energy devices in (A)Current Energy Policies and (B) Rapid Decarbonization scenarios by region with Current Abatement Legislation policies. Dashed lines show the total emissions for Stringent Mitigation cases. Note: no data available for Stringent Mitigation for the year 2020.

Figure 4.2 shows the anthropogenic combustion and metal-related primary $PM_{2.5}$ emissions in the two scenarios and the contribution of mining and smelting to anthropogenic combustion emissions. Primary $PM_{2.5}$ emissions from mining and smelting to meet global renewable energy demand are projected to reach 5-15% of total anthropogenic combustion $PM_{2.5}$ emissions in India (Figures 4.2b and 4.2f) and China (Figure 4.2a and 4.2e) in both pathways with Current Abatement Legislation policies. North America and European Union (Figure 4.2c and 4.2g) are projected to have a similar rate of emission reduction as India and China but the contribution by mining and smelting is much smaller, due to the lower expected future production and cleaner smelter plants. The $PM_{2.5}$ emission contribution due to mining and smelting is amplified in the Rapid Decarbonization scenario due to more demand of metals and a quicker reduction of fossil fuel emissions. However, even with higher metal-related emissions, the total anthropogenic emissions are much lower in the Rapid Decarbonization scenario compared to Current Energy Policies.

The global shift from fossil to renewable energy is estimated to create a high burden of air pollution due to metal mining and smelting in many regions (Figures C.8, C.9, and C.10). Introducing available mitigation techniques, however, could reduce the burden by rapidly reducing emissions in most regions. After 2035, when penetration of abatement measures increases in the Stringent Mitigation case (Klimont et al., 2017, Rafaj et al., 2018), mining and smelting-related emissions decrease rapidly along with other combustion emissions. The contribution of mining and smelting emissions falls from over 15% in India in the Current Abatement Legislation case to less than 5% after 2035. For regions such as Eastern Europe where mining and smelting emissions are projected to be dominant, the contribution of these emissions drops by half between Projected and Stringent Mitigation cases, demonstrating the role of policies in stimulating the introduction of efficient emission mitigation technologies.

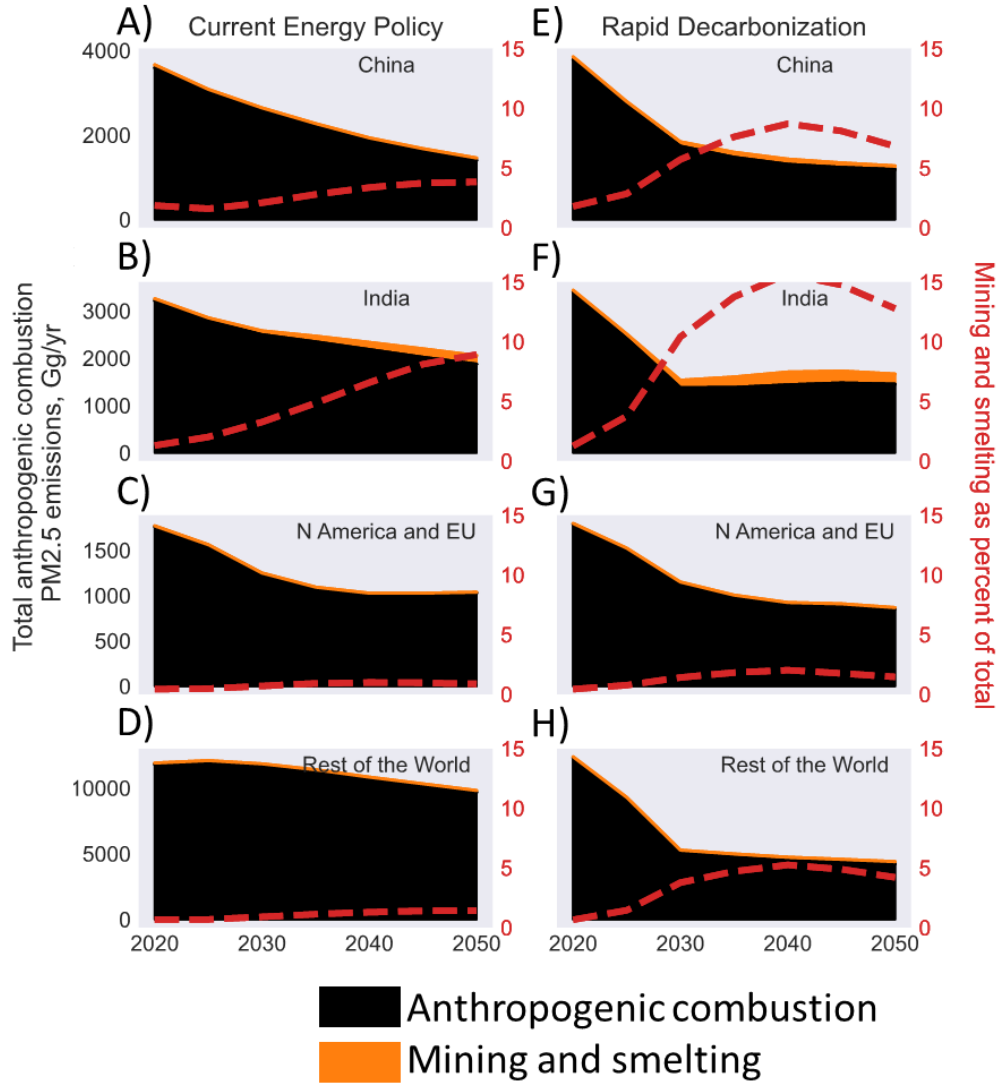

Figure 4.2. Absolute primary $PM_{2.5}$ emissions from anthropogenic combustion (black) and mining and smelting for metals for renewable technologies (orange) are shown for the Current Energy Policies (A-D) and Rapid Decarbonization scenarios (E-H) for India, China, North America, and European Union, and Rest of the World. $PM_{2.5}$ emissions by mining and smelting to meet metal demand for renewables, shown as percent of the total (mining and smelting and fossil fuel combustion) (red line, right axis).

4.3.3 Regional distributions of metal demand, production, and emissions

Figure 4.3a and 4.3c show regional contributions to metal demand, production, and smelting-related $PM_{2.5}$ emissions in the two abatement scenarios for the Current Energy Policies and Rapid Decarbonization pathways for the year 2050, based on Global Market regionality. Figure 4.3c and

4.3d show the same information as 4.3a and 4.3b, but for the Local Production case where all countries mine and smelt to meet their own renewable-driven metal demand. Figure 4.4 shows the time series of the distribution index for the cases studied in this work (data in Table C.4). A value of zero indicates the same distribution between emission and demand, and higher values indicate that emission is relatively more concentrated than demand. Below we discuss the effect of the rate of decarbonization, abatement, and production regionality on emissions and the distribution index.

Rate of decarbonization: With Current Abatement Legislation and Global Market regionality, the Current Energy Policies pathway has a lower distribution index compared to Rapid Decarbonization in the 2020-2050 period (Figure 4.4), indicating a more evenly distributed regionality of emissions compared to demand. In Rapid Decarbonization, with Current Abatement Legislation and Global Market, more regions add renewable capacity, but the number of regions producing metals remains the same in the two pathways, so its overall distribution index becomes higher, particularly in later years.

Abatement Policy: Current Abatement Legislation cases have a much higher distribution index in future years compared to Stringent Mitigation cases for both the decarbonization pathways under the Global Market regionality (Figure 4.4). Stringent Mitigation in this case leads to a lower distribution index because in this case abatement also occurs in regions with high-emitting technology. Most emissions occur in India if Current Abatement Legislations are considered, and in China, if Stringent Mitigations are considered in the scenarios (Figure 4.3). This difference between India and China in the two scenarios is due to the assumed higher emission factor and lower abatement penetration in China compared to India for the smelting sector under Stringent Mitigation measures (Rafaj et al., 2018).

Production regionality: Most future demand occurs in low- and middle-income regions. In the hypothetical Local Production case, the production also occurs in regions where emission control policies are not stringent (Figures 4.3c and 4.3d). Thus, metal-related emissions are higher in the Local Production cases than in Global Market for both, Current Energy Policies and Rapid Decarbonization (Figure 4.4). Local Production cases have a lower distribution index than Global Market under stated abatement policies (Figure 4.4). This is because the regional distribution of emissions is roughly the same as demand in absence of strong controls. However, even when most regions reduce their emissions in the Stringent Mitigation case, the highest emission occurs in regions that lag in abatement measures, skewing the regional distribution of emissions compared to demand and leading to a higher distribution index in the Local Production case with Stringent Mitigation.

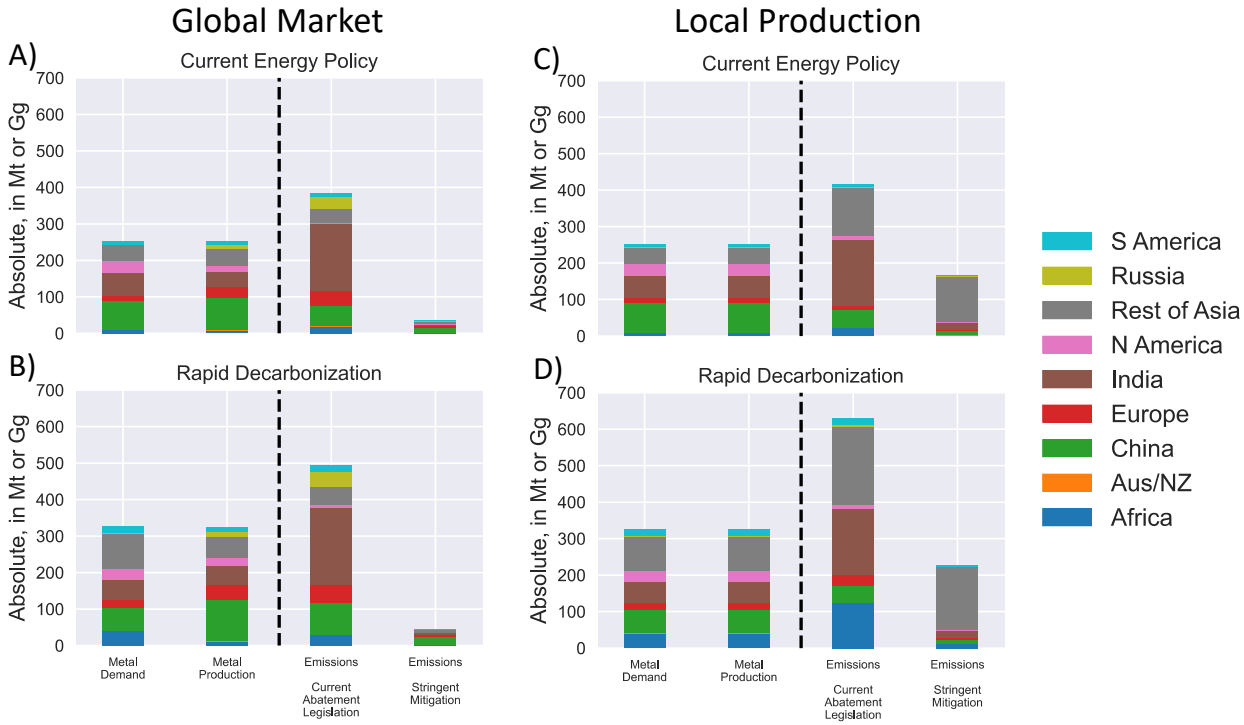

Figure 4.3. Absolute total metal demand (Mt), production (Mt), and related emissions (Gg) for Current Energy Policies (A and C) and Rapid Decarbonization (B and D) scenarios with Current Abatement Legislation policies with Global Market regionality (A and B), and with Local Production regionality (C and D). Shown only for the year 2050.

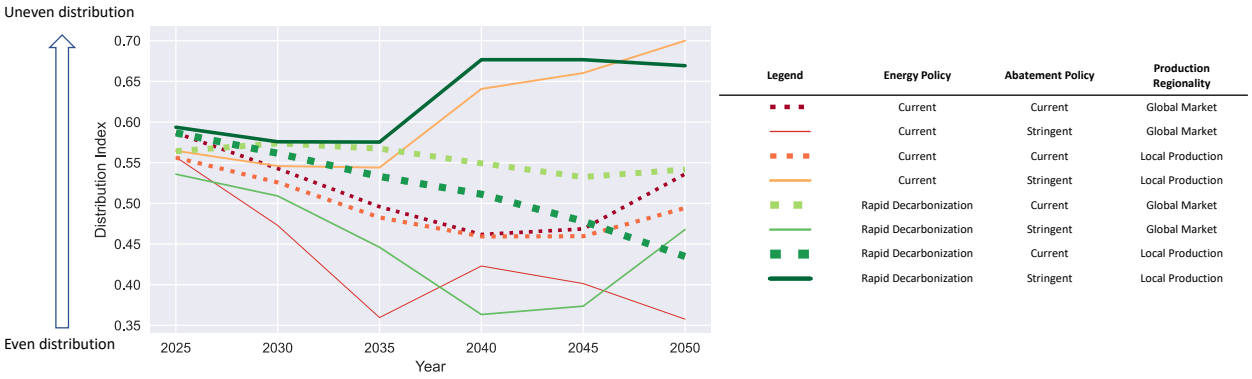

Figure 4.4. Trends in distribution index for regional distributions of emissions relative to demand, for all cases. Dashed lines show Current Abatement Legislation cases. Line widths and dash widths are linearly proportional to 2025-2050 total emissions from mining and smelting. The distribution index shows how regionally emissions are distributed compared to where demand occurs. A value closer to zero indicates emissions are collocated with demand. Values closer to one indicate most emissions are comparatively concentrated in fewer regions compared to demand. 'Current' under Energy Policy and Abatement Policy refers to 'Current Energy Policies' and 'Current Abatement Legislation', respectively.

Timeseries of the Gini-like distribution plots are shown in Figures C.11-C.16 for activity and emissions at various disaggregation. Most activity-related inequalities in activity might happen in the mining sector, followed by non-ferrous metals. Aluminum and steel might have the least inequalities for all the three technologies in future years for activity (Figures C.11-C.13). Activity-related inequality might increase in future as more regions demand renewable technologies in both the scenarios. The level of abatement also affects the metal-related inequality. As stronger abatement in Stringent Mitigation is realized after 2030, there is a reduction of emissions-related inequalities in both the scenarios (Figure C.14-C.16), indicating that stronger abatement does not only reduce overall emissions but also overall inequality regardless of the activity pathway. This

is intuitive, since the regionality of production and demand might not change, reducing emissions anywhere they are occurring might aid in reduce the overall inequalities.

4.3.4 Implications and Caveats

The global metal-related $PM_{2.5}$ emissions of 0.3-0.6 Tg/yr to make renewable energy devices is a small fraction of total anthropogenic emissions, and it is also small compared to the expected decrease in combustion emissions. Thus, this emission increase is not expected to attract global attention, but atmospheric pollution in producing areas needs to be evaluated as part of the life cycle so that the global move to renewable energy does not unfairly burden a few regions.

The highly idealized Local Production scenario avoids the effective export of emissions caused by the metal trade. However, the Local Production scenario would increase metal production and related pollution in these same areas where abatement measures are weak. Both global moves toward renewable energy and individual nations' attention to mineral security may increase demand for metals. Attention to emission abatement measures in the metal production sector, especially in regions with currently low abatement measures, is needed before these shifts occur; otherwise, nations may be forced into increasing the security of energy or minerals at the expense of their inhabitants' health.

Several assumptions in this study affect the magnitude and regionality of metal demand, production, and emissions and are summarized here. We use present-day metal intensity values for 2020-2050, although compact devices or devices that use different materials (e.g. Das et al., 2019) could affect future metal demand and activity location. IEA (2021) predicts that increased material efficiency could reduce cobalt demand in EV batteries by half but only modestly affect lithium demand. Advanced materials in solar panels have generally lower material requirements than the crystalline silica panels modeled in this study. As current mines run out of feasible and

high-grade ores, economies might either shift production to newer, feasible mines and create new smelter plants near them, or produce more ore to get the same metal amount (e.g. Mohr et al., 2015). The rate of ore quality decline could range from 0.1 to 5% per year (Calvo et al., 2016; Northey et al., 2014; Watari et al., 2019b) and hence could affect the amount of mining and the location of new mines. Materials for transmission and utility energy storage are not considered here and might represent more than 30% of total renewables-related metal demand (IEA, 2021). Finally, local production costs are affected by the accessibility of metal resources in each region, and the response of demand to this change in cost has not been modeled here.

Even if the assumptions listed above were further refined, the major lessons from this analysis are not expected to change. That is, rapid decarbonization will lead to a large overall decrease in $PM_{2.5}$ emissions, but it can increase inequity by placing the atmospheric burden in producing regions (e.g. Mohr et al., 2015), and those inequities cannot be solved by self-producing without attention to emission abatement.

4.4 Summary and Conclusion

A shift from fossil fuel to renewable energy is crucial in achieving climate targets. However, the higher material intensity of most renewable energy devices compared to fossil fuel technologies, and the emission-intensive methods to obtain those materials cause environmental impacts. This work quantifies the $PM_{2.5}$ emissions from mining and smelting due to the metal requirement for achieving the renewable energy goals in two IEA scenarios implemented in the GAINS model: Current Energy Policies and Rapid Decarbonization. Global $PM_{2.5}$ emissions from mining and smelting are projected to reach about 15% of total anthropogenic combustion-related $PM_{2.5}$ emissions in many regions in the Current Energy Policies scenario, and about 30% in the

Rapid Decarbonization scenario between 2020 and 2050. Only a few regions such as India and China might bear the burden of metal-related emissions due to the projected metal exploration and production in those regions and their relatively higher-emitting smelter plants. Introduction of legislation that relies on proven technology to reduce air pollutant emissions, anticipating global energy transition to renewables, would avoid increased pollution Rapid Decarbonization scenario is estimated to lead to overall lower anthropogenic emissions even if the mining and smelting emissions increase but could also lead to an increased unevenness of the distribution of metal-related emissions relative to demand, as compared to Current Energy Policies. Stronger application of emission control policies could reduce metal-related emissions by 90% and also reduce the unevenness of distribution of emissions relative to demand. Moving metals production to an expanded set of countries may cause excess $PM_{2.5}$ exposure. Policies that can provide access to rare-earth metals for developing economies may thus be important in achieving the full climate benefits of renewable energy technologies.

4.5 Data Availability

The activity and emission data for steel, aluminum, and non-ferrous, non-aluminum metals required for making solar PVs, wind turbines, and electric vehicles are available from GAINS v4 (https://gains.iiasa.ac.at/gains4/GOD/index.login).

RATHOD_WEO2020_<SCENARIONAME>_<ABATEMENT>_<TECHNAME>_ACTUA

Where SCENARIONAME = “STEPS” corresponding to Current Energy Policies or “SDS” corresponding to Rapid Decarbonization.

ABATEMENT = “CLE” corresponding to Current Abatement Legislation or “MFR” corresponding to Stringent Mitigation

TECHNAME = ‘SL’, ‘WN’, or ‘EV’, corresponding to Solar PV, wind turbines, and electric vehicles, respectively.

CHAPTER 5

SUMMARY AND FUTURE WORK

This dissertation presents an assessment of the role of iron and other metals in the atmospheric, oceanic, and energy systems. I examined if the Earth system impacts of iron, direct radiative forcing (DRF) and net primary productivity (NPP), could become important even with known uncertainties. Moreover, since these impacts are directly linked to emissions, I estimated the bounds of anthropogenic iron emission estimates using models and observations. And finally, I estimated the future atmospheric emissions of particulate matter due to metal mining and smelting since metals form an integral part of the global energy transition from fossil fuels to renewable energy. This final chapter summarizes the key findings of this dissertation.

5.1 Summary

Chapter 2: Direct radiative forcing and net primary productivity by anthropogenic iron emissions in the 1850-to-2010 period.

I estimated the atmospheric radiative and oceanic biogeochemical effects of anthropogenic-combustion-iron emission from the power, industrial, residential, and transportation sectors with a focus on mineralogical characteristics of iron. The key findings of this chapter are:

1. ***Global direct radiative forcing by anthropogenic iron is 5% of the sum of other anthropogenic aerosols.*** Anthropogenic combustion-iron emissions cause about +0.02 W/m^2 global mean 1850-2010 top-of-atmosphere all-sky DRF, with strongly absorbing iron oxides causing +0.03 W/m^2 and weakly scattering clays causing -0.01 W/m^2. The net forcing of +0.02 W/m^2 is about around 5% of the magnitude of net

anthropogenic aerosol direct radiative forcing although in the opposite sign, and 0.7% of all anthropogenic forcing including gases in the 1850-2010 period (Masson-Delmotte et al., 2021).

2. ***Global Net Primary Productivity effects by anthropogenic iron is 0.5% compared to total ocean NPP.*** The deposited anthropogenic soluble iron sustains 0.3 (0.2-11) Pg C/yr of present-day oceanic net primary production. Present-day atmospheric CO_2 concentrations would have been 0.3 (0.2-13) ppmv higher without the anthropogenic soluble iron deposition in the last 150 years, indicating an avoided CO_2 forcing of -0.002 to -0.16 W/m^2. The anthropogenic NPP of 0.3 Pg C/yr is around 0.5% of the total ocean NPP of 40-60 Pg C/yr (Behrenfeld & Falkowski, 1997; Buitenhuis et al., 2013; DeVries & Weber, 2017) and 1850-2010 avoided CO_2 forcing values of 0.002-0.16 W/m^2 due to anthropogenic soluble iron deposition are between 0.08-7% of total anthropogenic CO_2 forcing in this period (Masson-Delmotte et al., 2021).
3. ***Smelting and oil combustion are the largest emitters of iron oxides and sulfates, and hence they also act as the largest controls of anthropogenic DRF and NPP.*** Iron oxides (magnetite and hematite) exert a net warming effect on the Earth system since they have high radiation absorption properties (Moteki et al., 2017) and very low contribution to soluble iron deposition (Journet et al., 2008; Rathod et al., 2020). Sulfates, on the other hand, exert a cooling effect due to their high soluble iron fraction and thus more promotion of phytoplankton growth leading to more carbon fixation (Journet et al., 2008). Since, respectively.
4. ***The anthropogenic role could be crucial for oceans that are stratifying due to climate warming.*** Anthropogenic soluble iron deposition sustains about 10% of the

total ocean NPP in the high-latitude North Pacific Ocean, with an upper bound of 40%. Anthropogenic soluble iron supply to the North Pacific Ocean hence could become crucial as this basin is predicted to undergo increased stratification in the future due to climate change.

Chapter 3: Evaluating anthropogenic iron emissions using models and observations.

I evaluated various elements of a present-day anthropogenic combustion-iron emission inventory using observations and models. I used all the available methods and observations to evaluate only the emissions part including the anthropogenic sub-sectors such as coal combustion and smelting. The key findings of this chapter are:

1. ***Anthropogenic emissions from only three regions matter for oceanic iron-limited regions.*** The anthropogenic soluble iron supply from three regions, East Asia and North America, and western South America overlaps with regions where the oceanic phytoplankton growth is iron-limited, and hence anthropogenic iron emissions from these regions are important to constrain.
2. ***As few as 40 sites can be used to evaluate the averaged model-observation concentration bias in a region***. Considering more sites for comparison did not improve our confidence in the average model bias.
3. ***Anthropogenic fine iron emissions from North America are underestimated by a factor of 2, and overestimated from Europe by a factor of 1.1, with a factor of 2 uncertainty.*** The model matches observations well for anthropogenic fine iron emissions in Asia (factor of 1 with a factor of 1.5 uncertainty), but that region has a low number of observations.

4. ***The most important anthropogenic soluble iron source is underestimated by a factor of 2 in the current estimates.*** The receptor modeling estimates using Positive Matrix Factorization suggest that heavy-fuel-oil-related iron emissions are underestimated by a factor of 2, and the spatial distribution of modeled and observed Oil-Fe shows more underestimation (by a factor of 3) over coastal areas (dominated by shipping emissions) than many inland areas (dominated by industrial boilers). With these bounds in the heavy fuel oil combustion from shipping and industrial boilers, the anthropogenic soluble iron supply to the North Pacific and North Atlantic could be a factor of 3 higher than the current estimates, and range at 25-75% and 20-60% of the total atmospheric soluble iron, respectively.
5. ***Smelting-related iron oxide emissions are overestimated by a factor of 1.5 from East Asia.***

Chapter 4: Future emissions from metal mining and smelting to meet projected renewable energy demand.

In this chapter, I estimated the $PM_{2.5}$ emissions from metal mining and smelting to meet the projected demand of solar photovoltaics, wind turbines, and electric vehicles in the 2020-2050 period. The key findings of this chapter are:

1. ***$PM_{2.5}$ emissions due to mining and smelting might remain low globally but can get higher in certain regions.*** The global metal-related $PM_{2.5}$ emissions of 0.3-0.6 Tg/yr in the peak year 2035 to make renewable energy devices are less than 5% of present-day total anthropogenic emissions. However, $PM_{2.5}$ emissions from mining and smelting are projected to reach about 15% of total anthropogenic combustion-related

$PM_{2.5}$ emissions in many regions such as India and China in the Business-As-Usual scenario, and about 30% in the Rapid Decarbonization scenario between 2020 and 2050.

2. ***The Rapid Decarbonization scenario has lower global total $PM_{2.5}$ emissions even when accounting for an increase in mining and smelting.*** The $PM_{2.5}$ contribution due to mining and smelting is amplified in the Rapid Decarbonization scenario compared to Business-As-Usual due to more demand for renewable energy and hence metals. However, even with higher metal-related contribution, the global total (from fossil fuel combustion and metal production processes) anthropogenic emissions are estimated to be much lower in the Rapid Decarbonization scenario compared to Business-As-Usual due to a more rapid decline in fossil fuel emissions.
3. ***The inequality in emissions due to the geographical resource and demand distribution is projected to be higher in the Rapid Decarbonization scenario compared to a Business-As-Usual case.*** More regions add renewable capacity in the Rapid Decarbonization scenario compared to the Business-As-Usual case, but the number of regions producing metals remains the same in the two pathways. Hence, it puts more stress on the metal-producing regions and thus increases the unevenness in impact distribution.
4. ***Emission abatement has the potential to reduce 90% of emissions.*** In the Stringent Mitigation scenario, emission control methods are applied fully in most regions after 2035, thus leading to a 90% reduction in metal-related $PM_{2.5}$ emissions compared to the Business-As-Usual scenario. Countries like India and China might see the largest benefits due to the strictest abatement in their metal extraction and production sectors.

5. ***Policies that aim for mineral security might increase emissions in many regions.*** The geopolitics of critical minerals has motivated many countries such as the USA to push for mineral security. I ran a hypothetical scenario in which all countries push for mineral security and thus mine and smelt their metals for their renewable energy program, even if they might not have sufficient metal reserves or resources. I found that this hypothetical scenario could lead to more global emissions compared to the one in which metal production occurs "normally" in the future in regions with proper resources. The mineral security scenario has more emissions because countries that are not prepared with low-emitting combustion and metal-production technologies and abatement tools are also now involved in metal production.

5.2 Recommendations for future work

While it is important to understand the impacts of human activities on the Earth, it is equally important to identify the questions that could aid in a better systems understanding. Below I describe some of those questions in the context of this dissertation. These questions are aimed at inviting broader discussion about establishing the importance of a research topic and asking the 'right' questions in the energy transition discussions.

1. The uncertainty in the global anthropogenic iron impacts on the Earth system does not need to be narrowed and the focus should be on understanding its local impacts.

Instead of the uncertainty in the global anthropogenic iron impacts on the atmospheric radiative and oceanic biological effects, we need to focus on the local impacts for the following reasons:

1. The central values and the uncertainty in the atmospheric radiative and oceanic biological impacts of anthropogenic iron emissions are globally less than 5% of the system total or the total anthropogenic impacts (Table 5.1). Both the impacts remained smaller compared to the system totals even after I included as many uncertainties as possible in the estimates. For NPP, however, the upper estimate of 11 Pg C/yr does become comparable to the total ocean NPP of 40-60 Pg C/yr, but all modeling studies show the anthropogenic iron NPP to be less than 1 Pg C/yr.

Table 5.1. The magnitude of anthropogenic and system totals for DRF and NPP. Values from Rathod et al. (2022. *Accepted*)

Effect	**Anthropogenic contribution (central-high)**	**Comparison with system total (central-high)**
DRF (1850-2010)	0.03-0.1 W/m^2	2.3-3.3 W/m^2
NPP (2010)	0.3-11 Pg C/yr	40-60 Pg C/yr

2. The known mechanisms and observations suggest the central value and the uncertainty might be smaller for both DRF and NPP than estimated in Chapter 2, thus further decreasing their estimate. For DRF, observations (Yoshida et al., 2020) suggest the current simulated mean of the concentrations of iron oxides is overestimated by a factor of 1.5 in the high-impact areas (see Sec. 3.3.2.5). For NPP, moving from a simplistic approach that I used for estimating the anthropogenic marine NPP to a complex, mechanistic ocean model might reduce the estimated oceanic response because of various system buffers such as luxury intake of iron that I did not consider (Okin et al., 2011 ; Hamilton et al., 2020).

3. Local impacts need to be studied to better understand the overall impacts of anthropogenic iron emissions. Though globally small, both the DRF and NPP impacts are locally higher or comparable to the system or anthropogenic totals. Yet, their local impacts are not well understood, particularly for direct public relevance. For example, anthropogenic soluble iron supply currently sustains 5-20% of the phytoplankton growth in many parts of the iron-limited North Pacific Ocean, which are important for fishery yield (Watson et al., 2004). Yet, only a small body of work exists on connecting the impacts of atmospheric iron deposition with the stimulated phytoplankton for impacts such as fishery yield. For DRF, anthropogenic iron oxides cause 0.5 W/m^2 of direct radiative forcing over many parts of East Asia, a value comparable to other anthropogenic species such as Black Carbon. Yet, the direct application of these values for public health and local climate is not well-studied. Thus, studies that aim at bridging the gap between the Earth system effects of emissions with their subsequent and real-world impacts on local-level public health and climate might aid in a better understanding of the overall impacts of anthropogenic emissions.

2. A holistic assessment encompassing various impacts and justice lenses is required to understand the total impacts of energy transition on human and ecosystem health.

This recommendation is related to Chapter 4 in which I estimated the global and regional $PM_{2.5}$ emissions due to metal mining and smelting in future energy scenarios.

1. Energy transition affects multiple environmental outcomes that are not presently represented. Many impacts such as water and soil pollution are lesser understood and could be important for human and ecosystem health. Studies have shown elevated levels of carcinogenic uranium and cobalt in blood and urine in populations near the cobalt mines in the Democratic Republic of Congo and chromium in populations near the chromium and copper mines in India

(Banza Lubaba Nkulu et al., 2018; Parveen et al., 2016; Vijayanand et al., 2008). These metals also end up in the agricultural soil and thus in the food system (Ma et al., 2015). Many of these impacts are difficult to estimate for present-day and for future activities but deserve attention due to their longer timescales of persistence in the water and food systems than in the atmosphere. While air pollution is an important aspect affecting human health, it is not yet possible to estimate the true cost of energy transition, considering all the factors.

2. The analyzed outcome of energy transition impacts depends on the justice aspect. I focused only on the country-by-country distributional justice aspect of energy transition via the metal and the air pollution lens. However, the same situation --- who emits, who gets --- could also be evaluated via multiple aspects of transitional justice, such as social, economic, opportunity, relational, and equality justices (Bainton et al., 2021; Hahnel, 2020; McCauley & Heffron, 2018; Moeng, 2019; Simangan & Gidley, 2019; Velicu, 2019). Assessing how global energy transition changes the inequalities and inequities across the world via various justice approaches thus would allow us to explore policy options that mitigate impacts while ensuring equitable outcomes.

3. The analyzed outcome of energy transition impact on equity and justice depends on the spatial scale. The disparity in impacts could be greater at an intra-country level than at the inter-country level based on the resource and income distribution within those countries. While countries like India and China might get the greatest air pollution impact of energy transition (Rathod et al., 2022), certain populations within these countries are actually the ones most at risk due to their proximity to the mines and smelter plants (Banza Lubaba Nkulu et al., 2018; Naz et al., 2016; Parveen et al., 2016; Vijayanand et al., 2008). Doing inter-country analysis ignores these intra-country aspects and thus the populations that might be the most vulnerable to impacts during

the global energy transition. Thus, the analysis of the equity and justice aspects of any policy various spatial scales might aid in identifying all the inequitable outcomes of energy transition.

REFERENCES

Adebiyi, A. A., Kok, J. F., Wang, Y., Ito, A., Ridley, D. A., Nabat, P., & Zhao, C. (2020). Dust Constraints from joint Observational-Modelling-experiMental analysis (DustCOMM): comparison with measurements and model simulations. *Atmospheric Chemistry and Physics*, *20*(2), 829–863. https://doi.org/10.5194/acp-20-829-2020

American Mineral Security Act. (2020). S.1317 - A bill to facilitate the availability, development, and environmentally responsible production of domestic resources to meet national material or critical mineral needs, and for other purposes. Retrieved from https://www.congress.gov/bill/116th-congress/senate-bill/1317/text

Bainton, N., Kemp, D., Lèbre, E., Owen, J. R., & Marston, G. (2021). The energy-extractives nexus and the just transition. *Sustainable Development*, *29*(4), 624–634. https://doi.org/10.1002/sd.2163

Baker, A. R., & Croot, P. L. (2010). Atmospheric and marine controls on aerosol iron solubility in seawater. *Marine Chemistry*, *120*(1), 4–13. https://doi.org/10.1016/j.marchem.2008.09.003

Banza Lubaba Nkulu, C., Casas, L., Haufroid, V., De Putter, T., Saenen, N. D., Kayembe-Kitenge, T., et al. (2018). Sustainability of artisanal mining of cobalt in DR Congo. *Nature Sustainability*, *1*(9), 495–504. https://doi.org/10.1038/s41893-018-0139-4

Basu, S., & Mackey, K. R. M. (2018). Phytoplankton as Key Mediators of the Biological Carbon Pump: Their Responses to a Changing Climate. *Sustainability*, *10*(3), 869. https://doi.org/10.3390/su10030869

Behrenfeld, M. J., & Falkowski, P. G. (1997). Photosynthetic rates derived from satellite-based chlorophyll concentration. *Limnology and Oceanography*, *42*(1), 1–20. https://doi.org/10.4319/lo.1997.42.1.0001

Bond, T. C., Streets, D. G., Yarber, K. F., Nelson, S. M., Woo, J.-H., & Klimont, Z. (2004). A technology-based global inventory of black and organic carbon emissions from combustion. *Journal of Geophysical Research: Atmospheres*, *109*(D14). https://doi.org/10.1029/2003JD003697

Boyd, P. W., Arrigo, K. R., Strzepek, R., & van Dijken, G. L. (2012). Mapping phytoplankton iron utilization: Insights into Southern Ocean supply mechanisms. *Journal of Geophysical Research: Oceans*, *117*(C6). https://doi.org/10.1029/2011JC007726

Boyd, Philip W., Ellwood, M. J., Tagliabue, A., & Twining, B. S. (2017). Biotic and abiotic retention, recycling and remineralization of metals in the ocean. *Nature Geoscience*, *10*(3), 167–173. https://doi.org/10.1038/ngeo2876

Buitenhuis, E. T., Hashioka, T., & Quéré, C. L. (2013). Combined constraints on global ocean primary production using observations and models. *Global Biogeochemical Cycles*, *27*(3), 847–858. https://doi.org/10.1002/gbc.20074

Cakmur, R. V., Miller, R. L., Perlwitz, J., Geogdzhayev, I. V., Ginoux, P., Koch, D., et al. (2006). Constraining the magnitude of the global dust cycle by minimizing the difference between a model and observations. *Journal of Geophysical Research: Atmospheres*, *111*(D6). https://doi.org/10.1029/2005JD005791

Calvo, G., Mudd, G., Valero, A., & Valero, A. (2016). Decreasing Ore Grades in Global Metallic Mining: A Theoretical Issue or a Global Reality? *Resources*, *5*(4), 36. https://doi.org/10.3390/resources5040036

Capotondi, A., Alexander, M. A., Bond, N. A., Curchitser, E. N., & Scott, J. D. (2012). Enhanced upper ocean stratification with climate change in the CMIP3 models. *Journal of Geophysical Research: Oceans*, *117*(C4). https://doi.org/10.1029/2011JC007409

Chen, L., Gao, Y., Zhang, M., Fu, J. S., Zhu, J., Liao, H., et al. (2019). MICS-Asia III: multi-model comparison and evaluation of aerosol over East Asia. *Atmospheric Chemistry and Physics*, *19*(18), 11911–11937. https://doi.org/10.5194/acp-19-11911-2019

Chueinta, W., Hopke, P. K., & Paatero, P. (2000). Investigation of sources of atmospheric aerosol at urban and suburban residential areas in Thailand by positive matrix factorization. *Atmospheric Environment*, *34*(20), 3319–3329. https://doi.org/10.1016/S1352-2310(99)00433-1

Crippa, M., Guizzardi, D., Muntean, M., Schaaf, E., Dentener, F., Van Aardenne, J. A., et al. (2018). Gridded emissions of air pollutants for the period 1970-2012 within EDGAR v4.3.2. *Earth System Science Data*. https://doi.org/10.5194/essd-10-1987-2018

Csavina, J., Landázuri, A., Wonaschütz, A., Rine, K., Rheinheimer, P., Barbaris, B., et al. (2011). Metal and Metalloid Contaminants in Atmospheric Aerosols from Mining Operations. *Water, Air, & Soil Pollution*, *221*(1), 145–157. https://doi.org/10.1007/s11270-011-0777-x

Dai, S., Chou, C.-L., Yue, M., Luo, K., & Ren, D. (2005). Mineralogy and geochemistry of a Late Permian coal in the Dafang Coalfield, Guizhou, China: influence from siliceous and iron-rich calcic hydrothermal fluids. *International Journal of Coal Geology*, *61*(3), 241–258. https://doi.org/10.1016/j.coal.2004.09.002

Das, S., Pandey, D., Thomas, J., & Roy, T. (2019). The Role of Graphene and Other 2D Materials in Solar Photovoltaics. *Advanced Materials*, *31*(1), 1802722. https://doi.org/10.1002/adma.201802722

DeVries, T., & Weber, T. (2017). The export and fate of organic matter in the ocean: New constraints from combining satellite and oceanographic tracer observations. *Global Biogeochemical Cycles*, *31*(3), 535–555. https://doi.org/10.1002/2016GB005551

Dong, H., Kukkadapu, R. K., Fredrickson, J. K., Zachara, J. M., Kennedy, D. W., & Kostandarithes, H. M. (2003). Microbial Reduction of Structural Fe(III) in Illite and Goethite. *Environmental Science & Technology*, *37*(7), 1268–1276. https://doi.org/10.1021/es020919d

Dudka, S., & Adriano, D. C. (1997). Environmental Impacts of Metal Ore Mining and Processing: A Review. *Journal of Environmental Quality*, *26*(3), 590–602. https://doi.org/10.2134/jeq1997.00472425002600030003x

Ericsson, T., Wäppling, R., & Punakivi, K. (1977). Mössbauer spectroscopy applied to clay and related minerals. *Geologiska Föreningen i Stockholm Förhandlingar*, *99*(3), 229–244. https://doi.org/10.1080/11035897709455018

European Commission. (2020). Critical Raw Materials Resilience: Charting a Path towards greater Security and Sustainability. Retrieved from https://eur-lex.europa.eu/legal-content/EN/TXT/?uri=CELEX:52020DC0474

Flagan, R. C., & Seinfeld, J. H. (2012). *Fundamentals of Air Pollution Engineering*. Courier Corporation.

Fricko, O., Havlik, P., Rogelj, J., Klimont, Z., Gusti, M., Johnson, N., et al. (2017). The marker quantification of the Shared Socioeconomic Pathway 2: A middle-of-the-road scenario for the 21st century. *Global Environmental Change*, *42*, 251–267. https://doi.org/10.1016/j.gloenvcha.2016.06.004

Fu, H., Lin, J., Shang, G., Dong, W., Grassian, V. H., Carmichael, G. R., et al. (2012). Solubility of Iron from Combustion Source Particles in Acidic Media Linked to Iron Speciation. *Environmental Science & Technology*, *46*(20), 11119–11127. https://doi.org/10.1021/es302558m

Gastwirth, J. L. (1972). The Estimation of the Lorenz Curve and Gini Index. *The Review of Economics and Statistics*, *54*(3), 306–316. https://doi.org/10.2307/1937992

Ge, E., Lai, K., Xiao, X., Luo, M., Fang, Z., Zeng, Y., et al. (2018). Differential effects of size-specific particulate matter on emergency department visits for respiratory and cardiovascular diseases in Guangzhou, China. *Environmental Pollution*, *243*, 336–345. https://doi.org/10.1016/j.envpol.2018.08.068

Ghose, M. K., & Majee, S. R. (2001). Air pollution caused by opencast mining and its abatement measures in India. *Journal of Environmental Management*, *63*(2), 193–202. https://doi.org/10.1006/jema.2001.0434

Giurco, D., Dominish, E., Florin, N., Watari, T., & McLellan, B. (2019a). Requirements for minerals and metals for 100% renewable scenarios. In *Achieving the Paris Climate Agreement Goals: Global and Regional 100% Renewable Energy Scenarios with Non-Energy GHG Pathways for +1.5C and +2C* (pp. 437–457). Springer International Publishing. https://doi.org/10.1007/978-3-030-05843-2_11

Giurco, D., Dominish, E., Florin, N., Watari, T., & McLellan, B. (2019b). Requirements for Minerals and Metals for 100% Renewable Scenarios. In S. Teske (Ed.), *Achieving the Paris Climate Agreement Goals: Global and Regional 100% Renewable Energy Scenarios with Non-energy GHG Pathways for +1.5°C and +2°C* (pp. 437–457). Cham: Springer International Publishing. https://doi.org/10.1007/978-3-030-05843-2_11

Hahnel, R. (2020). Economic Justice: Confronting Dilemmas. *Journal of Economic Issues*, *54*(1), 19–37. https://doi.org/10.1080/00213624.2020.1720561

Hamilton, D. S., Scanza, R. A., Feng, Y., Guinness, J., Kok, J. F., Li, L., et al. (2019). Improved methodologies for Earth system modelling of atmospheric soluble iron and observation comparisons using the Mechanism of Intermediate complexity for Modelling Iron (MIMI v1.0). *Geoscientific Model Development*, *12*(9), 3835–3862. https://doi.org/10.5194/gmd-12-3835-2019

Hamilton, D. S., Moore, J. K., Arneth, A., Bond, T. C., Carslaw, K. S., Hantson, S., et al. (2020). Impact of Changes to the Atmospheric Soluble Iron Deposition Flux on Ocean Biogeochemical Cycles in the Anthropocene. *Global Biogeochemical Cycles*, *34*(3), e2019GB006448. https://doi.org/10.1029/2019GB006448

Hamilton, D. S., Scanza, R. A., Rathod, S. D., Bond, T. C., Kok, J. F., Li, L., et al. (2020). Recent (1980 to 2015) Trends and Variability in Daily-to-Interannual Soluble Iron Deposition from Dust, Fire, and Anthropogenic Sources. *Geophysical Research Letters*, *47*(17), e2020GL089688. https://doi.org/10.1029/2020GL089688

Hand, J. L., Schichtel, B. A., Pitchford, M., Malm, W. C., & Frank, N. H. (2012). Seasonal composition of remote and urban fine particulate matter in the United States. *Journal of Geophysical Research: Atmospheres*, *117*(D5). https://doi.org/10.1029/2011JD017122

Harris, E., Sinha, B., Hoppe, P., Crowley, J. N., Ono, S., & Foley, S. (2012). Sulfur isotope fractionation during oxidation of sulfur dioxide: gas-phase oxidation by OH radicals and aqueous oxidation by H_2O_2, O_3 and iron catalysis. *Atmospheric Chemistry and Physics*, *12*(1), 407–423. https://doi.org/10.5194/acp-12-407-2012

Hedberg, E., Gidhagen, L., & Johansson, C. (2005). Source contributions to PM10 and arsenic concentrations in Central Chile using positive matrix factorization. *Atmospheric Environment*, *39*(3), 549–561. https://doi.org/10.1016/j.atmosenv.2004.11.001

Hoesly, R. M., Smith, S. J., Feng, L., Klimont, Z., Janssens-Maenhout, G., Pitkanen, T., et al. (2018). Historical (1750–2014) anthropogenic emissions of reactive gases and aerosols from the Community Emissions Data System (CEDS). *Geoscientific Model Development*, *11*(1), 369–408. https://doi.org/10.5194/gmd-11-369-2018

Huang, R., Zhai, X., Ivey, C. E., Friberg, M. D., Hu, X., Liu, Y., et al. (2018). Air pollutant exposure field modeling using air quality model-data fusion methods and comparison with satellite AOD-derived fields: application over North Carolina, USA. *Air Quality, Atmosphere & Health*, *11*(1), 11–22. https://doi.org/10.1007/s11869-017-0511-y

Huertas, J. I., Camacho, D. A., & Huertas, M. E. (2012). Standardized emissions inventory methodology for open-pit mining areas. *Environmental Science and Pollution Research*, *19*(7), 2784–2794. https://doi.org/10.1007/s11356-012-0778-3

Hurrell, J. W., Holland, M. M., Gent, P. R., Ghan, S., Kay, J. E., Kushner, P. J., et al. (2013). The Community Earth System Model: A Framework for Collaborative Research. *Bulletin of the American Meteorological Society*, *94*(9), 1339–1360. https://doi.org/10.1175/BAMS-D-12-00121.1

Iacono, M. J., Delamere, J. S., Mlawer, E. J., Shephard, M. W., Clough, S. A., & Collins, W. D. (2008). Radiative forcing by long-lived greenhouse gases: Calculations with the AER radiative transfer models. *Journal of Geophysical Research: Atmospheres*, *113*(D13). https://doi.org/10.1029/2008JD009944

IEA. (2021). The Role of Critical Minerals in Clean Energy Transitions. IEA. Retrieved from https://www.iea.org/reports/the-role-of-critical-minerals-in-clean-energy-transitions

International Energy Agency. (n.d.). IEA, 2020. Retrieved September 3, 2021, from https://www.iea.org/reports/world-energy-outlook-2020

Ito, A. (2015). Atmospheric Processing of Combustion Aerosols as a Source of Bioavailable Iron. *Environmental Science & Technology Letters*, *2*(3), 70–75. https://doi.org/10.1021/acs.estlett.5b00007

Ito, A., Lin, G., & Penner, J. E. (2018). Radiative forcing by light-absorbing aerosols of pyrogenetic iron oxides. *Scientific Reports*, *8*(1), 7347. https://doi.org/10.1038/s41598-018-25756-3

Ito, A., Myriokefalitakis, S., Kanakidou, M., Mahowald, N. M., Scanza, R. A., Hamilton, D. S., et al. (2019). Pyrogenic iron: The missing link to high iron solubility in aerosols. *Science Advances*, *5*(5), eaau7671. https://doi.org/10.1126/sciadv.aau7671

Ito, T., Nenes, A., Johnson, M. S., Meskhidze, N., & Deutsch, C. (2016). Acceleration of oxygen decline in the tropical Pacific over the past decades by aerosol pollutants. *Nature Geoscience*, *9*(6), 443–447. https://doi.org/10.1038/ngeo2717

Jepson, W. B. (1988). Structural iron in kaolinites and in associated ancillary minerals. *Iron in Soils and Clay Minerals / Edited by J.W. Stucki, B.A. Goodman, U. Schwertmann*. Retrieved from https://scholar.google.com/scholar_lookup?title=Structural+iron+in+kaolinites+and+in+associated+ancillary+minerals&author=Jepson%2C+W.B.&publication_year=1988

Johnston, J. H., & Cardile, C. M. (1987). Iron Substitution in Montmorillonite, Illite, and Glauconite by 57Fe Mössbauer Spectroscopy. *Clays and Clay Minerals*, *35*(3), 170–176. https://doi.org/10.1346/CCMN.1987.0350302

Jorquera, H., & Barraza, F. (2012a). Source apportionment of ambient PM2.5 in Santiago, Chile: 1999 and 2004 results. *Science of the Total Environment*, *435–436*, 418–429. https://doi.org/10.1016/j.scitotenv.2012.07.049

Jorquera, H., & Barraza, F. (2012b). Source apportionment of ambient PM2.5 in Santiago, Chile: 1999 and 2004 results. *Science of The Total Environment*, *435–436*, 418–429. https://doi.org/10.1016/j.scitotenv.2012.07.049

Journet, E., Desboeufs, K. V., Caquineau, S., & Colin, J.-L. (2008). Mineralogy as a critical factor of dust iron solubility. *Geophysical Research Letters*, *35*(7). https://doi.org/10.1029/2007GL031589

Kaunda, R. B. (2020). Potential environmental impacts of lithium mining. *Journal of Energy & Natural Resources Law*, *38*(3), 237–244. https://doi.org/10.1080/02646811.2020.1754596

Kavouras, I. G., Koutrakis, P., Cereceda-Balic, F., & Oyola, P. (2001a). Source apportionment of PM10 and PM2.5 in five Chilean cities using factor analysis. *Journal of the Air and Waste Management Association*, *51*(3), 451–464. https://doi.org/10.1080/10473289.2001.10464273

Kavouras, I. G., Koutrakis, P., Cereceda-Balic, F., & Oyola, P. (2001b). Source Apportionment of PM10 and PM25 in Five Chilean Cities Using Factor Analysis. *Journal of the Air & Waste Management Association*, *51*(3), 451–464. https://doi.org/10.1080/10473289.2001.10464273

Kim, E., Hopke, P. K., & Edgerton, E. S. (2003). Source Identification of Atlanta Aerosol by Positive Matrix Factorization. *Journal of the Air & Waste Management Association*, *53*(6), 731–739. https://doi.org/10.1080/10473289.2003.10466209

Kim, Y. H., Krantz, Q. T., McGee, J., Kovalcik, K. D., Duvall, R. M., Willis, R. D., et al. (2016). Chemical composition and source apportionment of size fractionated particulate matter in Cleveland, Ohio, USA. *Environmental Pollution*, *218*, 1180–1190. https://doi.org/10.1016/j.envpol.2016.08.073

Klimont, Z., Cofala, J., Bertok, I., Amann, M., Heyes, C., & Gyarfas, F. (2002). Modelling Particulate Emissions in Europe. *IIASA, Interim Report*, *IR-02-076*.

Klimont, Zbigniew, Kupiainen, K., Heyes, C., Purohit, P., Cofala, J., Rafaj, P., et al. (2017a). Global anthropogenic emissions of particulate matter including black carbon. *Atmospheric Chemistry and Physics*, *17*(14), 8681–8723. https://doi.org/10.5194/acp-17-8681-2017

Klimont, Zbigniew, Kupiainen, K., Heyes, C., Purohit, P., Cofala, J., Rafaj, P., et al. (2017b). Global anthropogenic emissions of particulate matter including black carbon. *Atmospheric Chemistry and Physics*, *17*(14), 8681–8723. https://doi.org/10.5194/acp-17-8681-2017

Kotronarou, A., & Sigg, L. (1993). Sulfur dioxide oxidation in atmospheric water: role of iron(II) and effect of ligands. *Environmental Science & Technology*, *27*(13), 2725–2735. https://doi.org/10.1021/es00049a011

Krishnamurthy, A., Moore, J. K., Mahowald, N., Luo, C., Doney, S. C., Lindsay, K., & Zender, C. S. (2009). Impacts of increasing anthropogenic soluble iron and nitrogen deposition on ocean biogeochemistry. *Global Biogeochemical Cycles*, *23*(3). https://doi.org/10.1029/2008GB003440

Kurisu, M., Sakata, K., Uematsu, M., Ito, A., & Takahashi, Y. (2021). Contribution of combustion Fe in marine aerosols over the northwestern Pacific estimated by Fe stable isotope ratios. *Atmospheric Chemistry and Physics*, *21*(20), 16027–16050. https://doi.org/10.5194/acp-21-16027-2021

Lafon, S., Sokolik, I. N., Rajot, J. L., Caquineau, S., & Gaudichet, A. (2006). Characterization of iron oxides in mineral dust aerosols: Implications for light absorption. *Journal of Geophysical Research: Atmospheres*, *111*(D21). https://doi.org/10.1029/2005JD007016

Lamarque, J.-F., Bond, T. C., Eyring, V., Granier, C., Heil, A., Klimont, Z., et al. (2010). Historical (1850–2000) gridded anthropogenic and biomass burning emissions of reactive gases and aerosols: methodology and application. *Atmospheric Chemistry and Physics*, *10*(15), 7017–7039. https://doi.org/10.5194/acp-10-7017-2010

Lamb, K. D., Matsui, H., Katich, J. M., Perring, A. E., Spackman, J. R., Weinzierl, B., et al. (2021). Global-scale constraints on light-absorbing anthropogenic iron oxide aerosols. *Npj Climate and Atmospheric Science*, *4*(1), 1–12. https://doi.org/10.1038/s41612-021-00171-0

Le Quéré, C., Andrew, R. M., Friedlingstein, P., Sitch, S., Hauck, J., Pongratz, J., et al. (2018). Global Carbon Budget 2018. *Earth System Science Data*, *10*(4), 2141–2194. https://doi.org/10.5194/essd-10-2141-2018

Lèbre, É., Stringer, M., Svobodova, K., Owen, J. R., Kemp, D., Côte, C., et al. (2020). The social and environmental complexities of extracting energy transition metals. *Nature Communications*, *11*(1), 4823. https://doi.org/10.1038/s41467-020-18661-9

Lee, Y. H., Lamarque, J.-F., Flanner, M. G., Jiao, C., Shindell, D. T., Berntsen, T., et al. (2013). Evaluation of preindustrial to present-day black carbon and its albedo forcing from Atmospheric Chemistry and Climate Model Intercomparison Project (ACCMIP). *Atmospheric Chemistry and Physics*, *13*(5), 2607–2634. https://doi.org/10.5194/acp-13-2607-2013

Li, L., Mahowald, N. M., Miller, R. L., Pérez García-Pando, C., Klose, M., Hamilton, D. S., et al. (2021). Quantifying the range of the dust direct radiative effect due to source mineralogy uncertainty. *Atmospheric Chemistry and Physics*, *21*(5), 3973–4005. https://doi.org/10.5194/acp-21-3973-2021

Lin, J., Pan, D., Davis, S. J., Zhang, Q., He, K., Wang, C., et al. (2014). China's international trade and air pollution in the United States. *Proceedings of the National Academy of Sciences*, *111*(5), 1736–1741. https://doi.org/10.1073/pnas.1312860111

Liu, M., Matsui, H., Hamilton, D. S., Lamb, K. D., Rathod, S. D., Schwarz, J. P., & Mahowald, N. M. (2022). The underappreciated role of anthropogenic sources in atmospheric soluble iron flux to the Southern Ocean. *Npj Climate and Atmospheric Science*, *5*(1), 1–9. https://doi.org/10.1038/s41612-022-00250-w

Liu, X., Ma, P.-L., Wang, H., Tilmes, S., Singh, B., Easter, R. C., et al. (2016). Description and evaluation of a new four-mode version of the Modal Aerosol Module (MAM4) within version 5.3 of the Community Atmosphere Model. *Geoscientific Model Development*, *9*(2), 505–522. https://doi.org/10.5194/gmd-9-505-2016

Lorenz, M. O. (1905). Methods of Measuring the Concentration of Wealth. *Publications of the American Statistical Association*, *9*(70), 209–219. https://doi.org/10.2307/2276207

Luo, C., Mahowald, N., Bond, T., Chuang, P. Y., Artaxo, P., Siefert, R., et al. (2008). Combustion iron distribution and deposition. *Global Biogeochemical Cycles*, *22*(1). https://doi.org/10.1029/2007GB002964

Ma, L., Sun, J., Yang, Z., & Wang, L. (2015). Heavy metal contamination of agricultural soils affected by mining activities around the Ganxi River in Chenzhou, Southern China. *Environmental Monitoring and Assessment*, *187*(12), 731. https://doi.org/10.1007/s10661-015-4966-8

Mahowald, N. M., Zender, C. S., Luo, C., Savoie, D., Torres, O., & del Corral, J. (2002). Understanding the 30-year Barbados desert dust record. *Journal of Geophysical Research: Atmospheres*, *107*(D21), AAC 7-1-AAC 7-16. https://doi.org/10.1029/2002JD002097

Mahowald, N. M., Engelstaedter, S., Luo, C., Sealy, A., Artaxo, P., Benitez-Nelson, C., et al. (2009). Atmospheric Iron Deposition: Global Distribution, Variability, and Human Perturbations. *Annual Review of Marine Science*, *1*(1), 245–278. https://doi.org/10.1146/annurev.marine.010908.163727

Mahowald, N. M., Hamilton, D. S., Mackey, K. R. M., Moore, J. K., Baker, A. R., Scanza, R. A., & Zhang, Y. (2018). Aerosol trace metal leaching and impacts on marine microorganisms. *Nature Communications*, *9*(1), 2614. https://doi.org/10.1038/s41467-018-04970-7

Martin, J. H., Fitzwater, S. E., & Gordon, R. M. (1990). Iron deficiency limits phytoplankton growth in Antarctic waters. *Global Biogeochemical Cycles*, *4*(1), 5–12. https://doi.org/10.1029/GB004i001p00005

Martin, R. V., Jacob, D. J., Chance, K., Kurosu, T. P., Palmer, P. I., & Evans, M. J. (2003). Global inventory of nitrogen oxide emissions constrained by space-based observations of NO2 columns. *Journal of Geophysical Research: Atmospheres*, *108*(D17). https://doi.org/10.1029/2003JD003453

Masson-Delmotte, V., Zhai, P., Pirani, A., Connors, S. L., Péan, C., Berger, S., et al. (Eds.). (2021). Summary for policymakers. In *Climate Change 2021: The Physical Science Basis. Contribution of Working Group I to the Sixth Assessment Report of the Intergovernmental Panel on Climate Change*. Cambridge University Press.

Matsui, H., Mahowald, N. M., Moteki, N., Hamilton, D. S., Ohata, S., Yoshida, A., et al. (2018). Anthropogenic combustion iron as a complex climate forcer. *Nature Communications*, *9*(1), 1593. https://doi.org/10.1038/s41467-018-03997-0

Matsui, H., Hamilton, D. S., & Mahowald, N. M. (2018). Black carbon radiative effects highly sensitive to emitted particle size when resolving mixing-state diversity. *Nature Communications*, *9*(1), 3446. https://doi.org/10.1038/s41467-018-05635-1

McCauley, D., & Heffron, R. (2018). Just transition: Integrating climate, energy and environmental justice. *Energy Policy*, *119*, 1–7. https://doi.org/10.1016/j.enpol.2018.04.014

Menut, L., Forêt, G., & Bergametti, G. (2007). Sensitivity of mineral dust concentrations to the model size distribution accuracy. *Journal of Geophysical Research: Atmospheres*, *112*(D10). https://doi.org/10.1029/2006JD007766

Mermut†, A. R., & Cano, A. F. (2001). BASELINE STUDIES OF THE CLAY MINERALS SOCIETY SOURCE CLAYS: CHEMICAL ANALYSES OF MAJOR ELEMENTS. *Clays and Clay Minerals*, *49*(5), 381–386.

Meskhidze, N., Völker, C., Al-Abadleh, H. A., Barbeau, K., Bressac, M., Buck, C., et al. (2019). Perspective on identifying and characterizing the processes controlling iron speciation and residence time at the atmosphere-ocean interface. *Marine Chemistry*, *217*, 103704. https://doi.org/10.1016/j.marchem.2019.103704

Mestdagh, M. M., Vielvoye, L., & Herbillon, A. J. (1980). Iron in kaolinite: II. The relationship between kaolinite crystallinity and iron content. *Clay Minerals*, *15*(1), 1–13. https://doi.org/10.1180/claymin.1980.015.1.01

Michael, P. J., & McWhinnie, W. R. (1989). Mössbauer and esr studies of the thermochemistry of illite and montmorillonite. *Polyhedron*, *8*(22), 2709–2718. https://doi.org/10.1016/S0277-5387(00)80443-X

Moeng, K. (2019). Community perceptions on the health risks of acid mine drainage: the environmental justice struggles of communities near mining fields. *Environment, Development and Sustainability*, *21*(6), 2619–2640. https://doi.org/10.1007/s10668-018-0149-4

Mohr, S., Giurco, D., Yellishetty, M., Ward, J., & Mudd, G. (2015). Projection of Iron Ore Production. *Natural Resources Research*, *24*(3), 317–327. https://doi.org/10.1007/s11053-014-9256-6

Moore, C. M., Mills, M. M., Arrigo, K. R., Berman-Frank, I., Bopp, L., Boyd, P. W., et al. (2013). Processes and patterns of oceanic nutrient limitation. *Nature Geoscience*, *6*(9), 701–710. https://doi.org/10.1038/ngeo1765

Moore, J. K., Doney, S. C., Glover, D. M., & Fung, I. Y. (2001). Iron cycling and nutrient-limitation patterns in surface waters of the World Ocean. *Deep Sea Research Part II: Topical Studies in Oceanography*, *49*(1), 463–507. https://doi.org/10.1016/S0967-0645(01)00109-6

Moteki, N., Adachi, K., Ohata, S., Yoshida, A., Harigaya, T., Koike, M., & Kondo, Y. (2017). Anthropogenic iron oxide aerosols enhance atmospheric heating. *Nature Communications*, *8*(1), 15329. https://doi.org/10.1038/ncomms15329

Murad, E., & Wagner, U. (1994). The Mössbauer Spectrum of Illite. *Clay Minerals*, *29*(1), 1–10. https://doi.org/10.1180/claymin.1994.029.1.01

Mwaanga, P., Silondwa, M., Kasali, G., & Banda, P. M. (2019). Preliminary review of mine air pollution in Zambia. *Heliyon*, *5*(9), e02485. https://doi.org/10.1016/j.heliyon.2019.e02485

Myriokefalitakis, S., Gröger, M., Hieronymus, J., & Döscher, R. (2020). An explicit estimate of the atmospheric nutrient impact on global oceanic productivity. *Ocean Science*, *16*(5), 1183–1205. https://doi.org/10.5194/os-16-1183-2020

Myriokefalitakis, Stelios, Ito, A., Kanakidou, M., Nenes, A., Krol, M. C., Mahowald, N. M., et al. (2018). Reviews and syntheses: the GESAMP atmospheric iron deposition model intercomparison study. *Biogeosciences*, *15*(21), 6659–6684. https://doi.org/10.5194/bg-15-6659-2018

Nassar, N. T., Brainard, J., Gulley, A., Manley, R., Matos, G., Lederer, G., et al. (2020). Evaluating the mineral commodity supply risk of the U.S. manufacturing sector. *Science Advances*. https://doi.org/10.1126/sciadv.aay8647

Naz, A., Mishra, B. K., & Gupta, S. K. (2016). Human Health Risk Assessment of Chromium in Drinking Water: A Case Study of Sukinda Chromite Mine, Odisha, India. *Exposure and Health*, *8*(2), 253–264. https://doi.org/10.1007/s12403-016-0199-5

Northey, S., Mohr, S., Mudd, G. M., Weng, Z., & Giurco, D. (2014). Modelling future copper ore grade decline based on a detailed assessment of copper resources and mining. *Resources, Conservation and Recycling*, *83*, 190–201. https://doi.org/10.1016/j.resconrec.2013.10.005

Nriagu, J. O. (1979). Global inventory of natural and anthropogenic emissions of trace metals to the atmosphere [7]. *Nature*. https://doi.org/10.1038/279409a0

Nriagu, J. O., & Pacyna, J. M. (1988). Quantitative assessment of worldwide contamination of air, water and soils by trace metals. *Nature*, *333*(6169), 134–139. https://doi.org/10.1038/333134a0

Oakes, M., Ingall, E. D., Lai, B., Shafer, M. M., Hays, M. D., Liu, Z. G., et al. (2012). Iron Solubility Related to Particle Sulfur Content in Source Emission and Ambient Fine Particles. *Environmental Science & Technology*, *46*(12), 6637–6644. https://doi.org/10.1021/es300701c

Ohata, S., Yoshida, A., Moteki, N., Adachi, K., Takahashi, Y., Kurisu, M., & Koike, M. (2018). Abundance of Light-Absorbing Anthropogenic Iron Oxide Aerosols in the Urban Atmosphere and Their Emission Sources. *Journal of Geophysical Research: Atmospheres*, *123*(15), 8115–8134. https://doi.org/10.1029/2018JD028363

Okin, G. S., Baker, A. R., Tegen, I., Mahowald, N. M., Dentener, F. J., Duce, R. A., et al. (2011a). Impacts of atmospheric nutrient deposition on marine productivity: Roles of nitrogen, phosphorus, and iron. *Global Biogeochemical Cycles*, *25*(2), n/a-n/a. https://doi.org/10.1029/2010GB003858

Okin, G. S., Baker, A. R., Tegen, I., Mahowald, N. M., Dentener, F. J., Duce, R. A., et al. (2011b). Impacts of atmospheric nutrient deposition on marine productivity: Roles of nitrogen, phosphorus, and iron. *Global Biogeochemical Cycles*, *25*(2). https://doi.org/10.1029/2010GB003858

Paatero, P. (1997). Least squares formulation of robust non-negative factor analysis. *Chemometrics and Intelligent Laboratory Systems*, *37*(1), 23–35. https://doi.org/10.1016/S0169-7439(96)00044-5

Paatero, P., & Tapper, U. (1994). Positive matrix factorization: A non-negative factor model with optimal utilization of error estimates of data values. *Environmetrics*, *5*(2), 111–126. https://doi.org/10.1002/env.3170050203

Pacyna, Josef M., Semb, A., & Hanssen, J. E. (1984). Emission and long-range transport of trace elements in Europe. *Tellus B: Chemical and Physical Meteorology*, *36*(3), 163–178. https://doi.org/10.3402/tellusb.v36i3.14886

Pacyna, Jozef M., & Pacyna, E. G. (2001). An assessment of global and regional emissions of trace metals to the atmosphere from anthropogenic sources worldwide. *Environmental Reviews*. https://doi.org/10.1139/a01-012

Parveen, S. M. A., Suganyaa, B., Sathya, M. S., Margreat, A. A. P., Sivasankari, K., Shanmughapriya, S., et al. (2016). Leptospirosis Seroprevalence among Blue Metal Mine Workers of Tamil Nadu, India.

The American Journal of Tropical Medicine and Hygiene, *95*(1), 38–42. https://doi.org/10.4269/ajtmh.16-0095

Pinedo-González, P., Hawco, N. J., Bundy, R. M., Armbrust, E. V., Follows, M. J., Cael, B. B., et al. (2020). Anthropogenic Asian aerosols provide Fe to the North Pacific Ocean. *Proceedings of the National Academy of Sciences*, *117*(45), 27862–27868. https://doi.org/10.1073/pnas.2010315117

Pingitore, N. E., Jr. (2019). Unlocking a Strategic National Treasure: Multiple Critical and "Green" Minerals in Round Top Mt. Rhyolite, Far West Texas, U.S.A., *2019*, PA41C-1130.

Querry, M. (1987). *Optical Constants of Minerals and Other Materials from the Millimeter to the Ultraviolet*. CHEMICAL RESEARCH DEVELOPMENT AND ENGINEERING CENTER ABERDEEN PROVING GROUNDMD. Retrieved from https://apps.dtic.mil/sti/citations/ADA192210

Querry, M. R. (1985). *Optical Constants*. MISSOURI UNIV-KANSAS CITY. Retrieved from https://apps.dtic.mil/sti/citations/ADA158623

Råde, I., & Andersson, B. A. (2001). Requirement for metals of electric vehicle batteries. *Journal of Power Sources*, *93*(1–2), 55–71. https://doi.org/10.1016/S0378-7753(00)00547-4

Rafaj, P., Kiesewetter, G., Gül, T., Schöpp, W., Cofala, J., Klimont, Z., et al. (2018). Outlook for clean air in the context of sustainable development goals. *Global Environmental Change*, *53*, 1–11. https://doi.org/10.1016/j.gloenvcha.2018.08.008

Ramadan, Z., Song, X.-H., & Hopke, P. K. (2000). Identification of Sources of Phoenix Aerosol by Positive Matrix Factorization. *Journal of the Air & Waste Management Association*, *50*(8), 1308–1320. https://doi.org/10.1080/10473289.2000.10464173

Ramaswamy, V., Boucher, O., Haigh, J., Hauglustaine, D., Haywood, J., Myhre, G., et al. (n.d.). Radiative Forcing of Climate Change, 68.

Rathod, S. D., Hamilton, D. S., Mahowald, N. M., Klimont, Z., Corbett, J. J., & Bond, T. C. (2020a). A Mineralogy-Based Anthropogenic Combustion-Iron Emission Inventory. *Journal of Geophysical Research: Atmospheres*, *125*(17), e2019JD032114. https://doi.org/10.1029/2019JD032114

Rathod, S. D., Hamilton, D. S., Mahowald, N. M., Klimont, Z., Corbett, J. J., & Bond, T. C. (2020b). A mineralogy-based anthropogenic combustion-iron emission inventory. *Journal of Geophysical Research: Atmospheres*, e2019JD032114. https://doi.org/10.1029/2019JD032114

Rathod, Sagar D., Bond, T. C., Klimont, Z., Pierce, J. R., Mahowald, N., Roy, C., et al. (2022). Future PM$\less$sub$\greater$2.5$\less$/sub$\greater$ emissions from metal production to meet renewable energy demand. *Environmental Research Letters*, *17*(4), 044043. https://doi.org/10.1088/1748-9326/ac5d9c

Rauch, J. N., & Pacyna, J. M. (2009). Earth's global Ag, Al, Cr, Cu, Fe, Ni, Pb, and Zn cycles. *Global Biogeochemical Cycles*, *23*(2), 1–16. https://doi.org/10.1029/2008GB003376

Rienecker, M. M., Suarez, M. J., Gelaro, R., Todling, R., Bacmeister, J., Liu, E., et al. (2011). MERRA: NASA's Modern-Era Retrospective Analysis for Research and Applications. *Journal of Climate*, *24*(14), 3624–3648. https://doi.org/10.1175/JCLI-D-11-00015.1

Samset, B. H., Myhre, G., Herber, A., Kondo, Y., Li, S.-M., Moteki, N., et al. (2014). Modelled black carbon radiative forcing and atmospheric lifetime in AeroCom Phase II constrained by aircraft observations. *Atmospheric Chemistry and Physics*, *14*(22), 12465–12477. https://doi.org/10.5194/acp-14-12465-2014

Sarmiento, J. L., Gloor, M., Gruber, N., Beaulieu, C., Jacobson, A. R., Mikaloff Fletcher, S. E., et al. (2010). Trends and regional distributions of land and ocean carbon sinks. *Biogeosciences*, *7*(8), 2351–2367. https://doi.org/10.5194/bg-7-2351-2010

Scanza, R. A., Mahowald, N., Ghan, S., Zender, C. S., Kok, J. F., Liu, X., et al. (2015). Modeling dust as component minerals in the Community Atmosphere Model: development of framework and impact on radiative forcing. *Atmospheric Chemistry and Physics*, *15*(1), 537–561. https://doi.org/10.5194/acp-15-537-2015

Schoffman, H., Lis, H., Shaked, Y., & Keren, N. (2016). Iron–Nutrient Interactions within Phytoplankton. *Frontiers in Plant Science*, *7*. Retrieved from https://www.frontiersin.org/article/10.3389/fpls.2016.01223

Schroth, A. W., Crusius, J., Sholkovitz, E. R., & Bostick, B. C. (2009). Iron solubility driven by speciation in dust sources to the ocean. *Nature Geoscience*, *2*(5), 337–340. https://doi.org/10.1038/ngeo501

Seefeldt, J. L. (2020). Lessons from the Lithium Triangle: Considering Policy Explanations for the Variation in Lithium Industry Development in the "Lithium Triangle" Countries of Chile, Argentina, and Bolivia. *Politics & Policy*, *48*(4), 727–765. https://doi.org/10.1111/polp.12365

Shaked, Y., & Lis, H. (2012). Disassembling Iron Availability to Phytoplankton. *Frontiers in Microbiology*, *3*. Retrieved from https://www.frontiersin.org/article/10.3389/fmicb.2012.00123

Siegel, D. A., Buesseler, K. O., Doney, S. C., Sailley, S. F., Behrenfeld, M. J., & Boyd, P. W. (2014). Global assessment of ocean carbon export by combining satellite observations and food-web models. *Global Biogeochemical Cycles*, *28*(3), 181–196. https://doi.org/10.1002/2013GB004743

Simangan, D., & Gidley, R. (2019). Exploring the link between mine action and transitional justice in Cambodia. *Global Change, Peace & Security*, *31*(2), 221–243. https://doi.org/10.1080/14781158.2019.1608939

Singh, B., & Gilkes, R. J. (1992). Properties of soil kaolinites from south-western Australia. *Journal of Soil Science*, *43*(4), 645–667. https://doi.org/10.1111/j.1365-2389.1992.tb00165.x

Skinner, B. J. (1979). Earth resources*. *Proceedings of the National Academy of Sciences*, *76*(9), 4212–4217. https://doi.org/10.1073/pnas.76.9.4212

Smith, M. B., Mahowald, N. M., Albani, S., Perry, A., Losno, R., Qu, Z., et al. (2017). Sensitivity of the interannual variability of mineral aerosol simulations to meteorological forcing dataset. *Atmospheric Chemistry and Physics*, *17*(5), 3253–3278. https://doi.org/10.5194/acp-17-3253-2017

Solomon, P. A., Crumpler, D., Flanagan, J. B., Jayanty, R. K. M., Rickman, E. E., & McDade, C. E. (2014). U.S. National PM2.5 Chemical Speciation Monitoring Networks—CSN and IMPROVE: Description of networks. *Journal of the Air & Waste Management Association*, *64*(12), 1410–1438. https://doi.org/10.1080/10962247.2014.956904

Streets, D. G., Bond, T. C., Carmichael, G. R., Fernandes, S. D., Fu, Q., He, D., et al. (2003). An inventory of gaseous and primary aerosol emissions in Asia in the year 2000. *Journal of Geophysical Research: Atmospheres*, *108*(D21). https://doi.org/10.1029/2002JD003093

Sundararajan, S., & Rabe, H. (2021). Prevention of iron deficiency anemia in infants and toddlers. *Pediatric Research*, *89*(1), 63–73. https://doi.org/10.1038/s41390-020-0907-5

Tagliabue, A., Bowie, A. R., Boyd, P. W., Buck, K. N., Johnson, K. S., & Saito, M. A. (2017). The integral role of iron in ocean biogeochemistry. *Nature*, *543*(7643), 51–59. https://doi.org/10.1038/nature21058

Tan, J., Zhang, L., Zhou, X., Duan, J., Li, Y., Hu, J., & He, K. (2017). Chemical characteristics and source apportionment of PM2.5 in Lanzhou, China. *Science of the Total Environment*, *601–602*, 1743–1752. https://doi.org/10.1016/j.scitotenv.2017.06.050

The Paris Agreement | UNFCCC. (n.d.). Retrieved September 3, 2021, from https://unfccc.int/process-and-meetings/the-paris-agreement/the-paris-agreement

Tian, H. Z., Lu, L., Cheng, K., Hao, J. M., Zhao, D., Wang, Y., et al. (2012). Anthropogenic atmospheric nickel emissions and its distribution characteristics in China. *Science of The Total Environment*, *417–418*, 148–157. https://doi.org/10.1016/j.scitotenv.2011.11.069

Tsigaridis, K., Daskalakis, N., Kanakidou, M., Adams, P. J., Artaxo, P., Bahadur, R., et al. (2014). The AeroCom evaluation and intercomparison of organic aerosol in global models. *Atmospheric Chemistry and Physics*, *14*(19), 10845–10895. https://doi.org/10.5194/acp-14-10845-2014

Twining, B. S., & Baines, S. B. (2013). The Trace Metal Composition of Marine Phytoplankton. *Annual Review of Marine Science*, *5*(1), 191–215. https://doi.org/10.1146/annurev-marine-121211-172322

US Department of the Interior, U. (2019). *Mineral Commodity Summaries 2019*. *Handbook of Environmental Chemistry*. https://doi.org/10.1007/978-3-540-47108-0-4

US EPA. (1995). Metallugical Industry. *AP-42, Compilation of Air Pollutant Emission Factors Volume I: Stationary Point and Area Sources*, *86*(1), 1–20.

US EPA, O. (2016, September 26). AP-42: Compilation of Air Emissions Factors [Other Policies and Guidance]. Retrieved September 3, 2021, from https://www.epa.gov/air-emissions-factors-and-quantification/ap-42-compilation-air-emissions-factors

Valero, A., Valero, A., Calvo, G., Ortego, A., Ascaso, S., & Palacios, J.-L. (2018). Global material requirements for the energy transition. An exergy flow analysis of decarbonisation pathways. *Energy*, *159*, 1175–1184. https://doi.org/10.1016/j.energy.2018.06.149

Vecchi, R., Chiari, M., D'Alessandro, A., Fermo, P., Lucarelli, F., Mazzei, F., et al. (2008). A mass closure and PMF source apportionment study on the sub-micron sized aerosol fraction at urban sites in Italy. *Atmospheric Environment*, *42*(9), 2240–2253. https://doi.org/10.1016/j.atmosenv.2007.11.039

Vekasi, K. (2021). The Geoeconomics of Critical Rare Earth Minerals. *Georgetown Journal of International Affairs*, *22*(2), 271–279. https://doi.org/10.1353/gia.2021.0039

Velicu, I. (2019). De-growing environmental justice: Reflections from anti-mining movements in Eastern Europe. *Ecological Economics*, *159*, 271–278. https://doi.org/10.1016/j.ecolecon.2019.01.021

Vijayanand, C., Rajaguru, P., Kalaiselvi, K., Selvam, K. P., & Palanivel, M. (2008). Assessment of heavy metal contents in the ambient air of the Coimbatore city, Tamilnadu, India. *Journal of Hazardous Materials*, *160*(2–3), 548–553. https://doi.org/10.1016/j.jhazmat.2008.03.071

van Vuuren, D. P., Stehfest, E., Gernaat, D. E. H. J., Doelman, J. C., van den Berg, M., Harmsen, M., et al. (2017). Energy, land-use and greenhouse gas emissions trajectories under a green growth paradigm. *Global Environmental Change*, *42*, 237–250. https://doi.org/10.1016/j.gloenvcha.2016.05.008

Wang, R., Balkanski, Y., Boucher, O., Bopp, L., Chappell, A., Ciais, P., et al. (2015). Sources, transport and deposition of iron in the global atmosphere. *Atmospheric Chemistry and Physics*, *15*(11), 6247–6270. https://doi.org/10.5194/acp-15-6247-2015

Wang, Rong, Balkanski, Y., Bopp, L., Aumont, O., Boucher, O., Ciais, P., et al. (2015). Influence of anthropogenic aerosol deposition on the relationship between oceanic productivity and warming. *Geophysical Research Letters*, *42*(24), 10745–10754. https://doi.org/10.1002/2015GL066753

Wang, Yanan, Jia, C., Tao, J., Zhang, L., Liang, X., Ma, J., et al. (2016). Chemical characterization and source apportionment of PM2.5in a semi-arid and petrochemical-industrialized city, Northwest China. *Science of the Total Environment*, *573*, 1031–1040. https://doi.org/10.1016/j.scitotenv.2016.08.179

Wang, Yixiang, Puthussery, J. V., Yu, H., & Verma, V. (2020). Synergistic and antagonistic interactions among organic and metallic components of the ambient particulate matter (PM) for the cytotoxicity measured by Chinese hamster ovary cells. *Science of The Total Environment*, *736*, 139511. https://doi.org/10.1016/j.scitotenv.2020.139511

Watari, T., McLellan, B. C., Giurco, D., Dominish, E., Yamasue, E., & Nansai, K. (2019a). Total material requirement for the global energy transition to 2050: A focus on transport and electricity. *Resources, Conservation and Recycling*, *148*(May), 91–103. https://doi.org/10.1016/j.resconrec.2019.05.015

Watari, T., McLellan, B. C., Giurco, D., Dominish, E., Yamasue, E., & Nansai, K. (2019b). Total material requirement for the global energy transition to 2050: A focus on transport and electricity. *Resources, Conservation and Recycling*, *148*, 91–103. https://doi.org/10.1016/j.resconrec.2019.05.015

Watson, R., Kitchingman, A., Gelchu, A., & Pauly, D. (2004). Mapping global fisheries: sharpening our focus. *Fish and Fisheries*, *5*(2), 168–177. https://doi.org/10.1111/j.1467-2979.2004.00142.x

Wolfram, P., Tu, Q., Heeren, N., Pauliuk, S., & Hertwich, E. G. (2021). Material efficiency and climate change mitigation of passenger vehicles. *Journal of Industrial Ecology*, *25*(2), 494–510. https://doi.org/10.1111/jiec.13067

Wong, M. Y., Rathod, S. D., Marino, R., Li, L., Howarth, R. W., Alastuey, A., et al. (2021). Anthropogenic Perturbations to the Atmospheric Molybdenum Cycle. *Global Biogeochemical Cycles*, *35*(2), e2020GB006787. https://doi.org/10.1029/2020GB006787

World mineral statistics | MineralsUK. (n.d.). Retrieved April 30, 2022, from https://www2.bgs.ac.uk/mineralsuk/statistics/worldStatistics.html

Wu, Q. R., Wang, S. X., Zhang, L., Song, J. X., Yang, H., & Meng, Y. (2012). Update of mercury emissions from China's primary zinc, lead and copper smelters, 2000–2010. *Atmospheric Chemistry and Physics*, *12*(22), 11153–11163. https://doi.org/10.5194/acp-12-11153-2012

Wu, Z., Yang, L., Chen, Q., & Ye, Q. (2021). The impacts of international trade on global greenhouse gas emissions: A thought experiment based on a novel no-trade analysis. *Journal of Environmental Management*, *300*, 113836. https://doi.org/10.1016/j.jenvman.2021.113836

Xu, J., Liu, D., Wu, X., Vu, T. V., Zhang, Y., Fu, P., et al. (2021). Source apportionment of fine organic carbon at an urban site of Beijing using a chemical mass balance model. *Atmospheric Chemistry and Physics*, *21*(9), 7321–7341. https://doi.org/10.5194/acp-21-7321-2021

Xue, Y. H., Wu, J. H., Feng, Y. C., Dai, L., Bi, X. H., Li, X., et al. (2010). Source characterization and apportionment of PM10 in Panzhihua, China. *Aerosol and Air Quality Research*, *10*(4), 367–377. https://doi.org/10.4209/aaqr.2010.01.0002

Yahalom-Mack, N., Galili, E., Segal, I., Eliyahu-Behar, A., Boaretto, E., Shilstein, S., & Finkelstein, I. (2014). New insights into Levantine copper trade: analysis of ingots from the Bronze and Iron Ages in Israel. *Journal of Archaeological Science*, *45*, 159–177. https://doi.org/10.1016/j.jas.2014.02.004

Yoshida, A., Ohata, S., Moteki, N., Adachi, K., Mori, T., Koike, M., & Takami, A. (2018). Abundance and Emission Flux of the Anthropogenic Iron Oxide Aerosols From the East Asian Continental Outflow. *Journal of Geophysical Research: Atmospheres*, *123*(19), 11,194-11,209. https://doi.org/10.1029/2018JD028665

Yuan, Z. B., Yu, J. Z., Lau, A. K. H., Louie, P. K. K., & Fung, J. C. H. (2006). Application of positive matrix factorization in estimating aerosol secondary organic carbon in Hong Kong and its relationship with secondary sulfate. *Atmospheric Chemistry and Physics*, *6*(1), 25–34. https://doi.org/10.5194/acp-6-25-2006

Zhang, Q., Jiang, X., Tong, D., Davis, S. J., Zhao, H., Geng, G., et al. (2017). Transboundary health impacts of transported global air pollution and international trade. *Nature*, *543*(7647), 705–709. https://doi.org/10.1038/nature21712

Zhu, L., Henze, D. K., Cady-Pereira, K. E., Shephard, M. W., Luo, M., Pinder, R. W., et al. (2013). Constraining U.S. ammonia emissions using TES remote sensing observations and the GEOS-Chem adjoint model. *Journal of Geophysical Research: Atmospheres*, *118*(8), 3355–3368. https://doi.org/10.1002/jgrd.50166

APPENDIX A

SUPPLEMENTAL INFORMATION FOR CHAPTER 2

Equation A.1

$$DRF_{1850\text{-}2010} = [In_{SW+LW,2010} - Out_{SW+LW,\,2010}] - [In_{SW+LW,\,1850} - Out_{SW+LW,\,1850}]$$

$DRF_{1850\text{-}2010}$ is the all-sky top-of-atmosphere forcing between the period 1850 and 2010, In_{SW+LW} and Out_{SW+LW} are the incoming and outgoing shortwave (*SW*) and longwave (*LW*) radiation fluxes, respectively. Note that 1850 anthropogenic combustion-iron emissions are assumed to be negligible, hence the present-day direct radiative effect is the same as the 1850-2010 direct radiative forcing by this source.

Equation A.2

$C\text{-}Fixed_{Fedep} = (C/SolubleFe)_{phytoplankton} * SolFe_{dep}$;in basins with surface $NO_3^{-1} > 4\mu M$

C-Fixed$_{Fedep}$ is the mass of carbon fixed (represented as NPP, kg C/m2/yr) due to atmospheric soluble iron deposition with mass units same as $SolFe_{dep}$, *(C/SolubleFe)$_{phytoplankton}$* is the elemental C/SolubleFe ratio in phytoplankton (kg C/kg SolFe), *Fe$_{dep}$* is the atmospheric soluble iron deposition in the units (kg SolFe /m2/yr).

Equation A.3

CO_2 $Forcing_{1850\text{-}2010}$ $(W/m^2) = 5.35 * \ln (CO_{2Without\ anthropogenic,\ 2010}/CO_{2with\ anthropogenic,\ 2010})$

$CO_2Forcing_{1850\text{-}2010}$ is the avoided CO_2 forcing due to CO_2 sequestration by anthropogenic-Fe-caused NPP in the 1850-2010 period. $CO_{2Without\ anthropogenic,\ 2010}$ is the 2010 atmospheric CO_2 concentrations without the anthropogenic Fe deposition in the 1850-2010 period. $CO_{2with\ anthropogenic,\ 2010}$ is the actual present-day atmospheric CO_2 concentration (assumed to be 410 ppmv).

Table A.1. Sensitivity simulations performed in this work to estimate the anthropogenic Fe DRF.
$Clay_{DRF}$ = Case 2 – Case 1; $Oxide_{DRF}$ = Case 2; and $HighOxide_{DRF}$ = Case 3

Case	Emission species and value	Note
1	Anthropogenic Fe-clays and Fe-oxides	For estimating total anthropogenic DRF
2	Anthropogenic Fe-oxides	For isolating the Fe-oxide DRF from total anthropogenic DRF
3	Anthropogenic Fe-oxides high emissions magnitude values	For estimating the upper bound in Fe-oxide DRF

Table A.2. Sensitivity simulations performed in this work to estimate the anthropogenic Fe NPP. Row in red indicates the central simulation shown in Figure 1.

Case	Emission value (Rathod et al., 2020, temp-mineral case)	Phytoplankton C/SolubleFe ratio (g/g)	Fe limitation area Based on surface uM NO_3
1	Central	$3x10^4$	2
2	High	$3x10^4$	2
3	Central	$3x10^4$	4
4	High	$3x10^4$	4
5	Central	$3x10^4$	8
6	High	$3x10^4$	8
7	Central	$1.5x10^5$	2
8	High	$1.5x10^5$	2
9	Central	$1.5x10^5$	4
10	High	$1.5x10^5$	4
11	Central	$1.5x10^5$	8
12	High	$1.5x10^5$	8

Table A.3. Percent Fe by mass in kaolinite and illite clays. We used direct %Fe values where available. Where only %Fe2O3 was reported, %Fe was calculated by multiplying the %Fe2O3 value by 0.7.

Iron content in mineral (% by mass)

Mineral	Sample location	%Fe2O3	%Fe	Reference
		Kaolinite		
Kaolinite	Theoretical	0	0	(Jepson, 1988)
Kaolinite	Mexico	0.01	0.007	(Jepson, 1988)
Kaolinite	Keokuk geode	0.06	0.042	(Mestdagh et al., 1980)
Kaolinite	France	0.08	0.056	(Jepson, 1988)
Kaolinite	Keokuk geode	0.09	0.063	(Jepson, 1988)
Kaolinite	Australia	0.1	0.07	(Jepson, 1988)
Kaolinite	Brazil	0.12	0.084	(Jepson, 1988)
Kaolinite	France	0.15	0.105	(Jepson, 1988)
Kaolinite	Middle Georgia, USA	0.17	0.119	(Jepson, 1988)
Kaolinite	England	0.23	0.161	(Jepson, 1988)
Kaolinite	Georgia, USA	0.23	0.161	(Mestdagh et al., 1980)
Kaolinite	Australia	0.24	0.168	(Jepson, 1988)
Kaolinite	Georgia, USA	0.31	0.217	(Mestdagh et al., 1980)
Kaolinite	Brittany, France	0.32	0.224	(Mestdagh et al., 1980)
Kaolinite	St. Austell, UK	0.34	0.238	(Mestdagh et al., 1980)
Kaolinite	Middle Georgia, USA	0.38	0.266	(Jepson, 1988)
Kaolinite	Australia	0.45	0.315	(Singh & Gilkes, 1992)
Kaolinite	Spain	0.5	0.35	(Jepson, 1988)
Kaolinite	Charentes, France	0.5	0.35	(Mestdagh et al., 1980)
Kaolinite	Georgia, USA	0.51	0.357	(Mestdagh et al., 1980)
Kaolinite	Czechoslovakia	0.52	0.364	(Mestdagh et al., 1980)
Kaolinite	English coating grade	0.61	0.427	(Jepson, 1988)
Kaolinite	England	0.71	0.497	(Jepson, 1988)
Kaolinite	US Premium coating grade	0.75	0.525	(Jepson, 1988)
Kaolinite	English filter grade	0.8	0.56	(Jepson, 1988)
Kaolinite	Charentes, France	0.93	0.651	(Mestdagh et al., 1980)
Kaolinite	Charentes, France	0.95	0.665	(Mestdagh et al., 1980)
Kaolinite	Charentes, France	0.95	0.665	(Mestdagh et al., 1980)
Kaolinite	East Georgia	0.99	0.693	(Jepson, 1988)
Kaolinite	Middle Georgia, USA	1	0.7	(Jepson, 1988)
Kaolinite	Charentes, France	1	0.7	(Mestdagh et al., 1980)
Kaolinite	Georgia, USA	1.08	0.756	(Mestdagh et al., 1980)
Kaolinite	East Georgia	1.1	0.77	(Jepson, 1988)
Kaolinite	Charentes, France	1.17	0.819	(Mestdagh et al., 1980)
Kaolinite	Senegal	1.24	0.868	(Mestdagh et al., 1980)
Kaolinite	Charentes, France	1.33	0.931	(Mestdagh et al., 1980)

Kaolinite	Charentes, France	1.35	0.945	(Mestdagh et al., 1980)
Kaolinite	Cuba	1.52	1.064	(Mestdagh et al., 1980)
Kaolinite	Charentes, France	1.62	1.134	(Mestdagh et al., 1980)
Kaolinite	Zaire	1.68	1.176	(Mestdagh et al., 1980)
Kaolinite	Australia	1.7	1.19	(Jepson, 1988)
Kaolinite	Paris bassin, France	1.74	1.218	(Mestdagh et al., 1980)
Kaolinite	Nigeria	1.86	1.302	(Mestdagh et al., 1980)
Kaolinite	Paris bassin, France	1.89	1.323	(Mestdagh et al., 1980)
Kaolinite	Brazil	1.9	1.33	(Jepson, 1988)
Kaolinite	Rwanda	2.32	1.624	(Mestdagh et al., 1980)
Kaolinite	England	3.12	2.184	(Jepson, 1988)
Kaolinite	England	4.29	3.003	(Jepson, 1988)

Illite

Illite	Colorado, USA		0.88	(Murad & Wagner, 1994)
Illite	Regensburg, Germany		2.7	(Murad & Wagner, 1994)
Illite	API36 NY, USA		3.38	(Journet et al., 2008)
Illite	Illite No. 36	5.2	3.64	(Michael & McWhinnie, 1989)
Illite	Illite No. 35	4.99 + 0.26*	3.6932	(Ericsson et al., 1977)
Illite	Illite No. 36	4.99 + 0.26*	3.6932	(Ericsson et al., 1977)
Illite	API35 Illinois, USA	0	4.65	(Journet et al., 2008)
Illite	OECD#5, France		5.18	(Murad & Wagner, 1994)
Illite	ISGS, IL		6	(Dong et al., 2003)
Illite	Muloorina, Australia		8.41	(Johnston & Cardile, 1987)

*FeO, multiplier = 0.77

Table A.4. Mineral emission magnitudes for the 'base' case for DRF calculations

Class	Species	Fe-as-mineral emissions (Rathod et al., 2020) (Gg/yr)			Mineral emissions (Fe-as-mineral / %Fe by weight) (Gg/yr)	
		Fine (PM_1)	Coarse (PM_{1-10})	%Fe by weight (%)	Fine (PM_1)	Coarse (PM_{1-10})
Iron oxide	**Sulfates**	23	16	36.00	64	45
Iron oxide	**Hematite**	120	97	70.00	172	138
Iron oxide	**Magnetite**	863	769	72.30	1194	1064
Clay	**Illite**	80	171	4.60	1739	3722
Clay	**Kaolinite**	20	43	0.24	8333	17833

Table A.5. Simulated oceanic NPP by anthropogenic soluble iron deposition under different assumptions. High C/SolubleFe is 5x Cent C/SolubleFe. Low, Cent, and High Fe-limitation cut-off corresponding to ocean waters with surface nitrate concentrations of 2μM, 4μM, and 8μM, respectively. The row in red indicates the central simulation shown in Figure 1.

PD NPP (PgC/yr)					CO2-equivalent forcing for 2010 (W/m^2)			For the 1850-2000 period	
Case No.	**Deposition (kg/m2/s)**	**C/SolubleFe (g/g)**	**Fe-limited cut-off (μM NO3)**	**Global Anthropogenic-Fe NPP (Pg C/yr)**	**CO2 reduction per year (ppmv)**	**CO2 without anthroSolFe (ppmv)**	**CO2 forcing (W/m^2)**	**CO2 without anthrosolfe (ppmv)**	**CO2 forcing (W/m^2)**
1	Central	$3x10^4$	2	0.52	0.0122	410.0122	0.0002	410.5831	0.0076
2	Central	$3x10^4$	4	0.3	0.0071	410.0071	0.0001	410.3364	0.0044
3	Central	$3x10^4$	8	0.18	0.0042	410.0042	0.0001	410.2018	0.0026
4	Central	$1.5x10^5$	2	2.66	0.0626	410.0626	0.0008	412.9827	0.0388
5	Central	$1.5x10^5$	4	1.58	0.0372	410.0372	0.0005	411.7717	0.0231
6	Central	$1.5x10^5$	8	0.9	0.0212	410.0212	0.0003	411.0092	0.0132
7	High	$3x10^4$	2	2.32	0.0546	410.0546	0.0007	412.6015	0.0338
8	High	$3x10^4$	4	1.38	0.0325	410.0325	0.0004	411.5474	0.0202
9	High	$3x10^4$	8	0.74	0.0174	410.0174	0.0002	410.8298	0.0108
10	High	$1.5x10^5$	2	11.62	0.2735	410.2735	0.0036	423.0297	0.1674
11	High	$1.5x10^5$	4	6.92	0.1629	410.1629	0.0021	417.7595	0.1003
12	High	$1.5x10^5$	8	3.74	0.0880	410.0880	0.0011	414.1937	0.0544

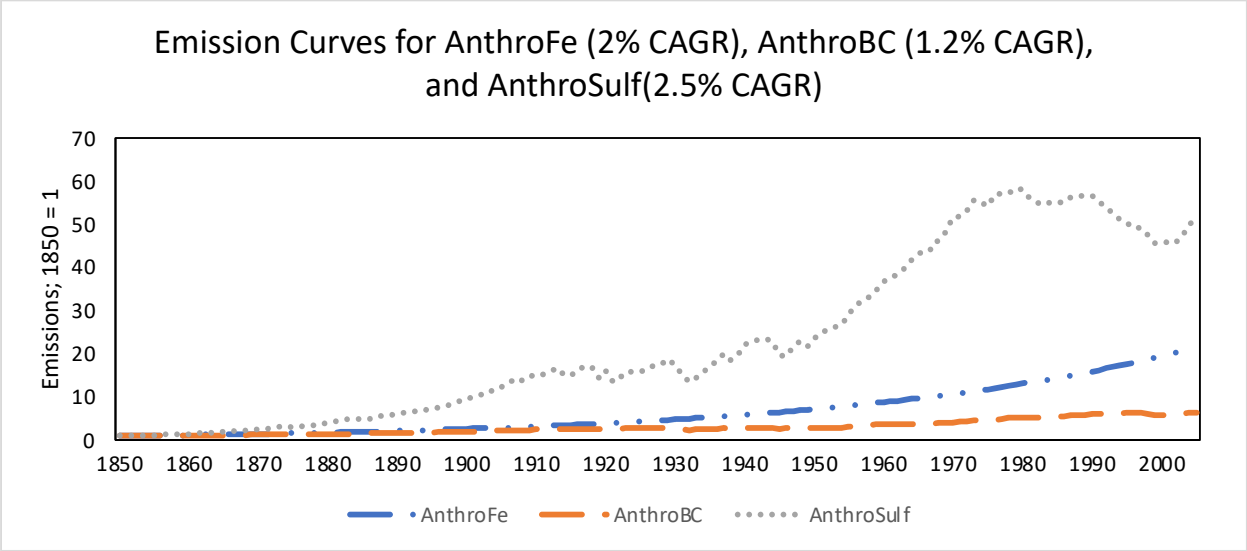

Figure A.1. Normalized emission time-series for Anthropogenic Fe, Black Carbon (BC), and Sulfur dioxide in the 1850-2000 period. CAGR = Compound Annual Growth Rate. AnthroFe is tracked back at 2% CAGR using 2010 values whereas BC and SO_2 data are from CEDS. All these sources represent non-biomass-related anthropogenic combustion emissions.

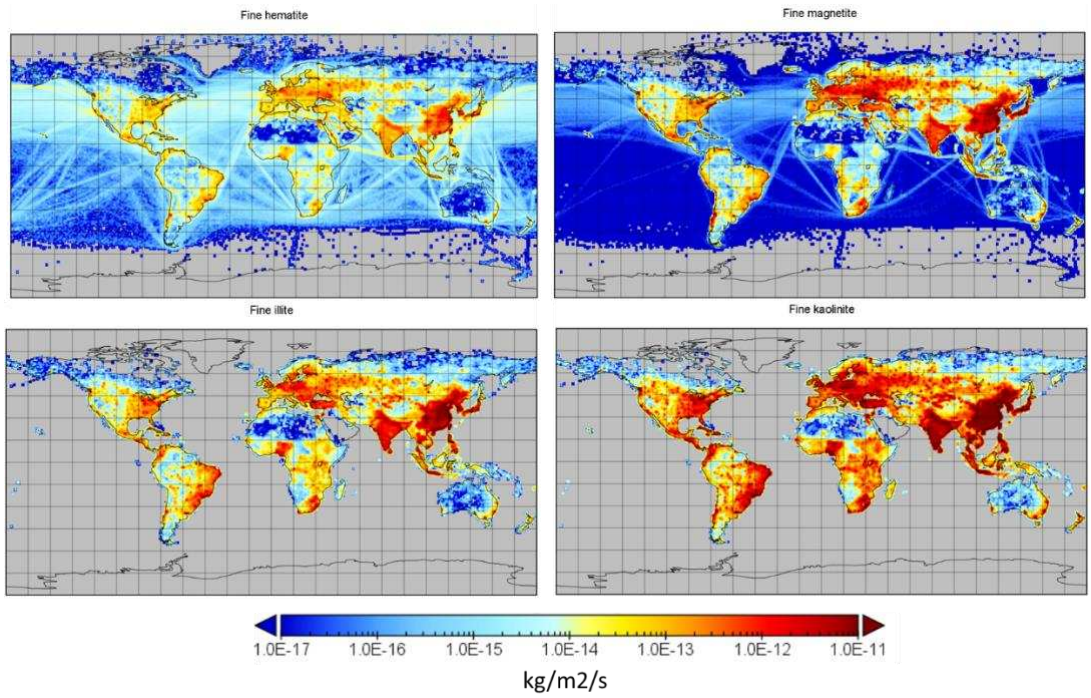

Figure A.2. Mineral emission maps for hematite, magnetite, kaolinite, and illite in the PM_1 size fraction. Emissions in the $PM_{1\text{-}10}$ (Coarse) fraction have similar spatial distribution as PM_1 emissions and are hence not shown.

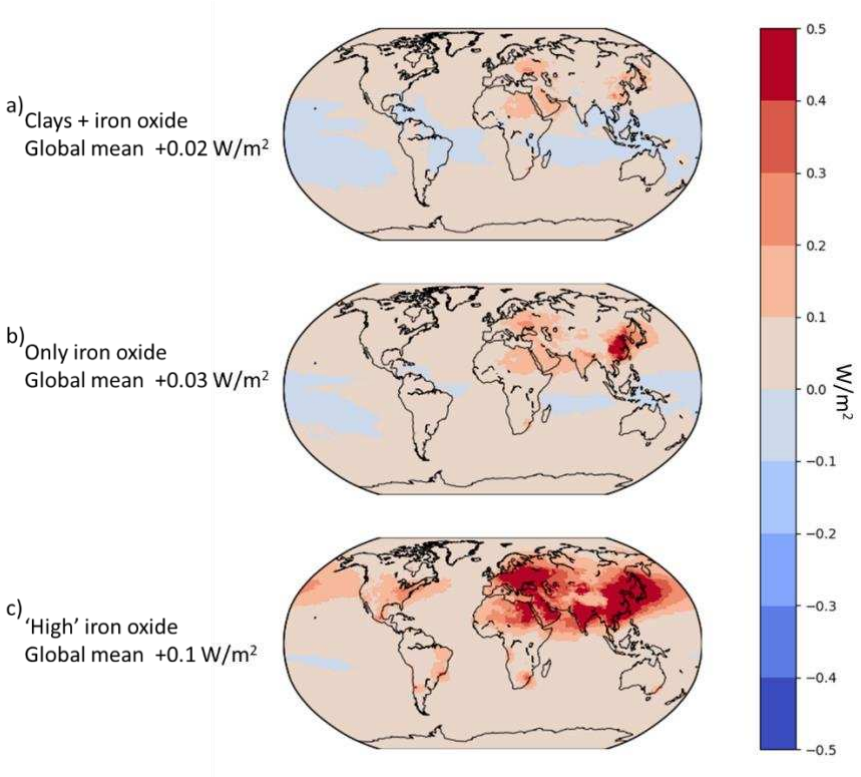

Figure A.3. 2010 DRF in W/m^2 by anthropogenic (a) clays and oxides ,+0.02 W/m^2, b) oxides only, +0.03 W/m^2, and c) high oxide emissions, +0.1 W/m^2. Values indicate the global mean.

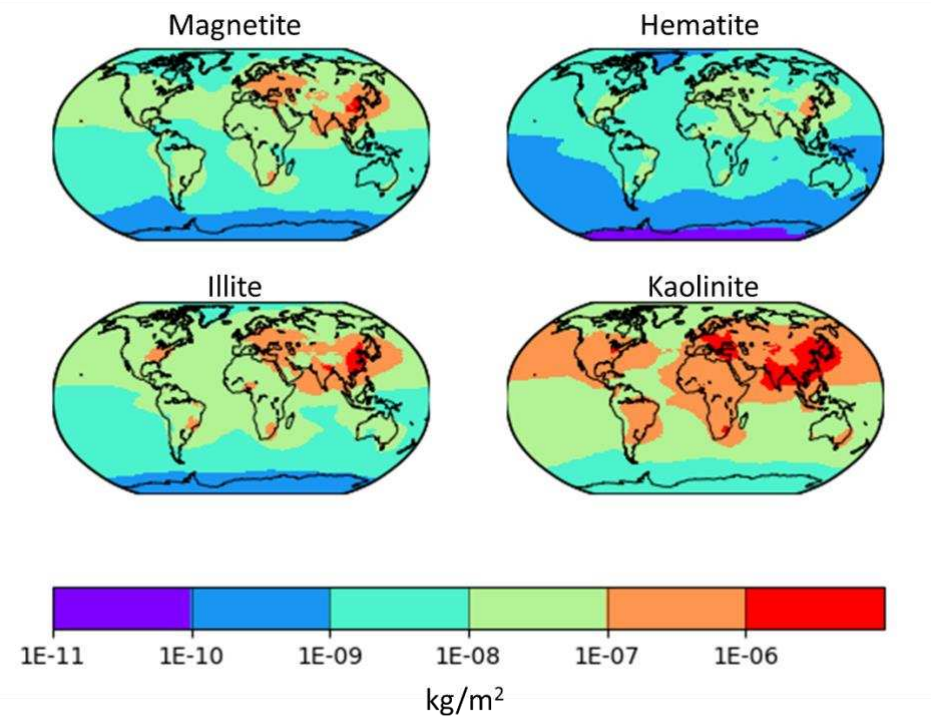

Figure A.4. Annual average column burden of magnetite, hematite, illite, and kaolinite, in kg/m^2.

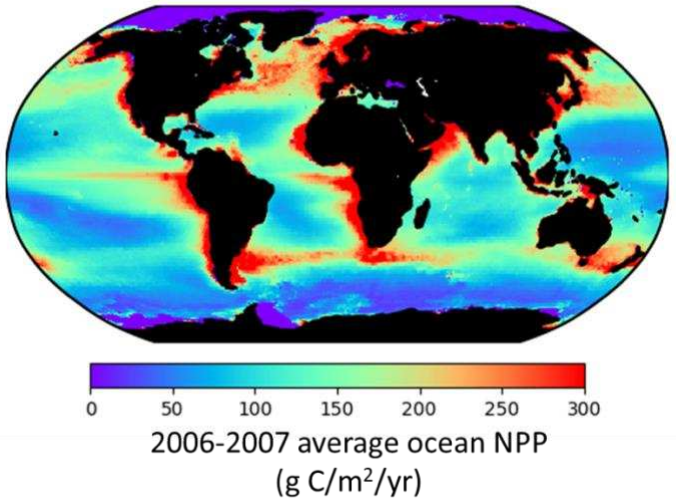

Figure A.5. 2006-2007 average ocean NPP in g C/m2/yr. Data from Behrenfeld and Falkowski, (2003); Available here: http://sites.science.oregonstate.edu/ocean.productivity/standard.product.php (last accessed April 4, 2022)

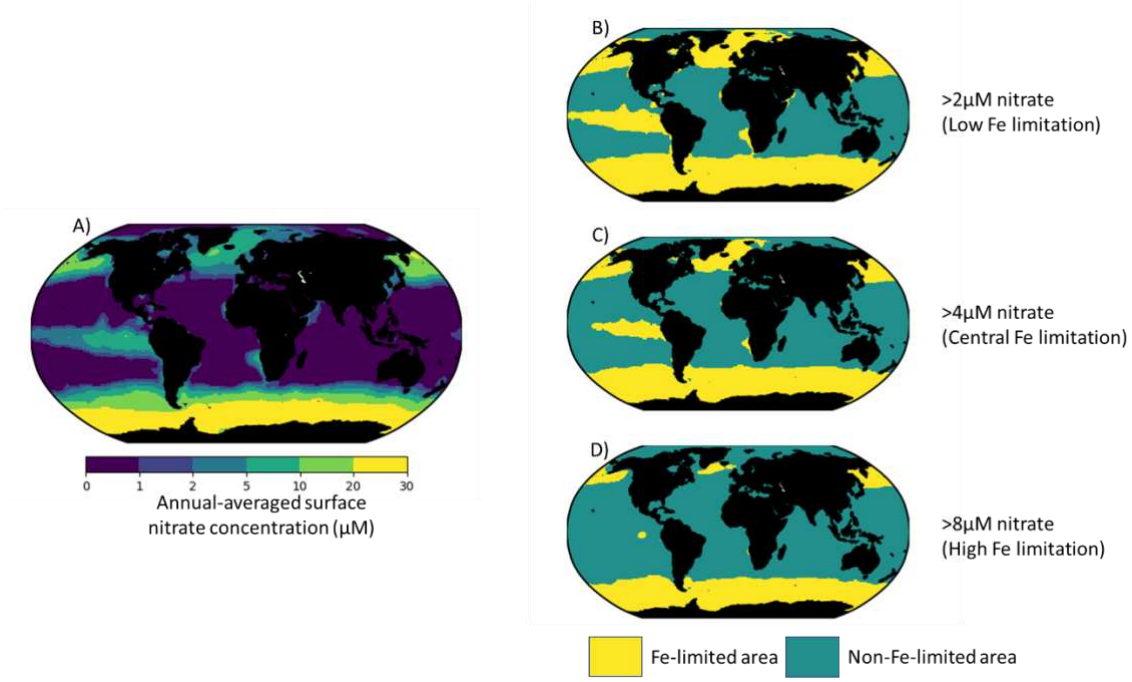

Figure A.6. Showing Fe limitation area based on surface nitrate abundance. Ocean waters are assumed to be iron-limited if the surface nitrate concentrations are more than 2, 4, and 8μM. Data from World Ocean Atlas, 2018 (Garcia et al., 2019). The Southern Ocean has more than 20μM surface nitrate, hence it is iron-limited in all three assumptions.

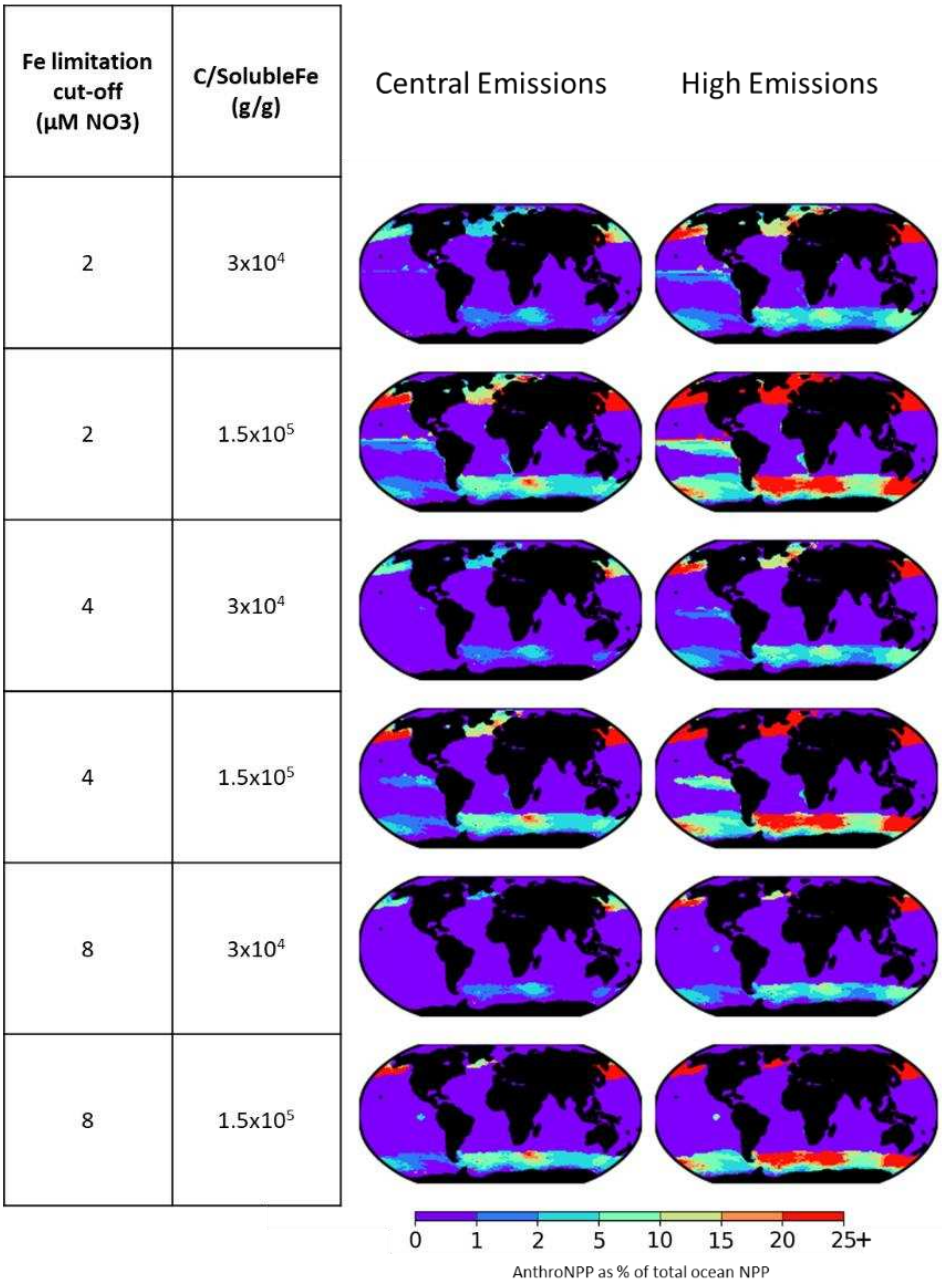

Figure A.7. Simulated Anthropogenic Fe-caused NPP in various sensitivity cases, shown as a percent of total ocean NPP.

APPENDIX B

SUPPLEMENTAL INFORMATION FOR CHAPTER 3

Text B.1: PMF assumptions and data curation

Selection and processing of observations

1. Elements used for the analysis are shown in Table B.3.
2. The bolded species were used for source apportionment in this study. These elements and molecules were chosen both to paint a clearer picture of source apportionment and to account for a large portion of total $PM_{2.5}$ mass.
3. The choice of chlorine vs. chloride and 3*sulfur vs. sulfate followed recommendations from the IMPROVE team as well as those in recently published work (e.g., Correal et al., 2020).
4. We included every site in CONUS that had continuous measurements from 2011 through 2019.
5. Zero or negative concentrations were set to a random number between zero and the MDL. The uncertainties of those concentrations were recalculated according to the IMPROVE SOP. We removed any data points that had one or more missing values for any of our selected components, either in concentration or uncertainty.
6. Elements with a very low signal-to-noise ratio, which are very rare and noisy species, were excluded from the PMF analysis. This was a recommendation from the EPA PMF 5.0 users' manual for species below 0.5 S/N (Norris and Duvall, 2014).

7. The other exception is excluding elements that would have otherwise been doubly counted, for example, sulfur and sulfate. Only one should be used: in this case, sulfate was chosen (personal communication, White and Hyslop).
8. Following the recommendation from a published IMPROVE advisory, we reduced the reported vanadium concentrations from January 2011 to October 2017 by 23% (http://vista.cira.colostate.edu/improve/Data/QA_QC/Advisory/da0038/da0038_V_advisory.pdf).
9. Total reported elemental and organic carbon concentrations did not have corresponding uncertainties in the database before 2017. Only the fractions themselves (EC1, EC2, EC3, OP, OC1, OC2, OC3, OC4) had uncertainties and minimum detection limits (MDL). The IMPROVE Standard Operating Procedure (SOP) had some of the information required to back out pre-2017 uncertainties (Hyslop and White, 2009; IMPROVE SOP #351, http://vista.cira.colostate.edu/improve/wp-content/uploads/2019/06/IMPROVE-SOP-351_Data-Processing-and-Validation_06.2019.pdf).
10. The first crucial component of PMF setup is to determine which variables are "weak" and "bad"; that is, which elements should have their uncertainties tripled or be excluded entirely, respectively. We consulted the EPA PMF 5.0 user's manual for this information (https://www.epa.gov/sites/production/files/2015-02/documents/pmf_5.0_user_guide.pdf). We set variables whose signal-to-noise ratio (S/N), calculated by the EPA PMF 5.0 software, was between 0.5 and 1.0 to "weak", and those less than 0.5 to "bad". Uncertainties were therefore tripled for Cr, Ni, and Se. As and Rb were ultimately removed entirely using this method, as noted in Table 2.1. Additionally, we set total $PM_{2.5}$ as a weak total variable, tripling its uncertainty as well.

11. Ultimately, this approach included 148 sites and yielded approximately 176,000 samples. The ME-2 engine can only calculate 100,000 samples at a time (Paatero, *personal communication*), so we split the data in half using the Python pandas "sample" method with random seed 125. Additionally, we created a separate bootstrapped version of our data with 8,000 samples and the same pandas method. This was used for the EPA PMF 5.0 software's uncertainty calculations and was necessary to accommodate its input limitations. The results of those uncertainty calculations were robust.

Table B.1 and B.2: COARSEMAP observations for $PM_{2.5}$-Fe and PM_{10}-Fe. Attached as csv.

Table B.3. IMPROVE species considered for source apportionment. **Bolded** species passed the QAQC tests and were used in the PMF analysis.

Aluminum	Arsenic	**Bromine**	**Calcium**	**Elemental Carbon**
Organic Carbon	**Chlorides**	Chlorine	**Chromium**	**Copper**
Iron	**Lead**	**Magnesium**	**Manganese**	**Total $PM_{2.5}$**
Total PM_{10}	Coarse mass	**Nickel**	**Nitrates**	Phosphorous
Potassium	Rubidium	**Selenium**	**Silicon**	**Sodium**
Sulfur	**Sulfate**	**Titanium**	**Vanadium**	**Zinc**

Table B.4. Metal/Fe ratio in PMF-derived factor and observations for Dust

Species	Dust-PMF	Saharan Dust-Obs
Al	1.496403	1.8
Ti	0.092446	0.18
Fe	1	1
V	0.001752	0.002
Ni	0.000687	0.0005
Mg	0	0.17
Ca	0.079137	0.37

Table B.5. Metal/Fe ratio in PMF-derived factor and observations for Heavy Fuel Oil combustion

	M/Fe ratio	
Species	**HFO-PMF**	**HFO-Obs**
Al	0	0.4
Ti	0.103704	0.05
Fe	1	1
V	0.035463	5
Ni	0.019444	1.5
Mg	7.37037	0.8
Ca	0	0.2

Table B.6. Metal/Fe ratio in PMF-derived factor and observations for Wood combustion

	M/Fe ratio	
Species	**Wood-PMF**	**Wood-Obs**
Al	0	3
Ti	0.096661	0
Fe	1	1
V	0	0
Ni	0.002226	0
Mg	0	3
Ca	1.500795	10

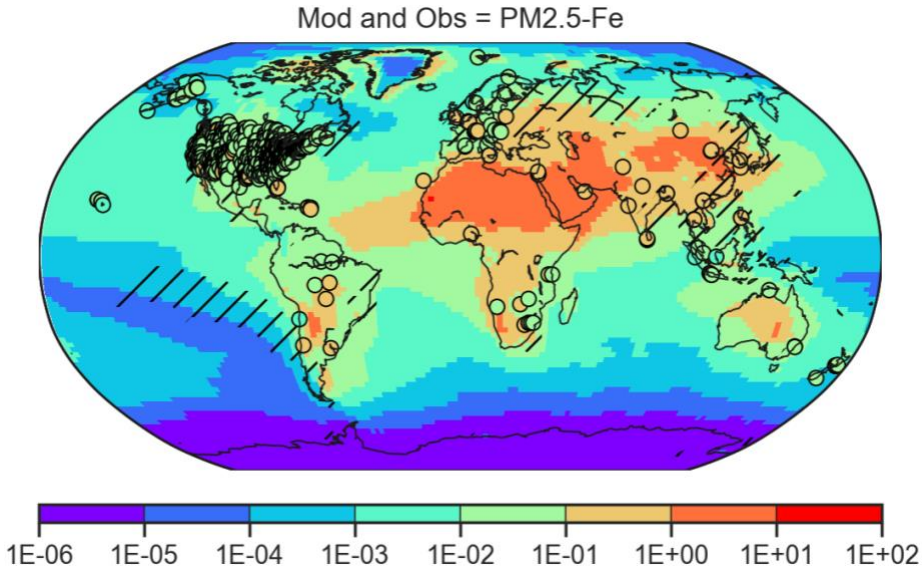

Figure B.1. $PM_{2.5}$-Fe COARSEMAP observations and modeled concentrations. Hatches show where the anthropogenic source is the largest modeled contributor to atmospheric total iron concentration.

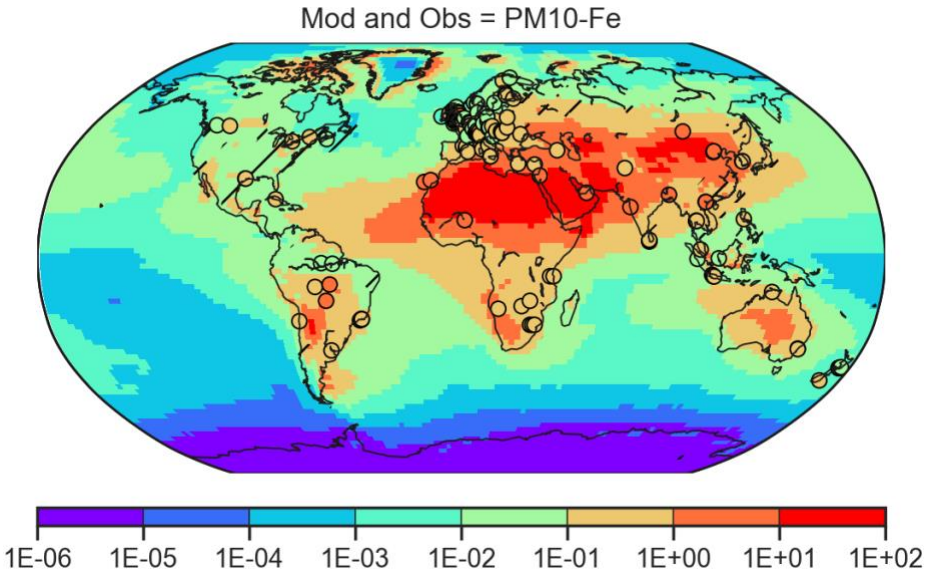

Figure B.2. PM_{10}-Fe COARSEMAP observations and modeled concentrations. Hatches show where the anthropogenic source is the largest modeled contributor to atmospheric total iron concentration.

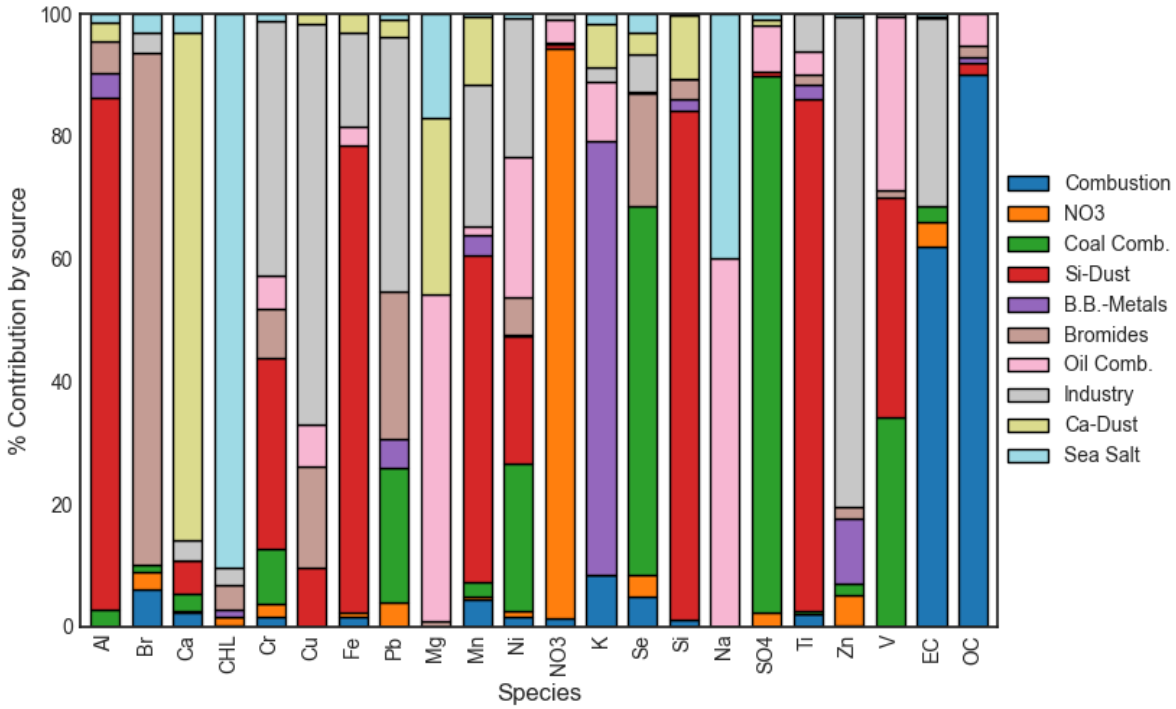

Figure B.3. Factor Fingerprints, 10 factors: For each of the 23 variables, 22 of which nearly sum up to a total $PM_{2.5}$, this plot shows the percentage of each element associated with each factor. Y-axis shows the average percent contribution by a source to a receptor in the IMPROVE sites.

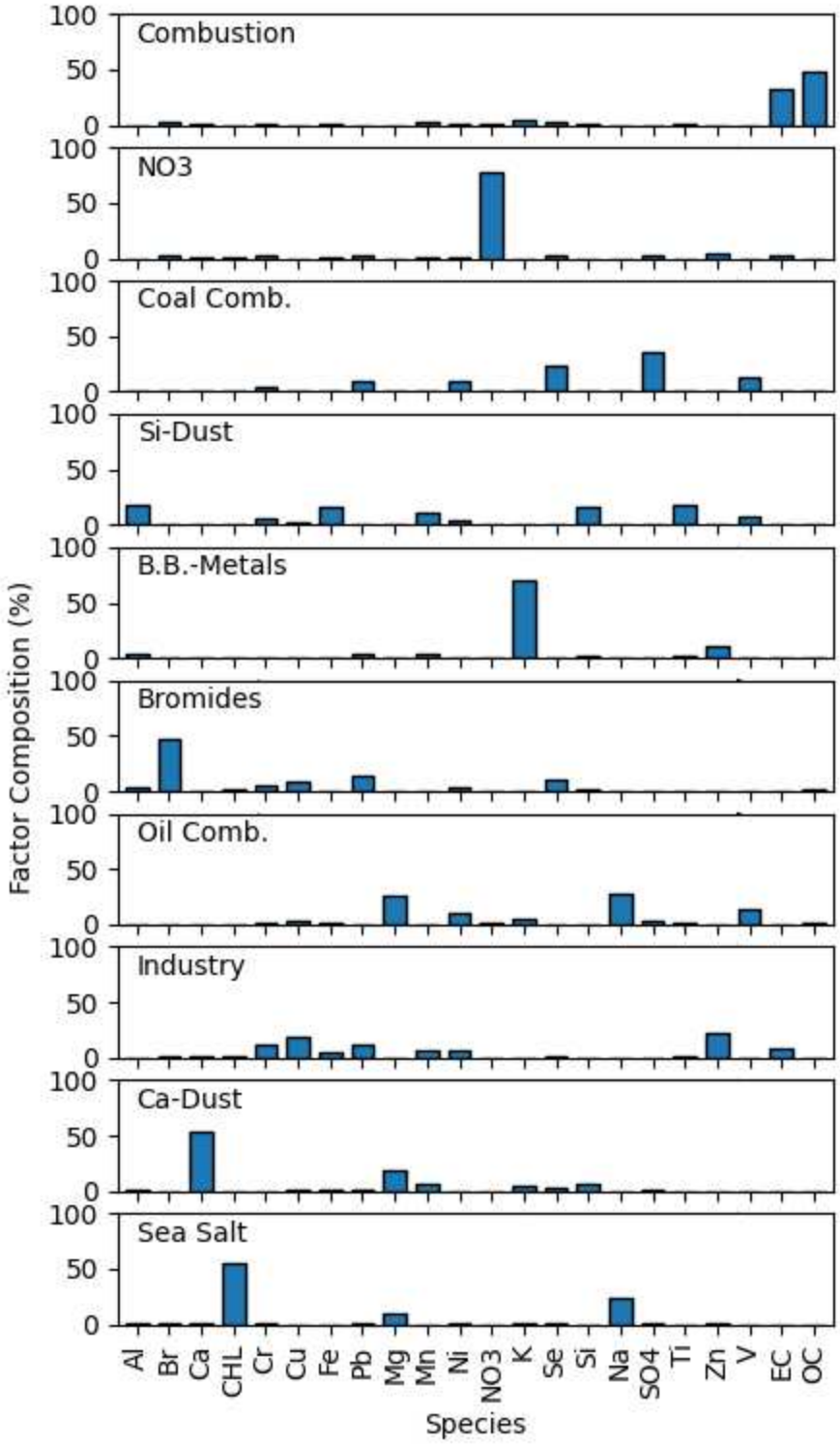

Figure B.4. Composition of the 10 factors obtained using PMF on US-IMPROVE observations.

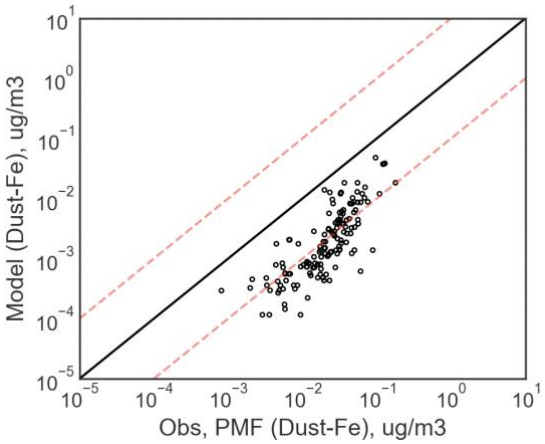

Figure B.5. Model (CESM-CAM6) and observation (PMF Dust-Fe) comparison for dust-Fe in the USA IMPROVE observations.

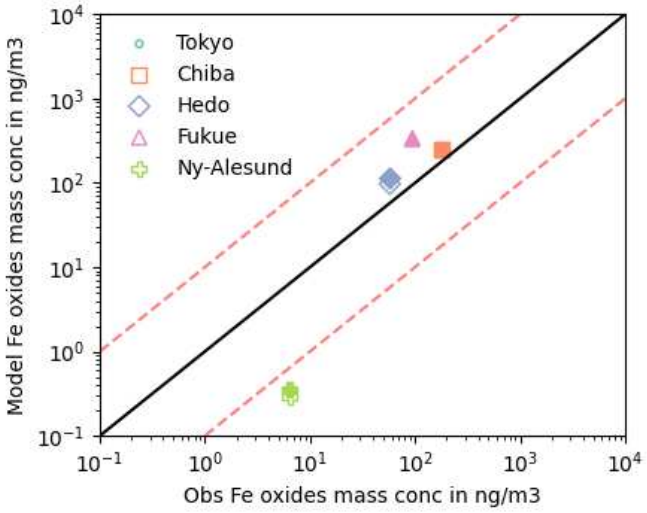

Figure B.6. Magnetite observation and model comparison with (filled) and without (hollow) dust-iron oxides.

APPENDIX C

SUPPLEMENTAL INFORMATION FOR CHAPTER 4

Text C.1

This text describes the methodology for estimating the global metal demand, mapping the metal demand to regional metal production in various technologies, and then estimating emissions using a GAINS methodology.

Equation C.1: Estimating global metal demand

$$MD_{m,i,t,s} = \sum_{r=1}^{n} \Delta RAC_{i,t,r,s} * MI_{m,t} \textbf{ (C.1)}$$

Intermediate step: Mapping metal m to GAINS sector gs (how a metal production sector is represented in GAINS)

1. Steel: Basic Oxygen Furnace, Electric Arc Furnace, Open Hearth Furnace
2. Aluminum: Primary and Secondary smelting
3. Non-Fe, Non-Al ('NFME'): single sector representing all non-ferrous, non-aluminum metals
4. Mining: single sector representing all-metal ore mining

Equation C.2: Mapping metal demand to the producing region

Metal activity in region r in GAINS sector gs = Global metal demand * Fraction of all-use metal m produced in region r in GAINS sector gs

$$MC_{m,i,t,r,s,gs} = MD_{m,i,t,s} * \frac{MIEA_{m,i,t,s,gs,r}}{MIEA_{m,i,t,s,gs}} \textbf{ (C.2)}$$

Equation C.3: Emissions

$$E_{m,i,t,r,s} = MC_{mi,t,r,s,gs} * EF_{i,gs,r} * (1 - ABAT_{i,gs,r}) \textbf{ (C.3)}$$

Equation C.4 for Local Production case: Mapping of metal demand to GAINS sectors

$$MC_{m,i,t,r,s,gs} = MD_{m,i,t,r,s} * \frac{MIEA_{m,i,t,s,gs,r}}{MIEA_{m,i,t,s,r}}$$

Where

m = metal,

i = year,

t = technology,

r = region,

s = scenario,

ΔRAC = The difference between projected gross electrical capacity (GW/yr) in two years, divided by the period between those years. As projected gross electrical capacity (GW) in any year is the stock of that technology, expressed as the sum of existing capacity, ΔRAC hence includes the changes to both capacity additions and retirements (IEA, 2020).

MI = metal intensity of renewable energy technologies (e.g. ton metal / GW solar addition),

MD = metal demand (ton / yr),

MC = GAINS metal activity (ton / yr),

c = country c in a region r

MIEA = metal activity in IEA all-use projections (ton /yr),

gs = GAINS sector (Basic Oxygen Furnace, Electric Arc Furnace, etc),

E = emissions (Gg/yr),

EF = Emission Factor (Gg $PM_{2.5}$ / ton activity),

ABAT = efficiency of control measures (dimensionless; $PM_{2.5}$ out / $PM_{2.5}$ in).

Text C.2. Downscaling routine

This text describes the downscaling routine for IEA 26 regions to GAINS 180 regions for capacity addition data for solar PV and wind turbines.

GAINS has a downscaling routine to convert IEA energy generation by technology from its 26 regions to 180 GAINS regions (Rafaj et al. 2018). However, the capacity addition of solar PV and wind turbines is not represented using that routine. Here we estimate capacity addition (e.g. GW of Solar PV) from energy generation (e.g. kWh) from IEA 26 regions to GAINS 180 regions using equation C.1.

$$\Delta CADD_{r,t} = \Delta CADD_{s,t} \frac{\Delta EADD_{r,t}}{\sum \Delta EADD_{r,t}} \textbf{(C.4)}$$

Where CADD is the estimated capacity addition in the GAINS region r in year t; EADD is the difference in energy generation between two time periods in GAINS region r in year t, and s is the IEA region to the GAINS region r belongs to.

For example, assume one IEA region, Asia, is made of two GAINS regions (India and China). Then, in a given year, the capacity addition of solar PV in India is assumed to be proportional to the fraction of Asia's solar energy added in India.

Table C.1. Metal intensities used in this work for solar PV (total plant values), wind turbines (total plant values), and Electric Vehicles (EV), from Watari et al., (2019)

Categories assumed in GAINS: **Red = Aluminum**, **Blue = Iron and steel**, and rest = NFME

Metal	Metal	Solar (ton / GW)	Wind (ton / GW)	EV (ton / vehicle)
Al	**Aluminum**	**33500**	**1372**	**0.127302**
Bo	Boron	0	1	0
Cd	Cadmium	0	0	0
Ce	Cerium	0	0	0
Cr	Chromium	1880	683	0.01185
Co	Cobalt	0	0	0.01346
Cu	Copper	3765	2497	0.0925
Dy	Dysprosium	0	16	0.000279
Er	Erbium	0	0	0
Gd	Gadolinium	0	0	0
Ga	Gallium	0	0	0
Ge	Germanium	0	0	0
In	Indium	0	0	0
Fe	**Iron (includes Steel)**	**1200000**	**119985**	**0.9095**
La	Lanthanum	0	0	0
Pb	Lead	39	0	0.00031
Li	Lithium	0	0	0.006768
Mg	Magnesium	0	0	0.0002
Mn	Manganese	0	57	0.03605
Mo	Molybdenum	200	335	0
Nd	Neodymium	0	148	0.000969
Ni	Nickel	1800	427	0.034589
Nb	Niobium	0	38	0
Pt	Platinum	0	0	0
Pr	Praseodymium	0	3	0.000001
Se	Selenium	0	0	0
Si	Silicon	6428	0	0
Ag	Silver	30	0	0
Te	Tellurium	0	0	0
Tb	Terbium	0	1	0
Sn	Tin	332	90	0
V	Vanadium	2	90	0
Zn	Zinc	1400	5450	0.0001

Table C.2. Fleet composition in the Rapid Decarbonization case (in thousands). Data from IEA (2020)

EV Sector	**2020**	**2025**	**2030**	**2035**	**2040**	**2045**	**2050**
Railways	113	141	168	202	244	285	329
Buses	595	1827	4187	7179	10561	13262	16105
Heavy duty vehicles	16	358	3483	7760	12183	17723	23416
Mopeds	258930	376284	562695	782188	968794	1065648	1117312
Cars	7042	46811	145072	330814	609841	918029	1206166
Light duty vehicles	353	3926	15360	34609	61282	82526	107346
Motorcycles	0	26	179	999	3823	6847	11126

Table C.3. Shows the absolute demand and percent of all-use for steel, aluminum, and non-ferrous non-aluminum for Current Energy Policies and Rapid Decarbonization pathways. All units in Million tons per year finished metal unless noted otherwise.

Steel

Current Energy Policies

	Metal demand (Million tons)			Total	Total as percent of all-use production
Year	**Solar**	**Wind**	**EV**		
2020	116.2	6.3	48.4	170.9	8.8
2025	146.5	7.1	25.2	178.8	8.3
2030	168.0	7.7	33.6	209.3	9.1
2035	186.8	8.0	41.4	236.3	9.7
2040	205.4	6.7	38.6	250.7	9.8
2045	209.5	7.0	34.6	251.2	9.4
2050	198.5	7.4	27.8	233.7	8.5

Rapid Decarbonization

	Metal demand (Million tons)			Total	Total as percent of all-use production
Year	**Solar**	**Wind**	**EV**		
2020	119.0	6.8	48.4	174.2	8.9
2025	255.4	12.3	29.5	297.2	13.2
2030	330.1	15.0	54.9	400.0	16.4
2035	342.2	15.2	78.7	436.0	17.3
2040	325.1	14.0	94.3	433.4	16.9
2045	273.1	12.4	85.8	371.3	14.6
2050	205.7	9.2	75.5	290.4	11.6

Aluminum

Current Energy Policies

	Metal demand (Million tons)			Total	Total as percent of all-use production
Year	**Solar**	**Wind**	**EV**		
2020	3.2	0.1	6.4	9.7	7.0
2025	4.1	0.1	3.3	7.5	4.9
2030	4.7	0.1	4.4	9.2	5.5
2035	5.2	0.1	5.5	10.8	5.8
2040	5.7	0.1	5.1	10.9	5.5
2045	5.8	0.1	4.6	10.5	5.0
2050	5.5	0.1	3.7	9.3	4.3

Rapid Decarbonization

Metal demand (Million tons)			Total	Total as percent of all-use production

Year	Solar	Wind	EV		
2020	3.3	0.1	6.4	9.8	7.0
2025	7.1	0.1	3.9	11.2	7.4
2030	9.2	0.2	7.2	16.6	10.2
2035	9.6	0.2	10.4	20.1	11.6
2040	9.1	0.2	12.4	21.7	12.0
2045	7.6	0.1	11.3	19.1	10.4
2050	5.7	0.1	10.0	15.8	8.7

NFME

Current Energy Policies

	Metal demand (Million tons)			Total	Total as percent of all-use production
Year	**Solar**	**Wind**	**EV**		
2020	1.5	0.5	10.1	12.2	16.6
2025	1.9	0.6	5.3	7.8	10.7
2030	2.2	0.6	7.0	9.9	13.1
2035	2.5	0.7	8.7	11.8	15.2
2040	2.7	0.6	8.1	11.3	14.8
2045	2.8	0.6	7.2	10.6	12.9
2050	2.6	0.6	5.8	9.0	10.6

Rapid Decarbonization

	Metal demand (Million tons)			Total	Total as percent of all-use production
Year	**Solar**	**Wind**	**EV**		
2020	1.6	0.6	10.1	12.2	16.7
2025	3.4	1.0	6.2	10.6	13.9
2030	4.4	1.2	11.5	17.1	20.6
2035	4.5	1.2	16.4	22.2	25.4
2040	4.3	1.2	19.7	25.1	28.0
2045	3.6	1.0	17.9	22.6	24.0
2050	2.7	0.8	15.8	19.2	20.1

Table C.4. Distribution Index (similar to Gini Index) values for the sum of all metals across all technologies for the two decarbonization scenarios under two abatement pathways and two production regionalities. CP corresponds to Current Energy Policies.

	Global Market Regionality	
	Current Abatement Legislation	
	Decarbonization Pathway	
	CP	**Rapid Decarbonization**
2025	0.59	0.56
2030	0.54	0.57
2035	0.50	0.57
2040	0.46	0.55
2045	0.47	0.53
2050	0.54	0.54

	Local Production Regionality	
	Current Abatement Legislation	
	Decarbonization Pathway	
	CP	**Rapid Decarbonization**
2025	0.56	0.59
2030	0.53	0.56
2035	0.48	0.53
2040	0.46	0.51
2045	0.46	0.48
2050	0.49	0.43

	Stringent Mitigation	
	Decarbonization Pathway	
	CP	**Rapid Decarbonization**
2025	0.56	0.54
2030	0.47	0.51
2035	0.36	0.45
2040	0.42	0.36
2045	0.40	0.37
2050	0.36	0.47

	Stringent Mitigation	
	Decarbonization Pathway	
	CP	**Rapid Decarbonization**
2025	0.56	0.59
2030	0.55	0.58
2035	0.54	0.58
2040	0.64	0.68
2045	0.66	0.68
2050	0.70	0.67

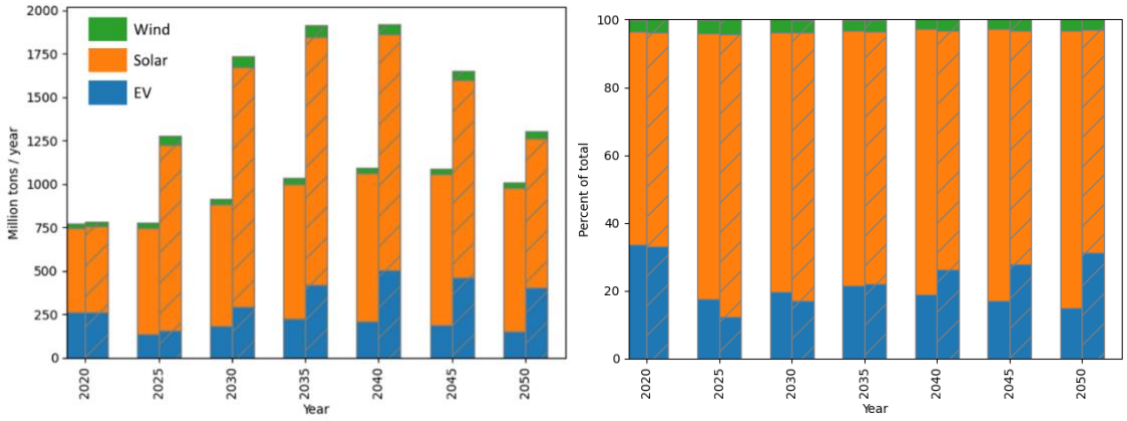

Figure C.1. a) Metal demand, in million tons per year, by EVs, solar PVs, and Wind energy addition in Current Energy Policies (left sub-bars), and Rapid Decarbonization (right sub-bars, hatched); b) Same as (a) but percent of total.

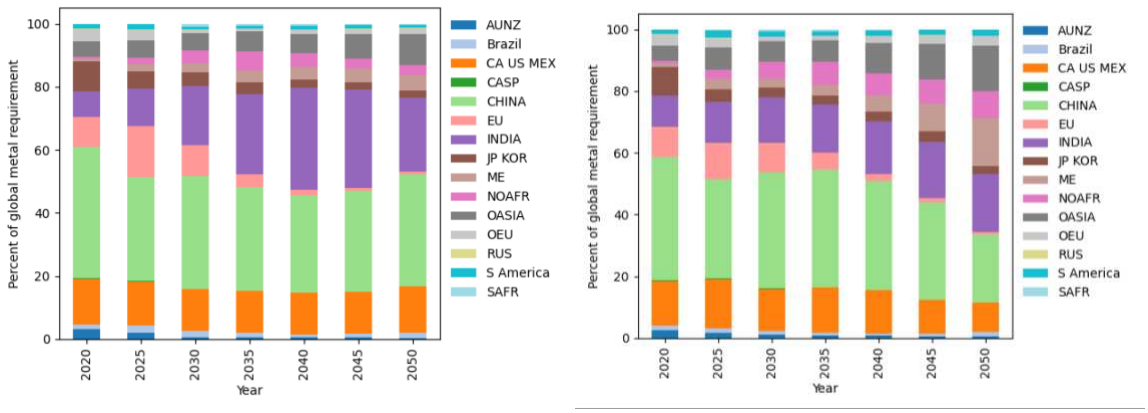

Figure C.2. Current and projected change in regional shares of metal demand in the Current Energy Policies (left) and Rapid Decarbonization (right) scenarios for Solar PVs.

Labels

1. AUNZ = Australia/New Zealand
2. CA US MEX = Canada, USA, Mexico
3. CASP = Central Asia
4. EU = European Union
5. JP KOR = Japan and Korea
6. ME = Middle East
7. NOAFR = North Africa
8. OASIA = Other Asia
9. OEU = Other Europe
10. RUS = Russia
11. S America = South America
12. SAFR = South Africa

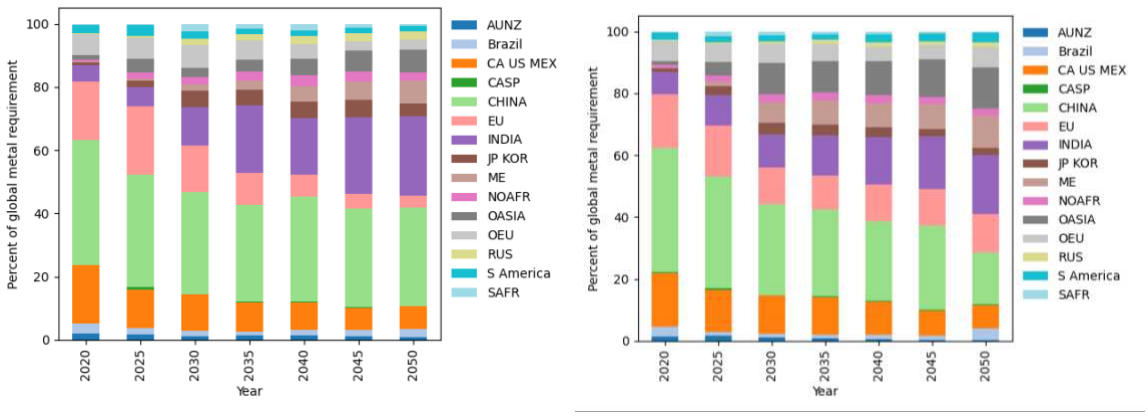

Figure C.3. Current and projected change in regional shares of metal demand in the Current Energy Policies (left) and Rapid Decarbonization (right) scenarios for Wind turbines.

Labels

1. AUNZ = Australia/New Zealand
2. CA US MEX = Canada, USA, Mexico
3. CASP = Central Asia
4. EU = European Union
5. JP KOR = Japan and Korea
6. ME = Middle East
7. NOAFR = North Africa
8. OASIA = Other Asia
9. OEU = Other Europe
10. RUS = Russia
11. S America = South America
12. SAFR = South Africa

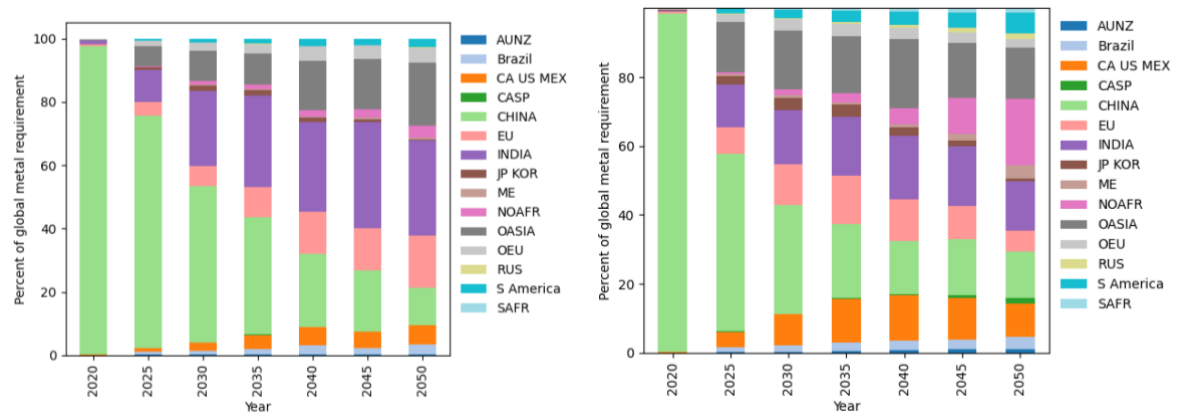

Figure C.4. Current and projected change in regional shares of metal demand in the Current Energy Policies (left) and Rapid Decarbonization (right) scenarios for Electric vehicles.

Labels

1. AUNZ = Australia/New Zealand
2. CA US MEX = Canada, USA, Mexico
3. CASP = Central Asia
4. EU = European Union
5. JP KOR = Japan and Korea
6. ME = Middle East
7. NOAFR = North Africa
8. OASIA = Other Asia
9. OEU = Other Europe
10. RUS = Russia
11. S America = South America
12. SAFR = South Africa

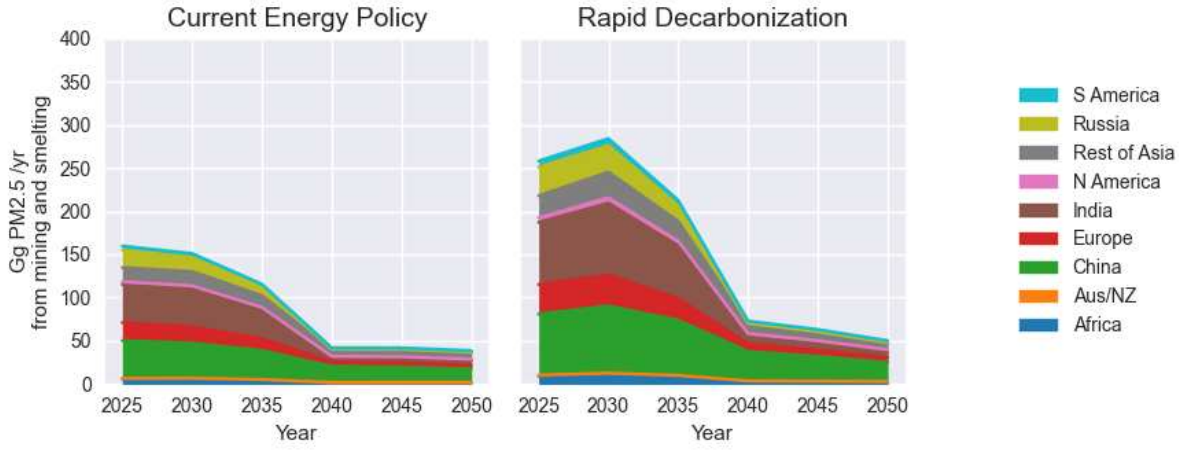

Figure C.5. $PM_{2.5}$ emissions from metal mining and smelting toward making renewable energy devices in Current Energy Policies (a) and Rapid Decarbonization (b) scenarios by region with Stringent Mitigation policies.

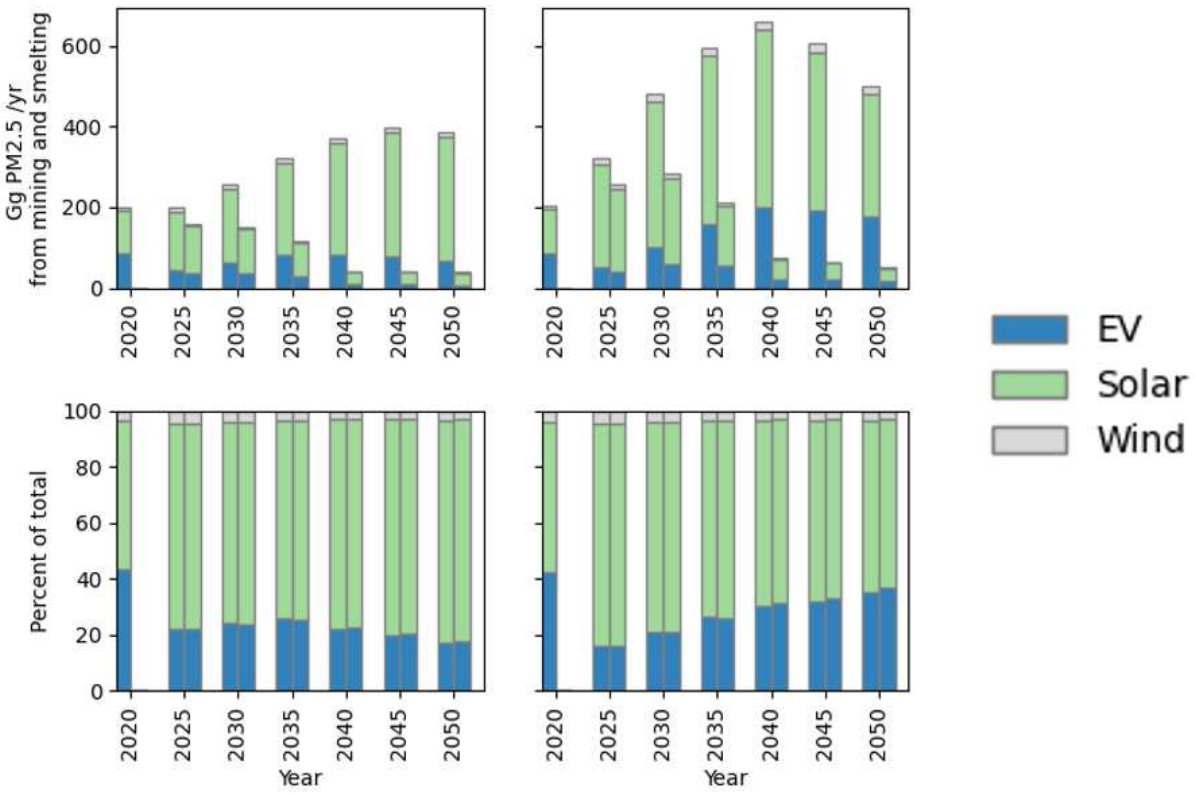

Figure C.6. Absolute (top) and relative (bottom) $PM_{2.5}$ emissions from metal mining and smelting toward making renewable energy devices in Current Energy Policies (left) and Rapid Decarbonization (right) scenarios by technology. Left- and right sub-bars in each subplot show the Current Abatement Legislation (Current Abatement Legislation, Current Energy Policies abatement), and Stringent Mitigation (stronger abatement) abatement policies, respectively. Stringent Mitigation and Current Abatement Legislation are same for 2020.

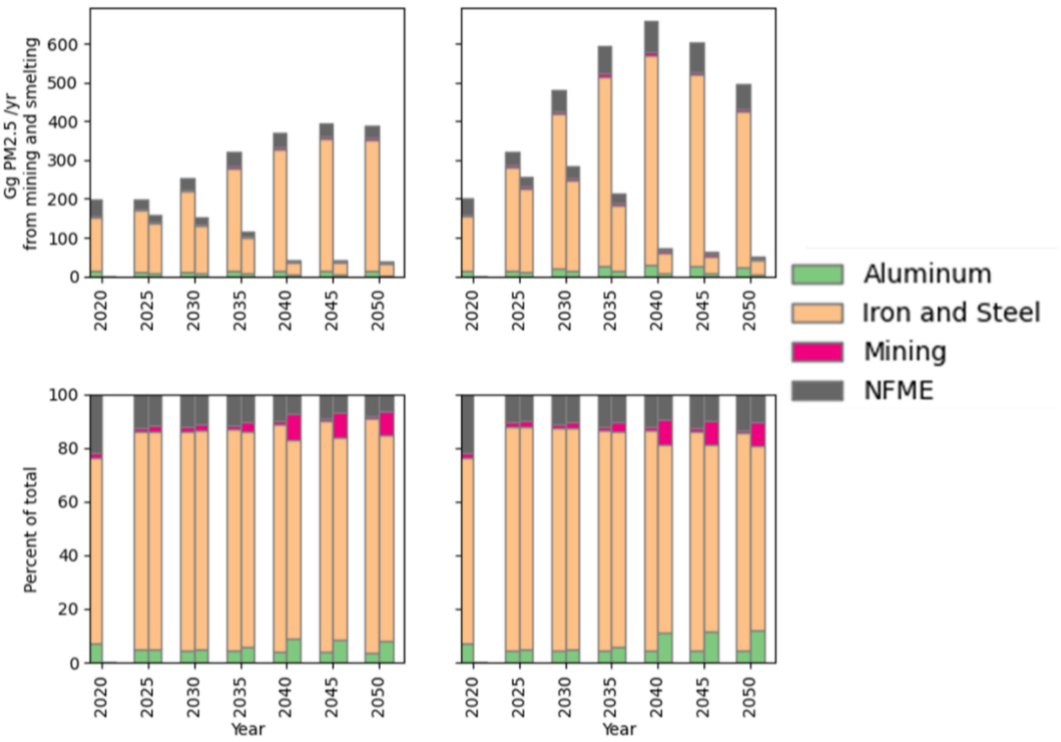

Figure C.7. Absolute (top) and relative (bottom) $PM_{2.5}$ emissions from metal mining and smelting toward making renewable energy devices in Current Energy Policies (left) and Rapid Decarbonization (right) scenarios by metal and process. Left- and right sub-bars in each subplot show the Current Abatement Legislation (Current Abatement Legislation, Current Energy Policies abatement), and Stringent Mitigation (stronger abatement) abatement policies, respectively. Stringent Mitigation and Current Abatement Legislation are same for 2020.

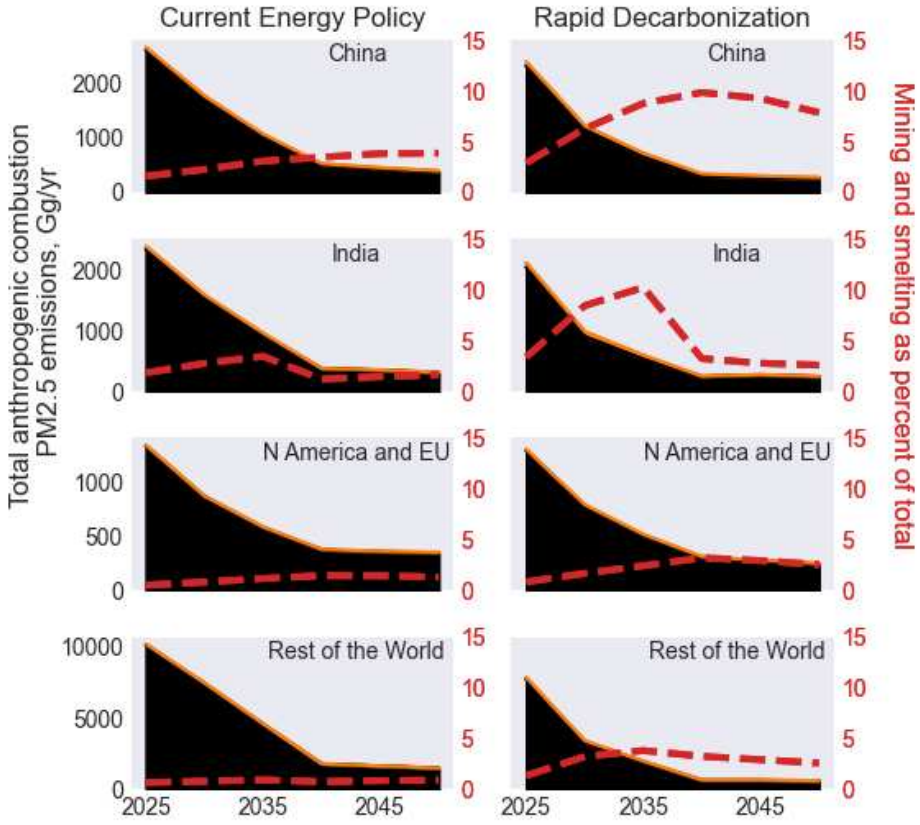

Figure C.8. Absolute primary $PM_{2.5}$ emissions from anthropogenic combustion (black) and mining and smelting for metals for renewable technologies (orange) shown for the Current Energy Policy and Rapid Decarbonization scenarios for India, China, North America and European Union, and Rest of the World for the Strictest Abatement case. $PM_{2.5}$ emissions by mining and smelting to meet metal demand for renewables, shown as percent of total (mining and smelting and fossil fuel combustion) (red line, right axis).

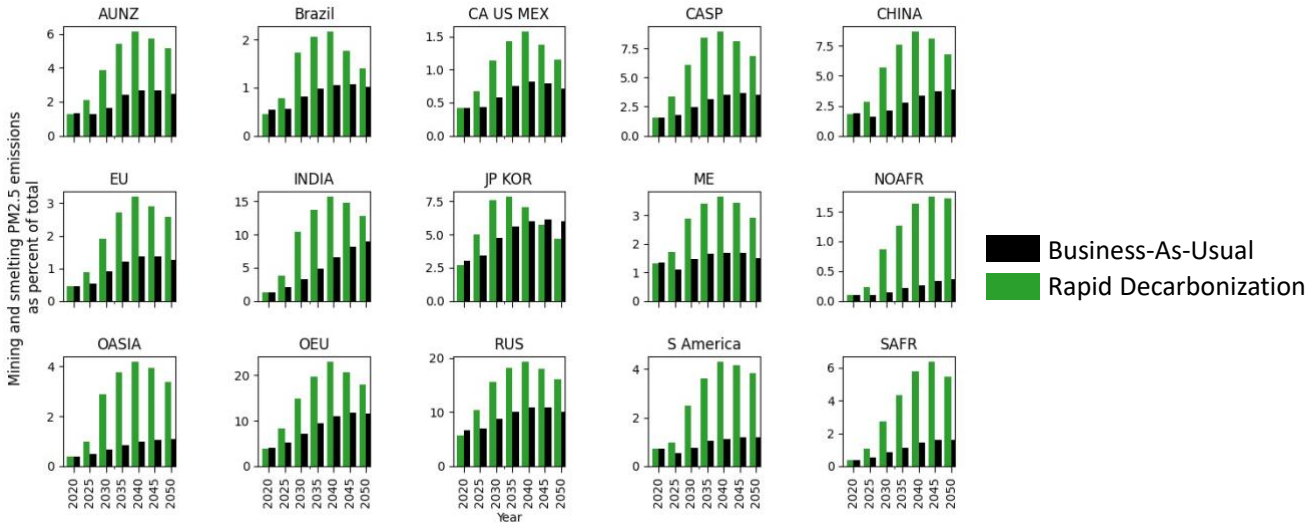

Figure C.9. $PM_{2.5}$ emissions by mining and smelting to meet metal demand for renewables, shown as percent of total (mining and smelting and fossil fuel combustion) in the Current Energy Policies and Rapid Decarbonization scenarios for Current Abatement Legislation.

Labels

1. AUNZ = Australia/New Zealand
2. CA US MEX = Canada, USA, Mexico
3. CASP = Central Asia
4. EU = European Union
5. JP KOR = Japan and Korea
6. ME = Middle East
7. NOAFR = North Africa
8. OASIA = Other Asia
9. OEU = Other Europe
10. RUS = Russia
11. S America = South America
12. SAFR = South Africa

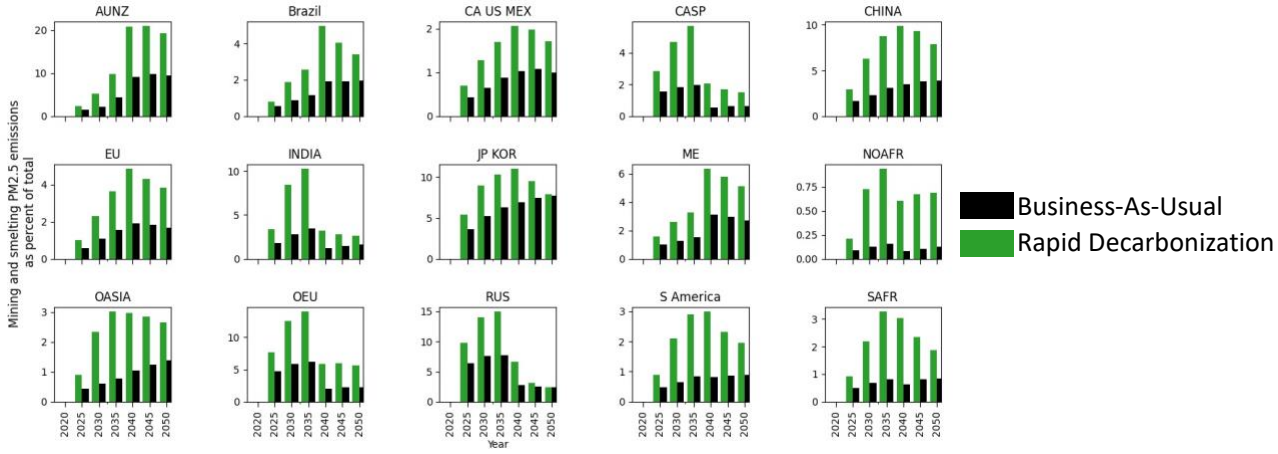

Figure C.10. $PM_{2.5}$ emissions by mining and smelting to meet metal demand for renewables, shown as percent of total (mining and smelting and fossil fuel combustion) in the Current Energy Policies and Rapid Decarbonization scenarios for Stringent Mitigation.

Labels

1. AUNZ = Australia/New Zealand
2. CA US MEX = Canada, USA, Mexico
3. CASP = Central Asia
4. EU = European Union
5. JP KOR = Japan and Korea
6. ME = Middle East
7. NOAFR = North Africa
8. OASIA = Other Asia
9. OEU = Other Europe
10. RUS = Russia
11. S America = South America
12. SAFR = South Africa

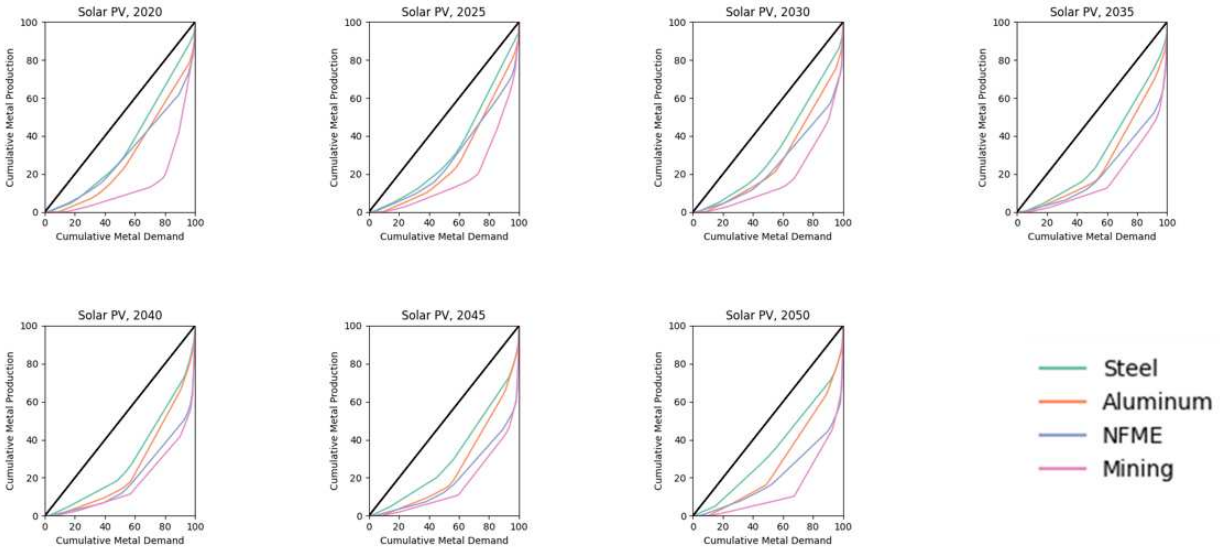

Figure C.11. Global distribution of demand and supply of by metals in the Current Energy Policies scenarios for the years 2020-2050 for the Solar PV.

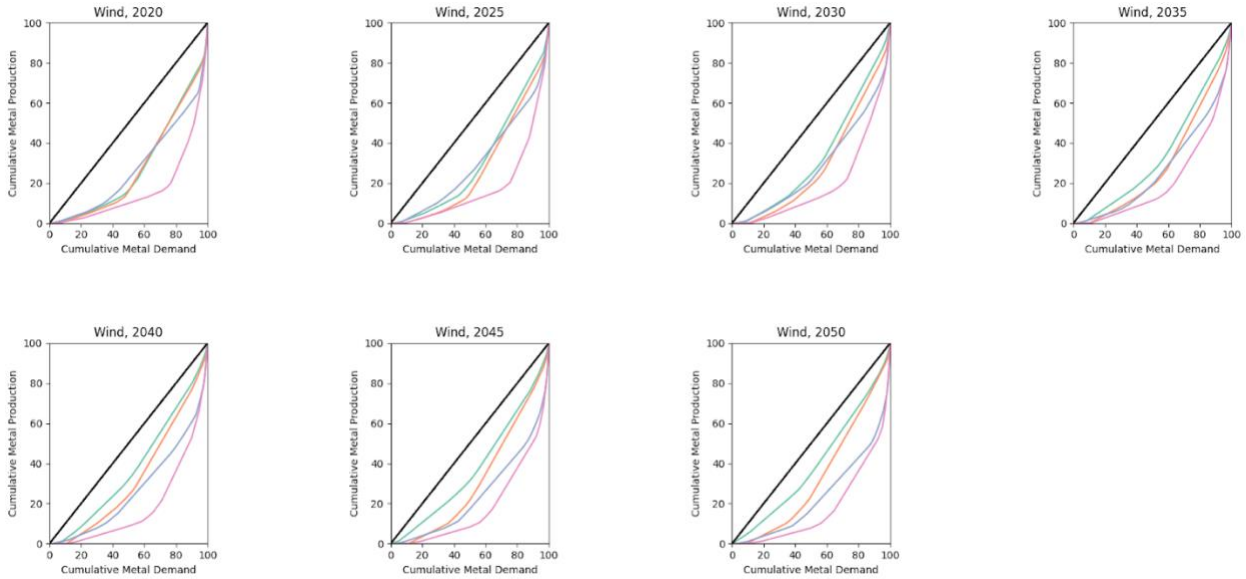

Figure C.12. Global distribution of demand and supply of by metals in the Current Energy Policies scenarios for the years 2020-2050 for the Wind turbines. Colors same as C.11

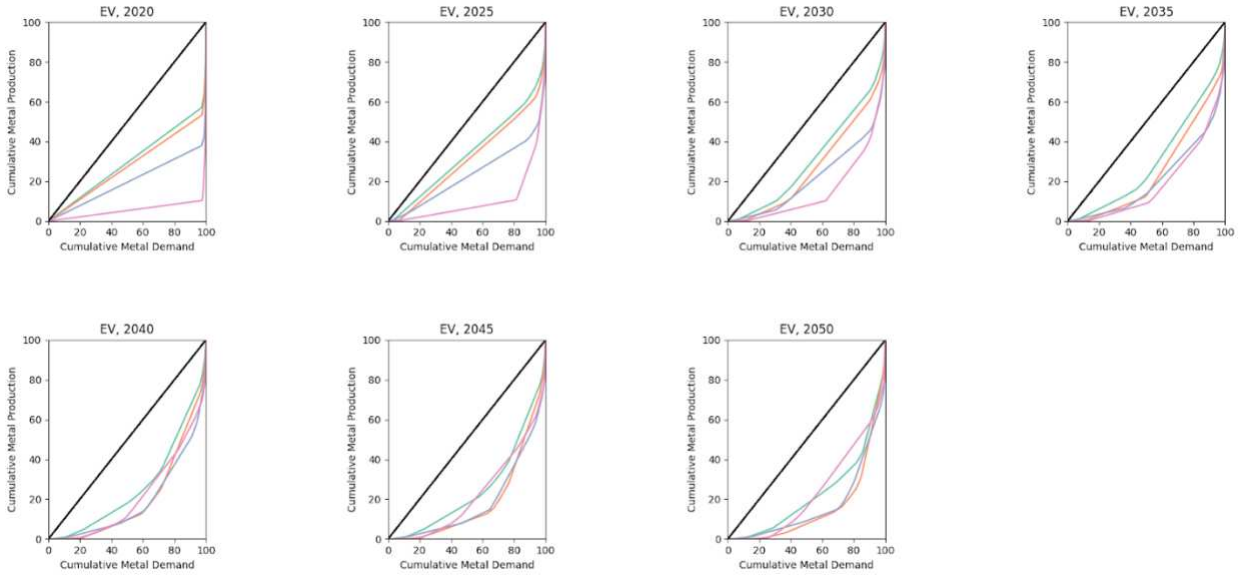

Figure C.13. Global distribution of demand and supply by metals in the Current Energy Policies for the years 2020-2050 for the Electric vehicles. Colors same as C.11

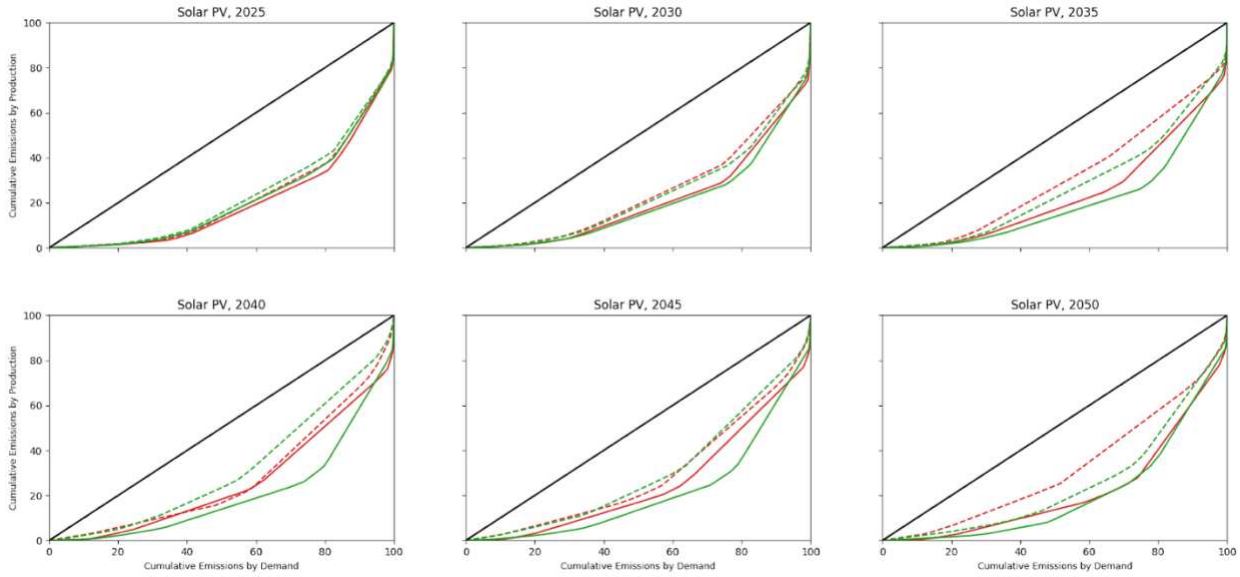

Figure C.14. Inequality in emissions by metal demand and production in Current Energy Policies (red) and Rapid Decarbonization (green) pathways with Current Abatement Legislation (solid) and Strictest Abatement (dashed) abatement scenarios for Solar PV.

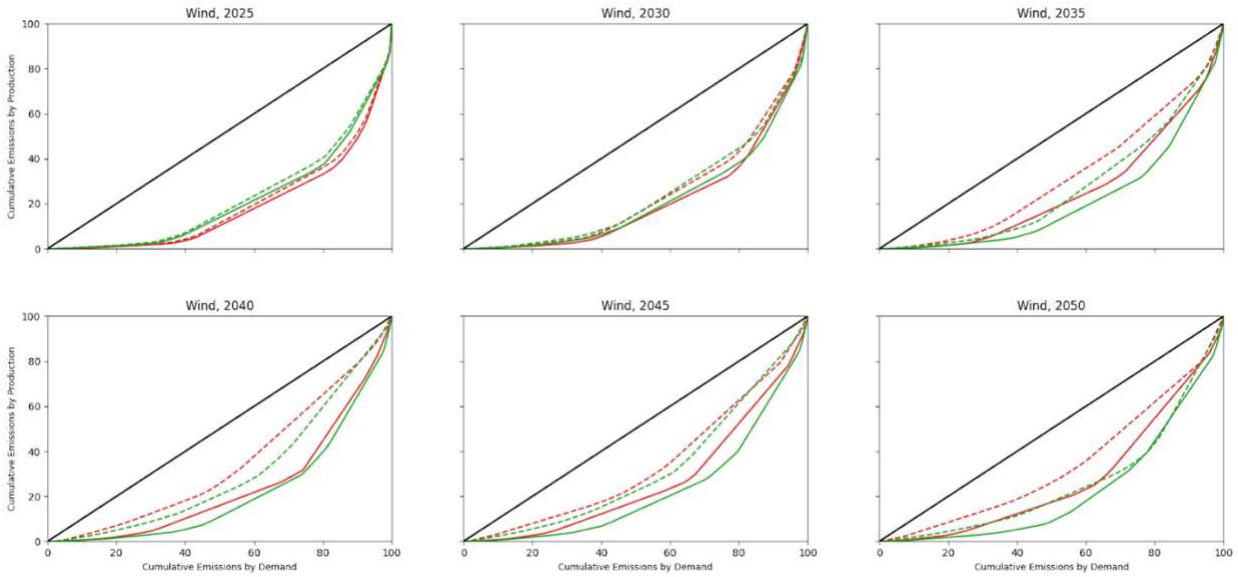

Figure C.15. Inequality in emissions by metal demand and production in Current Energy Policies (red) and Rapid Decarbonization (green) pathways with Current Abatement Legislation (solid) and Strictest Abatement (dashed) abatement scenarios for Wind turbines.

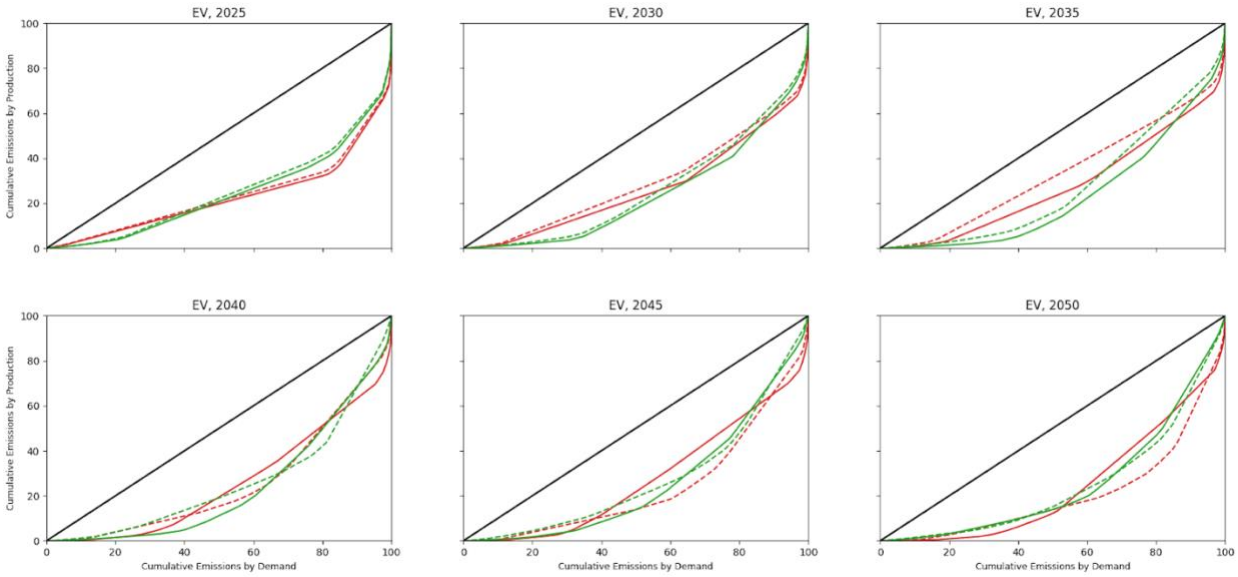

Figure C.16. Inequality in emissions by metal demand and production in Current Energy Policies (red) and Rapid Decarbonization (green) pathways with Current Abatement Legislation (solid) and Strictest Abatement (dashed) abatement scenarios for Electric vehicles.